

REU 2016



Research Experience for Undergraduates

Section 1

Support for the REU program is provided by the NSF MRSEC program (DMR-1120296) and the REU Site program (DMR-1460428).

TABLE OF CONTENTS

REU	Faculty Advisor	Page
Bishop-Van Horn, Logan	Prof. Dan Ralph	03
Britt, Carson	Prof. Christopher Ober	15
Ceron, Steven	Prof. Itai Cohen	21
Cripps, Kyle	Prof. Christopher Hernandez	24
Davis, Hazel	Prof. Brett Fors	34
DeJulius, Carlisle	Prof. Cynthia Reinhart-King	44
Diaz, Ricem	Prof. Brian Kirby	50
Frey, Peter	Prof. Kyle Shen	59
Hardy, Ashley	Prof. Katja Nowack	67
Harper, Angela	Prof. Paulette Clancy	74

Exploring Low-Frequency ST-FMR: Simulation and Experiment

LOGAN BISHOP-VAN HORN*, NEAL REYNOLDS, SAMUEL BRANTLEY, DANIEL C. RALPH†

Cornell Center for Materials Research REU

Summer 2016

Abstract

The field of spintronics, in which electrons are manipulated by way of their spin degree of freedom, shows great potential to form the basis for next generation data storage and computation technologies. Spin transfer torque-driven ferromagnetic resonance (ST-FMR) is a widely-used method for measuring current-generated spin transfer torques by exciting resonance precession in a thin magnetic film using microwave currents. In particular, ST-FMR is often used to determine the spin Hall angle, Θ_{SH} , the figure of merit for the spin Hall effect, a conversion of longitudinal charge current into transverse spin current via spin-orbit coupling. In this work we examine the accuracy of ST-FMR at low frequency as a function of sample dimensions, using both simulation and experiment.

I. INTRODUCTION

Spin transfer torques, in which a torque is applied to a nanoscale magnet by injection of a spin-polarized current, have been widely studied as alternatives to charge-based magnetic manipulation for data storage and computation applications [1,2]. The spin Hall effect, a conversion of charge current into transverse spin current via spin-orbit coupling, is one mechanism by which to generate spin currents to apply spin transfer torques [3,4]. The spin Hall angle, a figure of merit for the spin Hall effect, is defined as $\Theta_{SH} \equiv J_s / J_c$, where J_s is the spin current density and J_c is the charge current density. In a normal metal/magnetic film multilayer, charge current flowing through a metallic layer with a large spin Hall angle will inject a spin current into the magnetic layer, applying a torque to the magnetization. Accurate measurement of the spin Hall angle is critical for the development of spin orbit torque-based technologies.

A common method for measuring the spin

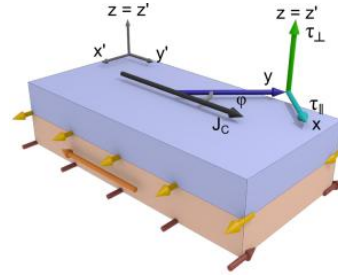


Figure 1: Coordinate system used for micromagnetic model and ST-FMR analysis [5].

Hall angle in magnetic multilayers is spin transfer torque-driven ferromagnetic resonance (ST-FMR). In ST-FMR, resonant precession of the magnetic layer is excited by applying a microwave charge current. The magnetization experiences a torque due to the Oersted field from the radio frequency (rf) charge current and a spin transfer torque due to the injection of spin current from the metallic layer via the spin Hall effect. The theory behind ST-FMR relies upon the *macrospin approximation*, which assumes the magnetic layer acts as a single spin. The magnetization is modeled as a unit

*logan.bvh@gmail.com

†dcr14@cornell.edu

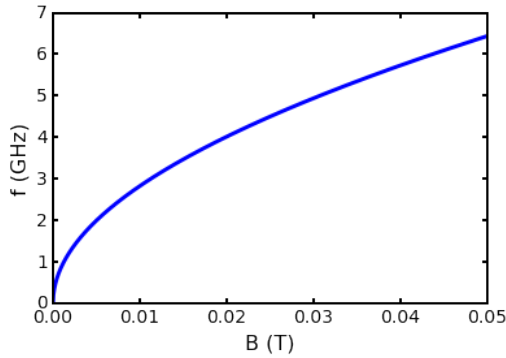


Figure 2: Resonant frequency as a function of in-plane magnetic field for a film with $M = 8 \times 10^5$ A/m, from the Kittel formula.

vector $\hat{m}(t) = m_x(t)\hat{x} + \hat{y} + m_z(t)\hat{z}$, which lies almost entirely in the y direction, with small arbitrary x and z components (see Figure 1).

The time evolution of the magnetization is described by the Landau-Lifshitz-Gilbert-Slonczewski (LLGS) equation [1]:

$$\begin{aligned} \dot{\hat{m}} = & \underbrace{-\gamma \hat{m} \times \vec{H}_{\text{eff}}}_{\text{(demagnetization)}} + \underbrace{\alpha \hat{m} \times \dot{\hat{m}}}_{\text{(Gilbert damping)}} \\ & + \underbrace{\frac{\gamma \hbar \cos \varphi}{2e\mu_0 M_s} J_s \hat{m} \times (\hat{\sigma} \times \hat{m})}_{\text{(spin transfer torque)}} \\ & - \underbrace{\gamma \cos \varphi \hat{m} \times \vec{H}_{\text{Oe}}}_{\text{(Oersted torque)}} \end{aligned}$$

Here, $\dot{\hat{m}}$ denotes the time derivative of the magnetization unit vector, γ is the gyromagnetic ratio, \vec{H}_{eff} is the effective external field, α is the Gilbert damping coefficient, μ_0 is the permeability of free space, \hbar is the reduced Planck constant, φ is the angle between the charge current and the external magnetic field, M_s is the saturation magnetization of the magnetic layer, J_s is the spin current density, $\hat{\sigma}$ is the direction of spin polarization, and \vec{H}_{Oe} is the Oersted field. The resonance condition for a thin film with with in-plane external field is given by the Kittel formula: $f = \frac{\gamma}{2\pi} \sqrt{B(B + \mu_0 M)}$ [6]. Here, f is the resonant frequency, B is the external field strength, and M is the film's magnetization. The resonant precession of the magneti-

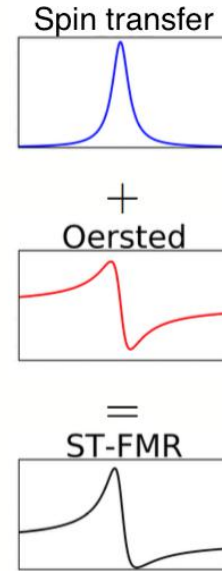


Figure 3: Components of the ST-FMR curve.

zation leads to rf oscillations in the magnetic layer resistivity due to anisotropic magnetoresistance (AMR, the dependence of resistance on the angle between the magnetization and the current). These rf oscillations in resistance mix with the rf charge current to produce a dc resonance curve. Analytical solutions to the LLGS equation predict a resonance curve that is the sum of a symmetric Lorentzian and an anti-symmetric Lorentzian, due to the spin transfer and Oersted torques, respectively (see Figure 3). The spin Hall angle can be extracted from fits to the ST-FMR resonance curves [3].

Low-frequency (i.e. < 5 GHz) ST-FMR has not been thoroughly studied. It is not known to what extent the macrospin approximation holds in this frequency regime, where the resonant field may not be strong enough to fully saturate the magnetic layer (see Figure 2). It is also not known what role spatial variations in the magnetization dynamics play in the final determination of Θ_{SH} . To begin to answer these questions, we examine low-frequency ST-FMR in magnetic bilayers as a function of sample dimensions using a combination of experiment and simulation.

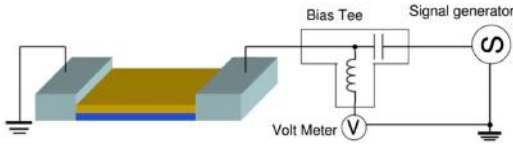


Figure 4: Schematic of ST-FMR measurement set-up [3].

II. METHODS

i. Experiment

i.1 Experimental Setup

We performed ST-FMR measurements on thin film bilayers of the form [sapphire substrate/normal metal layer (thickness in nm)/magnetic layer (thickness in nm)/thin capping layer to protect device]. Data presented below are from Pt (6)/Py (5.4) and Pt (6)/Py (10.8) (Py=Permalloy \equiv Ni₈₁Fe₁₉) samples with an Hf capping layer to prevent oxidation, and Pt (6)/CoFeB (6)/Al capping layer samples. The films were grown using dc magnetron sputter deposition in CCMR, and fabricated at CNF into devices with dimensions from 2 to 100 microns with varying aspect ratio. Ground-signal-ground waveguides were added to each device to create rf contact.

The ST-FMR measurement is performed as follows:

- Measure AMR of device using rotating projected-field magnet
- Measure the rf transmission and reflection characteristics of the device and auxiliary cabling
- Field sweep:
 - Apply charge current at fixed frequency and power
 - Set $\varphi = 45$ degrees between the external field and charge current
 - Sweep external field
 - Measure dc mixing voltage
 - Step frequency, and repeat

The rf charge current is supplied by a signal generator through a bias tee (see Figure 4). The Oersted field and spin Hall effect-generated transverse spin current apply torques to the

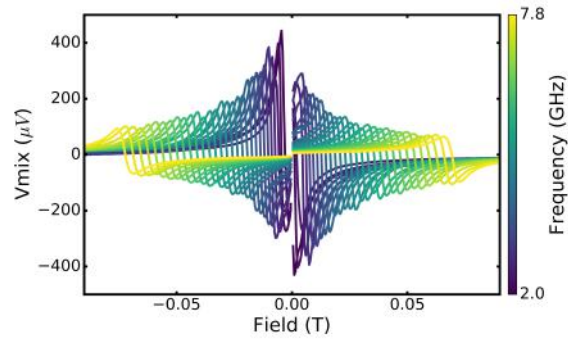


Figure 5: Experimental ST-FMR data for a $20\mu m \times 4\mu m$ Pt (6)/Py (10.8) device.

magnetization, resulting in small-angle precession. This causes oscillations in the resistance of the device due to AMR. These rf resistance oscillations mix with the rf charge current, resulting in a dc signal that is measured at the dc port of the bias tee. In order to maximize signal-to-noise, we perform amplitude modulation of the supplied current at ~ 1 kHz and use a lock-in amplifier locked in to this low-frequency signal to measure the dc mixing voltage.

i.2 Analysis

Figure 5 shows a typical sequence of ST-FMR curves at frequencies from 2-7.8GHz. In order to extract Θ_{SH} from this data, the following analysis must be performed:

- Calculate how much current is flowing through the device using the measured rf characteristics of the experimental setup
- Calculate how much current is flowing through the normal metal layer of the device using the resistivity of the normal metal material and the total device resistance (parallel resistor model)
- Fit the data to a sum of symmetric and anti-symmetric Lorentzians to extract the following fit parameters:
 - C_x : Symmetric component amplitude
 - C_z : Anti-symmetric component amplitude
 - α : Gilbert damping coefficient
 - M_{eff} : effective magnetization

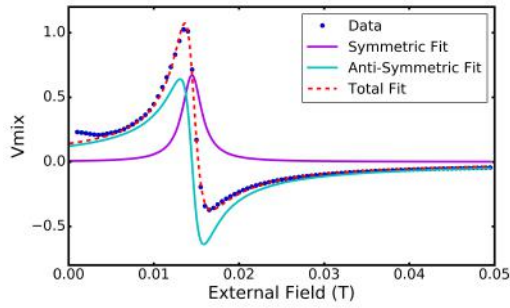


Figure 6: Typical positive field ST-FMR curve and fit.

- Multiply the ratio C_x/C_z by M_{eff} and set of constants based on the sample dimensions and experimental parameters to obtain Θ_{SH} , the "S over A" spin Hall angle

Using this fitting routine, we can examine the determined value of the spin Hall angle, effective magnetization, and Gilbert damping as a function of sample dimensions and frequency. Figure 6 shows a typical ST-FMR curve with symmetric and anti-symmetric fits.

ii. Micromagnetic Simulation

Computer simulations allow us to explore the magnetization dynamics of thin films on sub-micron length scales, allowing us to investigate the validity of the macrospin approximation in ST-FMR for various sample dimensions, materials, and frequencies. In contrast with macrospin analysis, in which it is assumed that the magnetization of the entire layer can be described by a single vector, micromagnetic analysis breaks up a sample into many cells or *microspins* and calculates their interaction amongst themselves and with the external excitations (e.g. field and spin current). We use MuMax3 GPU-accelerated micromagnetic software in the cloud utilizing AWS Elastic Cloud Compute [7,8]. Using MuMax3 we can calculate the instantaneous spatial distribution of the magnetization for visualization or animation. We can also output the vector components of the unit magnetization as a function of time, averaged over all or part of the magnetic layer.

The micromagnetic model for ST-FMR has

the following components (see Figure 1 for coordinate system):

- In-plane magnetized (y direction) magnetic layer with set dimensions and material parameters:
 - Saturation magnetization
 - Gilbert damping
 - Exchange strength
- rf charge current in y' direction and resulting Oersted field
- In-plane external field at an angle φ relative to the rf charge current
- Spin current in $z = z'$ direction, with polarization in x' direction and spin current density J_s determined by fixed spin Hall angle $\Theta_{SH} \equiv J_s/J_c$

ii.1 Simulated ST-FMR

In order to evaluate the extent to which micromagnetic simulations can simulate ST-FMR, we turn first to the task of simulating the dc mixing voltage which comprises our experimental data. Since experimental ST-FMR results arise from the AMR of the entire sample, we need to examine the x' component of the magnetization averaged over the whole film. In MuMax3 we perform field sweeps at a sequence of frequencies, just as in ST-FMR experiments. The output from these simulations is a single text file containing the vector components of the spatially-averaged magnetization as a function of time for all field sweeps performed (see Figure 7). MuMax3 uses an adaptive time step ODE solver, resulting in arbitrary time spacing. The first step in data processing is to perform a cubic spline to obtain data that is evenly spaced in time. To obtain ST-FMR data from these simulations the following steps are performed:

- For each frequency:
 - For each field:
 - * Identify the time period corresponding to this field
 - * Disregard the first half of this time period (transient)
 - * Multiply the $m_{x'}$ signal from the second half of this time period

by $\sin(2\pi \cdot f \cdot t)$, where f is the frequency of the rf current and t is time

- * Integrate the multiplied signal over $n \in \mathbb{N}$ periods and divide by $T = n/f$ to simulate the mixing of the rf resistance and rf current

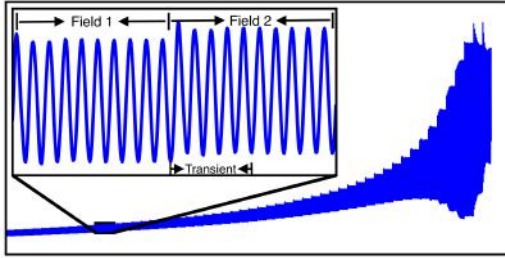


Figure 7: x' component of the magnetization for a single MuMax3 field sweep. The timescale of the inset (showing two field steps) is 10ns. Resonance is visible to the right of the inset. The first half of each field step is ignored to allow any transient to subside.

This computation preserves both the amplitude and phase of the magnetization dynamics, resulting in ST-FMR curves as shown in Figure 8. Once the ST-FMR curves are obtained, we can fit them to the Lorentzian model predicted by the LLGS equation (see Figure 6) to extract the parameters C_x (the symmetric Lorentzian amplitude), C_z (the anti-symmetric Lorentzian amplitude), M_{eff} (the effective magnetization in tesla), and α (the Gilbert damping coefficient). The "S over A" spin Hall angle is then given by

$$\Theta_{\text{SH}} = -\frac{C_x}{C_z} \frac{e}{\hbar} M_{\text{eff}} t^2$$

Here, e is the elementary charge and t is the thickness of the magnetic layer in meters.

III. RESULTS

i. Experimental Results

Most of the experimental data obtained was from the Pt (6)/CoFeB (6) devices. Due to time

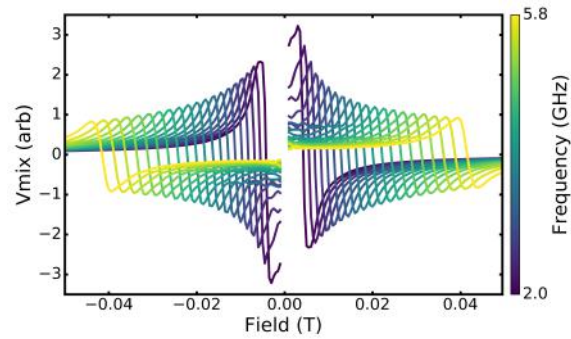


Figure 8: Simulated ST-FMR data for a $20\mu\text{m} \times 4\mu\text{m} \times 10\text{nm}$ Py film with spin current corresponding to Θ_{SH} of Pt.

constraints, a very limited amount of Pt/Py data was taken.

i.1 CoFeB ST-FMR

Below is data demonstrating the low-frequency trends in Θ_{SH} as a function of sample dimensions. Except for extreme cases (i.e. frequencies below $\sim 4\text{GHz}$, very high or very low aspect ratios), Θ_{SH} showed very good agreement with the expected value: ≈ 0.07 for Pt [9]. As can be seen in Figure 9, the determined value for Θ_{SH} begins to diverge with decreasing frequency below about 4GHz, at a rate that depends upon the sample length. A similar effect can be seen as a function of sample width where, all else equal, Θ_{SH} for narrower samples diverges faster than Θ_{SH} for wider samples. While the devices presented in the lower graph of Figure 9 are not all the same length, they are all long enough to be in a regime where relatively small differences in length do not cause significant changes in the trend in Θ_{SH} .

The dependence on sample dimensions is much greater at low frequencies than at higher frequencies. Figure 10 shows Θ_{SH} as a function of sample length and frequency for samples of two different widths. Particularly interesting is the $2\mu\text{m}$ wide sample, which shows a maximum in Θ_{SH} as a function of length that develops with decreasing frequency. Such a feature is not seen in wider samples. Graphs such as Figure 10 could serve as a useful roadmap for

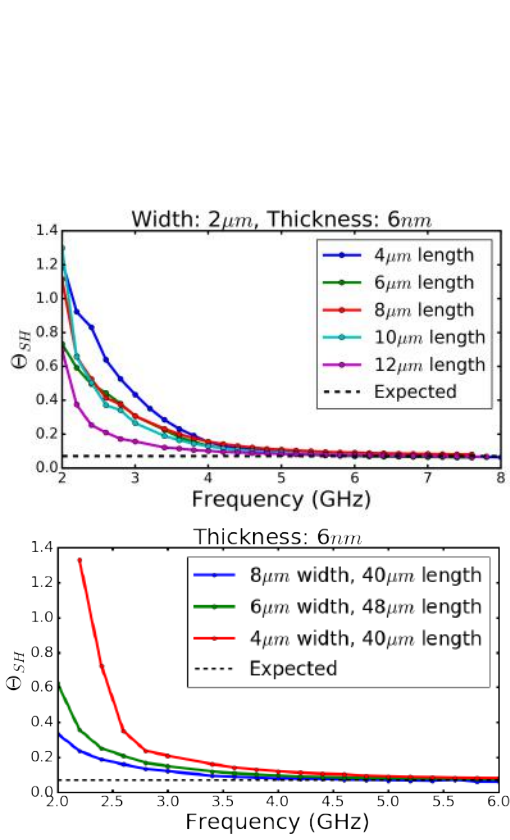


Figure 9: Θ_{SH} for Pt (6)/CoFeB (6) samples with $2\mu m$ width and varying length (top) and varying width (bottom). The devices in the bottom graph are long enough that the small difference in length between them does not affect Θ_{SH} . The determined value for the spin Hall angle diverges at low frequencies, at a rate that depends on sample dimensions.

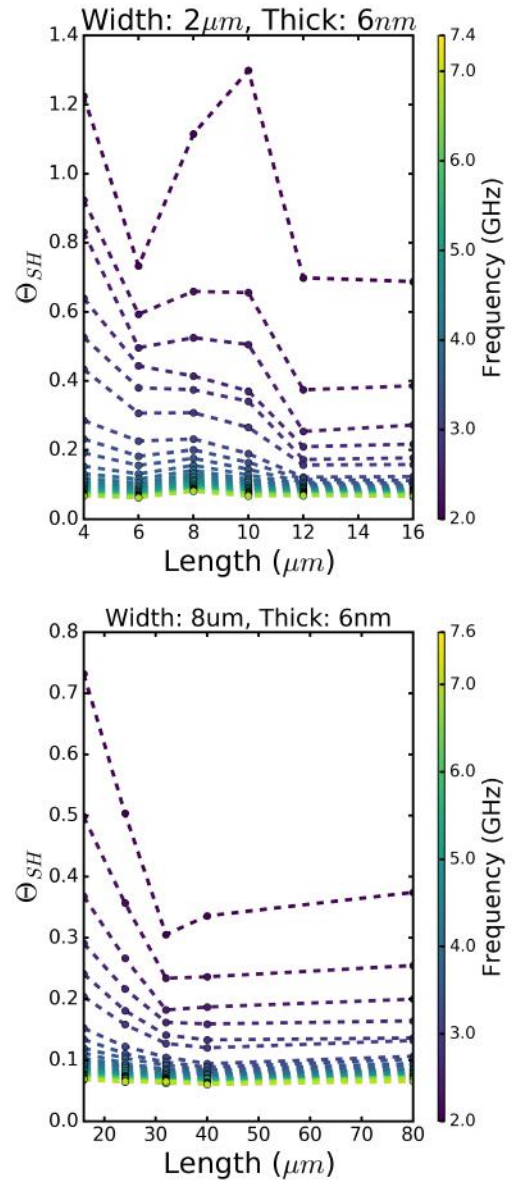


Figure 10: Θ_{SH} as a function of sample length and frequency for two Pt (6)/CoFeB (6) samples of different widths.

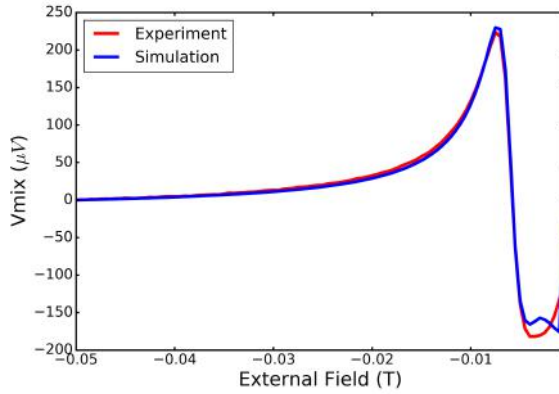


Figure 11: Experimental and simulated ST-FMR curves for a $24\mu\text{m} \times 4\mu\text{m} \times 5.4\text{nm}$ Py layer at 2GHz. Simulation data has been scaled vertically by a constant factor.

determining over which regions of parameter space ST-FMR results are valid.

ii. Simulation Results

To evaluate the validity of the micromagnetic model, the effective magnetization M_{eff} and Gilbert damping coefficient α were extracted from fits to the Lorentzian model for experimental ST-FMR data from a $24\mu\text{m} \times 4\mu\text{m}$ Pt (6)/Py (5.4) device. These parameters were then used to model a device with the same dimensions. Figure 11 shows both experimental and simulated ST-FMR curves for a field sweep at 2GHz. The simulated data (whose amplitude is arbitrary) has been scaled vertically by a constant factor. Clearly there is very good agreement between simulation and experiment, even in a frequency regime where the macrospin approximation may not hold.

One difficulty with this type of analysis is that M_{eff} and α are not well constrained under the current fitting method, so their values tend to drift as a function of frequency (see Figure 17). The micromagnetic model uses a single value for these parameters for all frequencies. The result is that the experimental and simulated ST-FMR curves do not agree to the same extent across a whole frequency sweep.

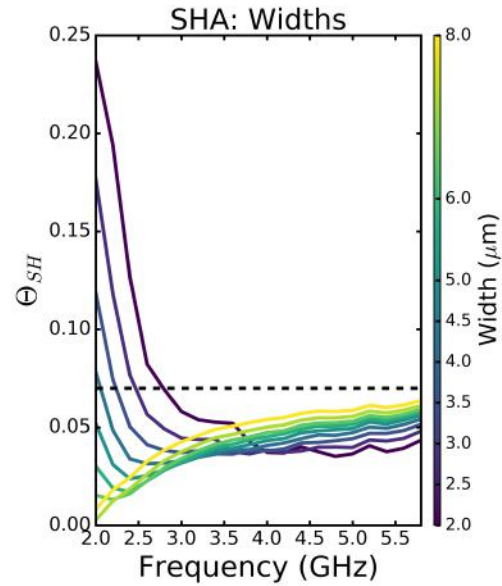


Figure 12: Simulated Θ_{SH} for $20\mu\text{m}$ long, 6nm thick Py samples as a function of frequency and sample width. The dotted black line shows the actual spin Hall angle

ii.1 Θ_{SH} Measurements

We examined Θ_{SH} extracted from micromagnetic simulation data using the "S over A" method described above. All of the simulations were of Permalloy samples, which makes it difficult to make quantitative comparisons to the CoFeB experimental results. Qualitatively, however, the simulations reproduce the trends in Θ_{SH} at low frequency. Figure 12 shows the simulated ST-FMR-determined spin Hall angle $20\mu\text{m}$ long, 6nm thick Py samples as a function of frequency and sample width. The divergence in Θ_{SH} with decreasing frequency for narrower samples is consistent with the results from CoFeB measurements. For wider samples, however, the simulated spin Hall angle decreases with decreasing frequency, which we do not see experimentally. Figure 13 shows that for thicker samples, the ST-FMR-determined value for Θ_{SH} in thicker magnetic films is suppressed for "intermediate" frequencies ($\sim 3\text{GHz} - \sim 6\text{GHz}$). We do not have experimental data, either CoFeB or Permalloy, to which to compare this result.

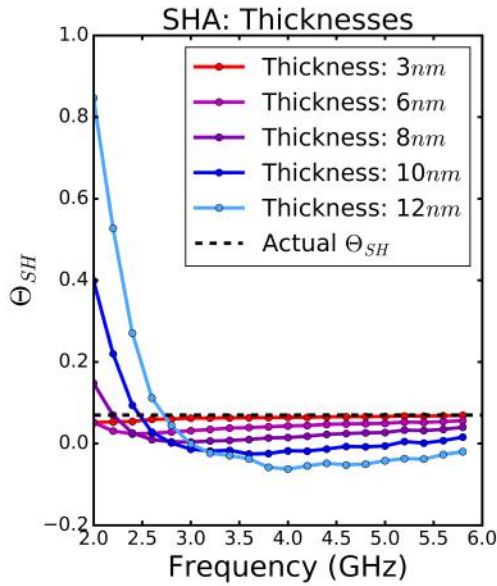


Figure 13: Simulated ST-FMR-determined Θ_{SH} as a function of frequency and magnetic layer thickness for a $20\mu\text{m} \times 4\mu\text{m}$ Py samples. The dotted black line shows the actual spin Hall angle.

ii.2 Spatial Analysis

Given the form of the Kittel resonance condition (Figure 2), it is possible that at lower frequencies the resonant field is not strong enough to satisfy the macrospin approximation. It is therefore desirable to examine the spatial variation in magnetization dynamics, which ST-FMR is not sensitive to. MuMax3 has the option to output spatial magnetization data either in the form of .jpg images (Figure 14) or .ovf files, which can be converted into images using other software.

As images like those in Figure 14 show, there are significant variations in the magnetization dynamics across the sample. In order to better understand these spatial variations, we examined the relative phase and amplitude of the magnetization precession in various regions of the sample.

Figure 15 shows that in a thin sample (6nm), the oscillations at the edge of the sample almost always lag the oscillations at the center. This is not surprising, as the material at the edge of

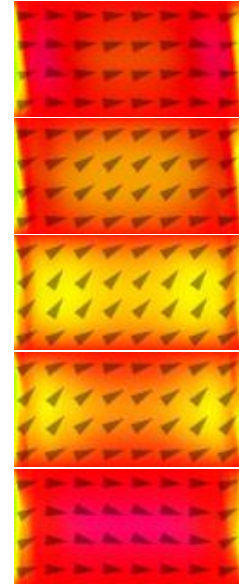


Figure 14: Visualization of the magnetization of a $10\mu\text{m} \times 1\mu\text{m} \times 6\text{nm}$ Py film, driven at 2.4GHz, over roughly one period near resonance. The triangles and color represent the direction of the magnetization in different regions

the sample is more strongly influenced by the demagnetization field. The phase shift between the edge and center at resonance grows with decreasing frequency, which is not surprising as the resonant field is lower at lower frequencies.

In the thicker sample (12nm), the phase shift at resonance is larger for all frequencies, the region of large phase shift around resonance is wider, and the frequency of maximum phase shift is higher than in the 6nm sample. At higher frequencies, in addition to the minimum at resonance, we see maxima and minima in the phase difference as a function of field below the resonant field. This is a very interesting result, and certainly warrants further investigation, both in experiment and in simulation.

We can also examine the amplitude of the magnetization precession in different regions of the sample. Figure 16 shows the precession amplitude in the edge and center regions of a $20\mu\text{m} \times 4\mu\text{m} \times 12\text{nm}$ Py film, as defined in the top image of Figure 15. The bottom

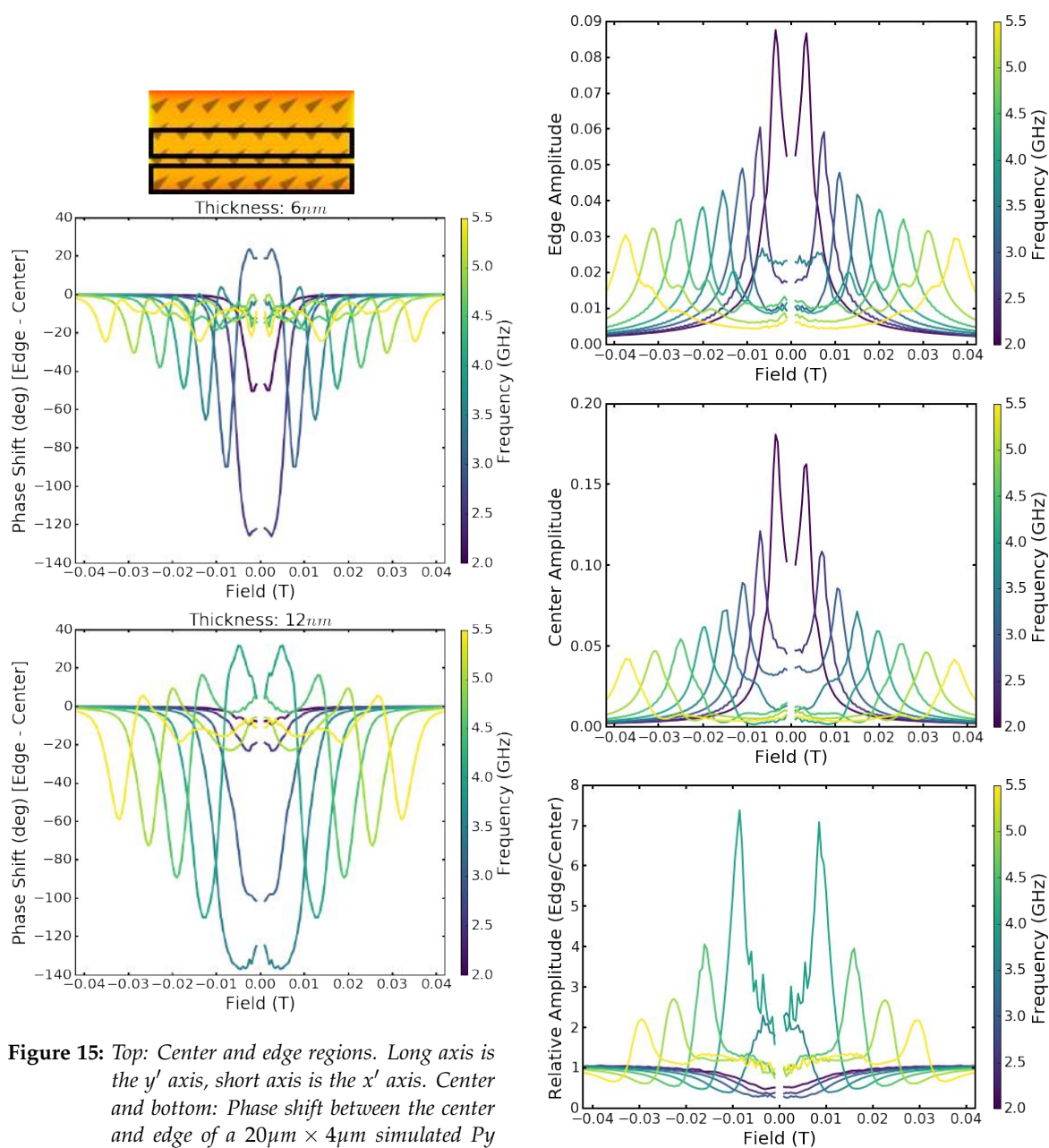


Figure 15: Top: Center and edge regions. Long axis is the y' axis, short axis is the x' axis. Center and bottom: Phase shift between the center and edge of a $20\mu\text{m} \times 4\mu\text{m}$ simulated Py sample as a function of field for 6nm (center) and 12nm (bottom) films. Negative phase shift means the center "leads" the edge.

Figure 16: Top and center: Precession amplitude at the edge and center of a $20\mu\text{m} \times 4\mu\text{m} \times 12\text{nm}$ Py film as a function of field. Bottom: relative precession amplitude (edge/center) between the two regions.

panel shows the relative amplitude (edge amplitude/center amplitude) between the two regions. As expected, there is a maximum in both edge and center amplitudes at resonance. There is also a minimum in relative amplitude at resonance (meaning that the amount by which the center amplitude is larger is at a maximum). This is also to be expected. What is somewhat surprising is the maximum in relative amplitude after resonance (as the magnitude of the field decreases), for instance at about $\pm 0.015T$ in the 4.5GHz curve. It appears this is due to additional local maxima that develop in the edge amplitude (top graph) below the resonant field.

IV. DISCUSSION

i. Lorentzian Model

As can be seen in Figure 11, given the right material parameters (saturation magnetization, Gilbert damping, and exchange strength), the micromagnetic model can very accurately recreate experimental ST-FMR curves. The effective magnetization, M_{eff} , and Gilbert damping coefficient, α , can be extracted from fits to experimental data. However, since these two parameters are strongly coupled and not well constrained, their values as determined by fitting to the Lorentzian model are not constant as a function of frequency (see Figure 17). In the future, even at high frequencies, it would likely be wise to fit both the experimental and simulated ST-FMR data to the more general Lorentzian form as described in Ref. [3].

It appears the ST-FMR curves are not a simple sum of Lorentzians at very low frequencies due to breakdown of the macrospin approximation, and therefore the extracted values for M_{eff} and α are not reliable in this regime. **It seems likely that the low frequency divergence in the determined value of the effective magnetization is main cause of the low frequency divergence in Θ_{SH} .** In both simulation and experiment, the nature of the divergence in M_{eff} seems to depend upon sample dimensions. This suggests the dimensions of the

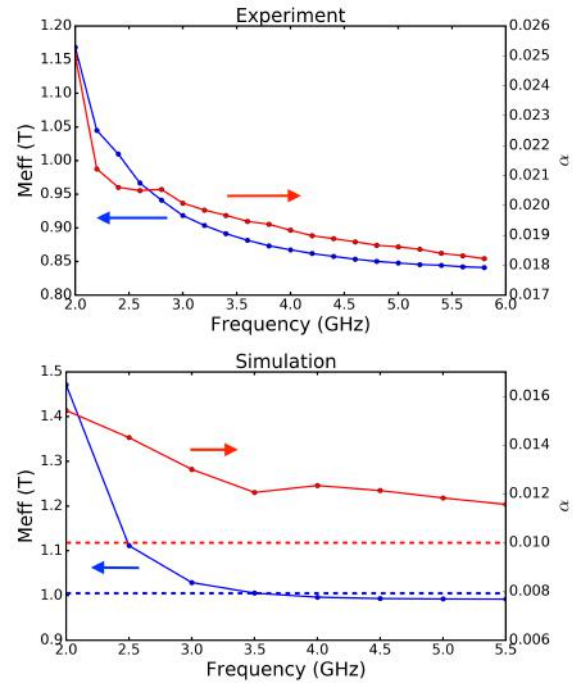


Figure 17: Values for M_{eff} (blue) and Gilbert damping coefficient, α , (red) extracted from fits to experimental (top) and simulated (bottom) ST-FMR data. Experimental data is from a $24\mu\text{m} \times 4\mu\text{m}$ Pt (6)/Py(5.8) device. Dotted lines in simulated data show actual values for M_{eff} and α .

sample affect the way in which the magnetization dynamics differ from the macrospin model.

ii. Sample Dimensions

It is clear from both the experimental CoFeB data and the simulated Py data that all three sample dimensions, length, width, and thickness, play an important role in the magnetization dynamics and ST-FMR measurements of thin films at low frequency. The experimental CoFeB data (Figures 9 & 10) shows dependence of the ST-FMR-determined spin Hall angle on sample length and width, and the simulated Py data (Figure 12) shows a similar dependence on sample width. Unfortunately we do not at this time have simulated CoFeB data to compare to experiment, nor do

we have enough experimental Py data to make detailed comparisons to simulation.

Figure 13 shows that the ST-FMR-determined value for Θ_{SH} in thick samples is suppressed at intermediate frequencies (roughly 3GHz–6GHz) and diverges at lower frequencies. **The suppression of Θ_{SH} in thick samples appears to be a result of destructive interference between different regions of the sample (see Figure 15).** However, this does not explain why the determined value of Θ_{SH} rises *above* the actual value at the lowest frequencies. **The most likely explanation for this is the divergence in the fit-determined value of M_{eff} , because in the ST-FMR analysis $\Theta_{\text{SH}} \propto M_{\text{eff}}$.** This is supported by the data in Figure 12, which appears to show two competing terms affecting Θ_{SH} : one term (the destructive interference between different regions) that tends to decrease Θ_{SH} with decreasing frequency, and another term (the divergence in M_{eff}) that tends to increase Θ_{SH} with decreasing frequency.

iii. Simulation Tools

We have developed a large set of tools for performing micromagnetic simulations of ST-FMR and analyzing and visualizing the results. These tools, written in Python, include:

- Standard ST-FMR analysis, including the calculation of Θ_{SH}
- Analysis and comparison of the phase and amplitude of 2-5 regions in a single sample
- Analysis and comparison of the phase and amplitude of up to 5 regions in two different samples (if, for example, one wants to change a material parameter and examine the effect that has on the spatial variation)
- Analysis of phase relative to driving current in two regions of a sample
- Tools for creating clear visualizations of the results of the above analyses

Micromagnetic ST-FMR simulations can serve as a very valuable probe into the microscopic phenomena that lead to the macroscopic data (i.e., the dc mixing signal). These simulations

may also serve as a useful bridge to connect ST-FMR, which is not sensitive to spatial information about the magnetization dynamics, to other spatially-resolved measurements such as time-resolved anomalous Nernst effect (TRANE) microscopy [10] and Brillouin light scattering (BLS) spectroscopy [11], allowing clearer interpretation of results across measurement methods.

Acknowledgements: I would like to thank Neal Reynolds for his guidance this summer, Samuel Brantley for performing the device fabrication at CNF, and Dr. Ralph for his guidance and support. This work was made possible by the Cornell Center for Material Research, the Cornell NanoScale Science & Technology Facility, the NSF MRSEC program (DMR-1120296) and the REU Site program (DMR-1063059).

REFERENCES

- [1] Slonczewski, Current-driven excitation of magnetic multilayers. *J. Magn. Magn. Mater.*, **159**, L1-L7 (1996).
- [2] Kiselev, *et al.*, Microwave oscillations of a nanomagnet driven by a spin-polarized current. *Nature*, **425**, (2003).
- [3] Liu, *et al.*, Spin-Torque Ferromagnetic Resonance Induced by the Spin Hall Effect. *Phys. Rev. Lett.*, **106**, 036601 (2011).
- [4] Liu, *et al.*, Spin-Torque Switching with the Giant Spin Hall Effect of Tantalum. *Science*, **336**, (2012).
- [5] Mellnik, Notes on ST-FMR, <http://alex.mellnik.net/notes-on-st-fmr/>
- [6] Kittel, Introduction to Solid State Physics 7th edn, 505 (John Wiley & Sons, New York, 1996).
- [7] Vansteenkiste, *et al.*, The design and verification of MuMax3, *AIP Advances*, **4**, 107133 (2014).

- [8] Jermain, *et al.* GPU-accelerated micromagnetic simulations using cloud computing. *J. Magn. Magn. Mater.*, **401**, 320-322 (2016).
- [9] Liu, *et al.* Review and Analysis of Measurements of the Spin Hall Effect in Platinum. arXiv:1111.3702, (2012)
- [10] Guo, *et al.* Ferromagnetic resonance phase imaging in spin Hall multilayers. *Phys. Rev. B*, **93**, 144415 (2016).
- [11] Jungfleisch, *et al.* Large Spin-Wave Bullet in a Ferrimagnetic Insulator Driven by the Spin Hall Effect. *Phys. Rev. Lett.*, **116**, 057601 (2016).

Synthesis of Block Copolymers Containing Stable Radicals

Carson Britt¹, Yiren Zhang², Christopher Ober²

¹Department of Chemistry, Case Western Reserve University, Cleveland OH

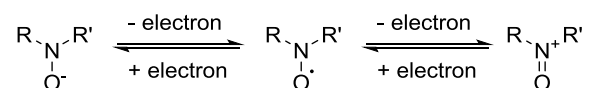
²Department of Materials Science and Engineering, Cornell University, Ithaca NY

ABSTRACT: Radical polymers are a subgroup of electronically active polymers that contain stable radical pendant groups on a polymer backbone. These stable radical pendant groups can undergo reversible redox reactions, and for this reason have been identified as a potential electrode material for batteries. Studies have shown these radical polymers can exhibit charge rates hundreds of times greater than inorganic materials used as electrodes in batteries, which could lead to drastically reduced charging times in future devices if these charge-rates are realized commercially. These radical polymers do have limitations however, such as poor charge transport properties due to the insulating nature of commonly used non-conjugated polymer backbones. In this study we created block copolymers composed of a conducting conjugated polymer, P3HT, and a radical polymer, PTMA, so that we could study the effect that a conjugated polymer block has on the charge transport properties of a radical polymer.

INTRODUCTION

Electronically active polymers, such as conjugated or radical polymers, are promising materials for use in modern electronics, as they exhibit thin film properties, they are readily made and altered using controllable synthetic techniques, and can be cost effective when produced in bulk. Radical polymers are a subgroup of electronically active polymers that are composed of two units: a polymer backbone and a stable radical pendant group. The polymer backbone is typically non-conjugated, with ethylenic, styrenic, acrylic, and methacrylic backbones being among the most common¹. The second part of the radical polymer, the stable radical pendant group, is attached to these backbone structures. The radical on this pendant group is typically stabilized by nearby bulky substituents, conjugated substituents, or both. A key property of these radical polymers is the ability of the stable radical pendant groups to undergo reversible redox reactions, as shown in Scheme 1, and it is because of this property that radical polymers hold promise as an electrode material for use in next generation batteries.

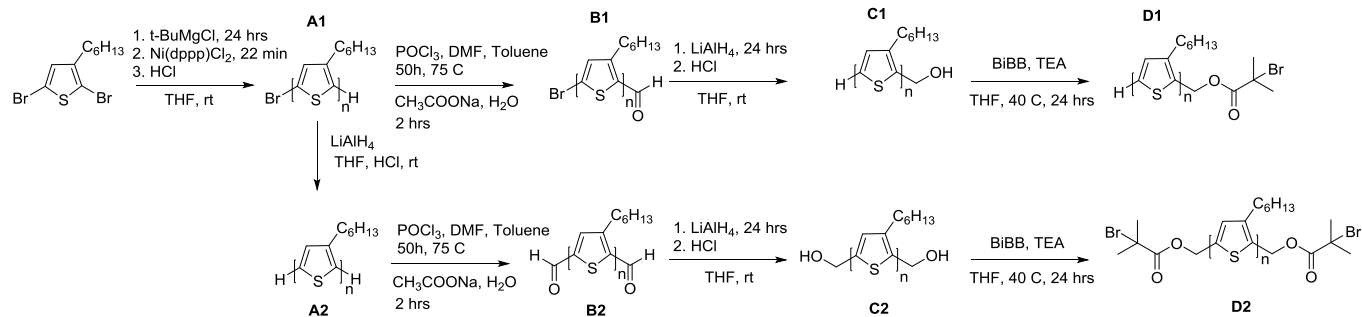
Although devices incorporating radical polymers have not yet been introduced commercially, studies indicate that these polymers exhibit charge-rates of 10-50C,



Scheme 1: Redox reaction of a nitroxide radical

hundreds of times higher than inorganic batteries, which generally have charge-rates between 0.1-0.5C¹. Despite these advantages, there are limitations that need to be overcome in order to make even higher performance radical polymers. One of these limitations that has been identified is the poor charge transport properties that radical polymers exhibit due to the insulating nature of commonly used non-conjugated backbones.

In this study, we seek to address these poor charge transport properties by combining a typical radical polymer and a typical conjugated polymer, P3HT and PTMA respectively, into a block copolymer. P3HT is a well-studied conjugated polymer that is readily synthesized with low PDI and controllable end groups. In films, P3HT forms conducting nanofibrils through pi-pi stacking. By combining P3HT with PTMA in a block copolymer, we hope to achieve a nanoscale phase separation in film where P3HT blocks facilitate charge transport between PTMA blocks that undergo reversible redox reactions. We identified two synthetic routes to make these radical block copolymers - ATRP from a P3HT macroinitiator, and “click” chemistry between azide functionalized PTMPM and alkyne functionalized P3HT homopolymers. This report details the synthetic procedure used to create these block co-polymers, and reports preliminary characterization results of the formed radical block copolymers.



Scheme 2: Synthesis of mono-functionalized macroinitiator (top) and di-functionalized macroinitiator (bottom)

EXPERIMENTAL

P3HT Macroinitiator:

α -bromo poly(3-hexylthiophene) (A1): 2,5-dibromo-3-hexylthiophene (0.464 g, 1.42 mmol) and dry THF (3.5 mL) were added to a flask with a Teflon stir bar in a nitrogen atmosphere. *t*-BuMgCl (0.85M solution in THF, 1.6 mL, 1.36 mmol) was added via syringe, and the mixture was stirred at room temperature for 24 hours. Ni(dppp)Cl₂ (0.0162g, 0.30 mmol) was added, and the mixture was stirred for 30 minutes at room temperature. Dilute HCl was added, and the reaction was then precipitated in MeOH. The product was then washed by Soxhlet extraction with MeOH and hexanes. Yield: 0.081 g.

poly(3-hexylthiophene) (A2): Compound **A1** (0.165 g, 0.033 mmol) and dry THF (26.35 mL) were added to a flask with a Teflon stir bar in a nitrogen atmosphere. LiAlH₄ (0.80M solution in THF, 0.83 mL, 0.66 mmol) was then added dropwise via syringe, and the mixture was stirred at room temperature for 24 hours. The reaction was precipitated in MeOH, then washed by Soxhlet extraction with MeOH. Yield: 0.166 g.

α -bromo, ω -formyl, poly(3-hexylthiophene) (B1): Compound **A1** (0.080 g, 0.016 mmol) and anhydrous toluene (21 mL) were added to a flask with a Teflon stir bar in a nitrogen atmosphere. DMF (0.26 mL) and POCl₃ (0.2 mL) were added via syringe, and the mixture was stirred at 75° C for 48 hours. After the reaction cooled to room temperature, a solution of saturated aqueous sodium acetate was added, and the reaction was stirred for 2 hours at room temperature. The reaction was precipitated in MeOH, then washed by Soxhlet extraction with MeOH. Yield: 0.127 g. ¹H NMR (300 MHz, CDCl₃) M_nNMR = 5k g/mol

α -formyl, ω -formyl, poly(3-hexylthiophene) (B2):

The same procedure as **B1** was used, using compound **A2**, and doubling reactants. ¹H NMR (400 MHz, CDCl₃) M_nNMR = 7.2k g/mol

ω -hydroxyl, poly(3-hexylthiophene) (C1):

Compound **B1** (0.127 g, 0.025 mmol) and dry THF (42 mL) were added to a flask with a Teflon stir bar in a nitrogen atmosphere. LiAlH₄ (0.8M solution in THF, 0.33 mL, 0.26 mmol) was then added dropwise via syringe, and the mixture was stirred at room temperature for 24 hours. The reaction was precipitated in MeOH, then washed by Soxhlet extraction with MeOH. Yield: 0.0965 g.

α -hydroxyl, ω -hydroxyl, poly(3-hexylthiophene) (C2):

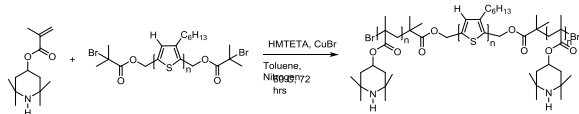
The same procedure as **C1** was used, using compound **B2**, and doubling reactants.

ω -bromoisobutyryl poly(3-hexylthiophene) (D1):

Compound **C1** (0.097 g, 0.019 mmol) and dry THF (8 mL) were added to a flask with a Teflon stir bar in a nitrogen atmosphere. TEA (1.8 mL, 13.2 mmol) was added via syringe. α -Bromoisobutyryl bromide (0.35 mL, xx mmol) was added dropwise via syringe, and the reaction mixture was stirred at 40° C for 24 hours. The reaction was precipitate in MeOH, then washed by Soxhlet extraction with MeOH. Yield: 0.070 g.

α -bromoisobutyryl, ω -bromoisobutyryl, poly(3-hexylthiophene) (D2): The same procedure as **D1** was used, using compound **C2**, and doubling reactants.

PTMPM-*b*-P3HT-*b*-PTMPM (E2): Compound **D2** (0.076 g, 0.011 mmol), TMPM (4.76 g, 21.2 mmol), HMTETA (0.054 g, 0.23 mmol), and anhydrous toluene (5.5 mL) were added to a flask with a Teflon stir bar in a nitrogen atmosphere. The mixture was degassed five times by freeze-pump-thaw cycling. The degassed solution was then transferred via cannula to



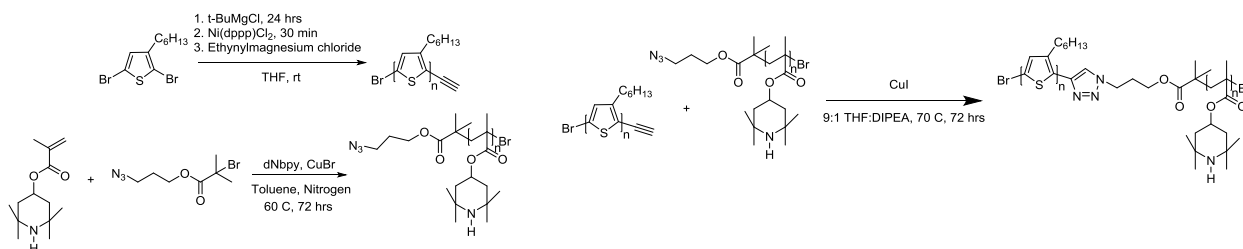
Scheme 3: Synthesis of PTMPM-b-P3HT-b-PTMPM

a flask containing CuBr (0.014 g, 0.098 mmol) and a Teflon stir bar in a nitrogen atmosphere. The reaction mixture was stirred at 60° C for 18 hours. The reaction was exposed to air, and then precipitated in hexanes. The precipitate was then dissolved in a small amount of THF, and precipitated again in hexanes. Yield: 0.64 g.

PTMA-b-P3HT-b-PTMA: Compound **E2** (0.25 g, 0.0016 mmol) and DCM (10 mL) were added to a flask with a Teflon stir bar in a nitrogen atmosphere. A solution of mCPBA (0.7235 g, 4.19 mmol) and DCM (50 mL) was added dropwise to the flask over the course of 2 hours at 0° C. After the addition was complete, the reaction was allowed to stir for 1 hour at 0° C. The reaction was then washed twice with a solution of saturated sodium bicarbonate, twice with a solution of 0.1M HCl, and twice with water. The organic layer was then concentrated, and precipitated in hexanes. Yield: 0.39 g. ¹H NMR (400 MHz, CDCl₃) M_nNMR = 160k g/mol

Azide-Alkyne “Click” Chemistry:

Alkyne functionalized P3HT: 2,5-dibromo-3-hexythiophene (0.494 g, 1.51 mmol) and dry THF (3.75 mL) were added to a flask with a Teflon stir bar in a nitrogen atmosphere. *t*-BuMgCl (0.85M solution in THF, 1.7 mL, 1.45 mmol) was added via syringe, and the mixture was stirred at room temperature for 24 hours. Ni(dppp)Cl₂ (0.0172g, 0.032 mmol) was added, and the mixture was stirred for 30 minutes at room temperature. Ethynylmagnesium chloride (0.6M solution in THF, 0.63 mL, 0.38 mmol) was added, the



Scheme 4: Synthesis of P3HT-b-PTMPM via alkyne azide click chemistry

reaction was stirred for 3 minutes, then precipitated in MeOH. Yield: 0.136 g. ¹H NMR (400 MHz, CDCl₃) M_nNMR = 7.9k g/mol

Azide functionalized PTMPM: Azide functionalized BiBB (0.126 g, 0.50 mmol), TPM (14.27 g, 63.43 mmol), dNbpy (0.216 g, 0.53 mmol), and anhydrous toluene (16.5 mL) were added to a flask with a Teflon stir bar in a nitrogen atmosphere. The mixture was degassed five times by freeze-pump-thaw cycling. The degassed solution was then transferred via cannula to a flask containing CuBr (0.0384 g, 0.27 mmol) and a Teflon stir bar in a nitrogen atmosphere. The reaction mixture was stirred at 60° C for 18 hours. The reaction was exposed to air, and then precipitated in hexanes. The precipitate was then dissolved in a small amount of THF, and precipitated again in hexanes. Yield: 5.642 g. M_nNMR could not be determined.

PTMPM-b-P3HT: Azide functionalized PTMPM (1.87g, unknown mw), alkyne functionalized P3HT (0.102 g, 0.013 mmol), CuI (4 mg, 0.02 mmol), and a solution of THF and DIPEA in a 9:1 ratio (8 mL) were added to a reaction tube with a Teflon stir bar in a nitrogen atmosphere. The mixture was stirred at 70° C for 72 hours. The reaction was exposed to air, then precipitated in hexanes. The precipitate was then dissolved in a small amount of THF, and precipitated again in hexanes. Yield: 1.92 g.

PTMA-b-P3HT: PTMPM-b-P3HT (0.251 g, unknown mw) and DCM (10 mL) were added to a flask with a Teflon stir bar in a nitrogen atmosphere. A solution of mCPBA (0.725 g, 4.2 mmol) and DCM (40 mL) was added dropwise to the flask over the course of 1 hour at 0° C. After the addition was complete, the reaction was allowed to stir for 1 hour at 0° C. The reaction was then washed twice with a solution of saturated sodium bicarbonate, twice with a solution of 0.1M HCl, and twice with water. The organic layer was then concentrated, and precipitated in hexanes. Yield: 0.207 g.

RESULTS AND DISCUSSION

P3HT Macroinitiator

Synthesizing low PDI P3HT with 100% H/Br end groups was identified as an important aspect in the synthesis of the P3HT macroinitiator. The H end group is the anchor from which we would perform our end group modifications. If we could not ensure that we had 100% H/Br end groups, and we instead had a mixture of H/Br and H/H end groups, we could inadvertently modify both end groups of the polymer during end group transformation, leading to a di-functionalized macroinitiator instead of the desired mono-functionalized. After searching the literature, it was found that complete consumption of *t*-BuMgCl was the key factor in obtaining 100% H/Br end groups². For this reason, it was important to titrate the *t*-BuMgCl before use in reactions so that the molar ratio of *t*-BuMgCl to 2,5-dibromo-3hexylthiophene could be carefully controlled. Additionally, to avoid disproportionation and to achieve low PDI, it is

important to quench the P3HT polymerization with HCl before precipitating in MeOH^{1,2}.

After P3HT with H/Br end groups had been synthesized, we proceeded with end group modification. As can be seen in scheme 2, the modification of the end groups is very similar for both macroinitiators that we made. There is one additional step in the di-functionalized macroinitiator, and that is reduction of the Br end group to an H end group. After reduction to H/H end group, the synthesis of both macroinitiators is virtually the same, the only difference being that twice as much reactant must be used in the reactions with the di-functionalized polymer.

After synthesizing aldehyde terminated P3HT, it was reduced with LiAlH₄ to yield hydroxyl terminated P3HT. The hydroxyl terminated P3HT then undergoes a substitution reaction with BiBB to yield the macroinitiator³.

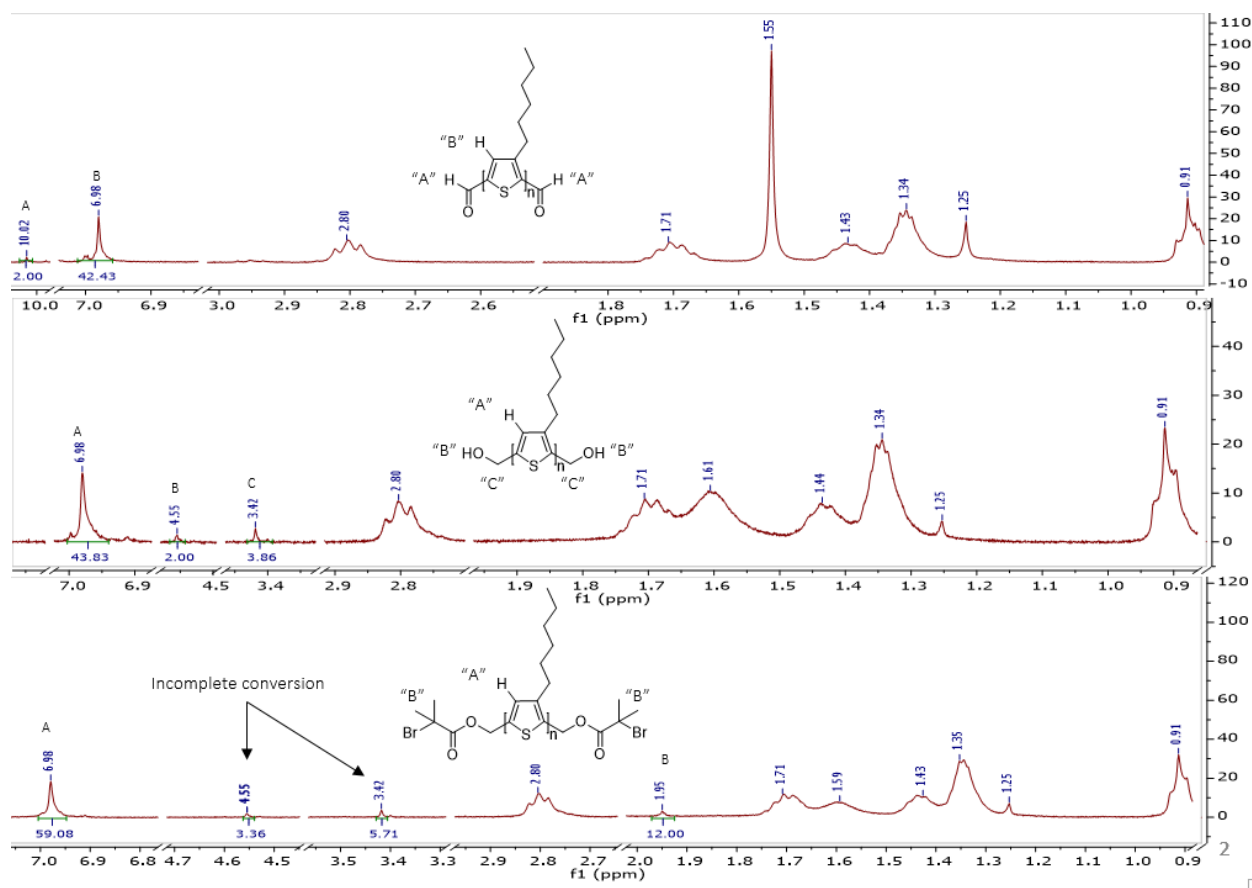


Figure 1: NMR spectra of di-functionalized P3HT end group modifications

To confirm that each reaction had been successfully completed, and to determine the molecular weight of the polymer, NMR spectra were taken after each reaction. Figure 1 shows a sample NMR spectrum of di-functionalized P3HT after each modification to the end groups. By measuring the ratio of the integral of the aldehyde-hydrogen peak to the integral of the thiophene-hydrogen peak, we were able to find the average number of repeat units in each polymer. The molecular weight of the polymer is then calculated from this value. The target molecular weights for mono-functionalized and di-functionalized end groups 5k g/mol and 7k g/mol respectively. We found that the mono-functionalized polymer had a molecular weight of 5k g/mol, and the di-functionalized polymer had a molecular weight of 7.2k g/mol.

These macroinitiators were then used in an ATRP polymerization with TMPM monomer to form the di-block and tri-block. The catalyst used for ATRP, CuBr, is very sensitive to oxygen, and as ATRP relies on an oxidation reduction cycle it is important to avoid oxidizing the CuBr prematurely. A nitrogen atmosphere was used for the polymerization, and the reaction vessel was purged of oxygen using freeze-pump-thaw cycles to degas the toluene. For our initial ATRP reaction, we wanted to create a PTMPM block that was quite large compared to the P3HT block, so a large excess of TMPM monomer was used, and the reaction was allowed to proceed for 18 hrs. The reaction was exposed to oxygen to halt it, and was then precipitated in hexanes. The precipitate was collected, dissolved in a small amount of THF, then precipitated again in hexanes to remove any remaining TMPM. NMR spectra of the precipitates were then taken.

The NMR data showed that the synthesis of PTMPM-b-P3HT was unsuccessful, and that there were still large amounts of monomer present, and virtually no polymer. We believe that ATRP failed to initiate for the mono-functionalized macroinitiator due to poor solubility. In the process of solvent removal after isolating hydroxyl terminated P3HT, we believe that we unintentionally annealed the sample in a glass vial. The sample coated the vial and was difficult to remove, and reluctant to dissolve in solvents that are typically good solvents for P3HT, such as THF.

PTMPM-b-P3HT-b-PTMPM on the other hand was successfully polymerized, and was isolated as a light purple powder that was soluble in DCM, chloroform, and THF. The NMR spectrum showed that we had a PTMPM polymer and P3HT. We calculated the

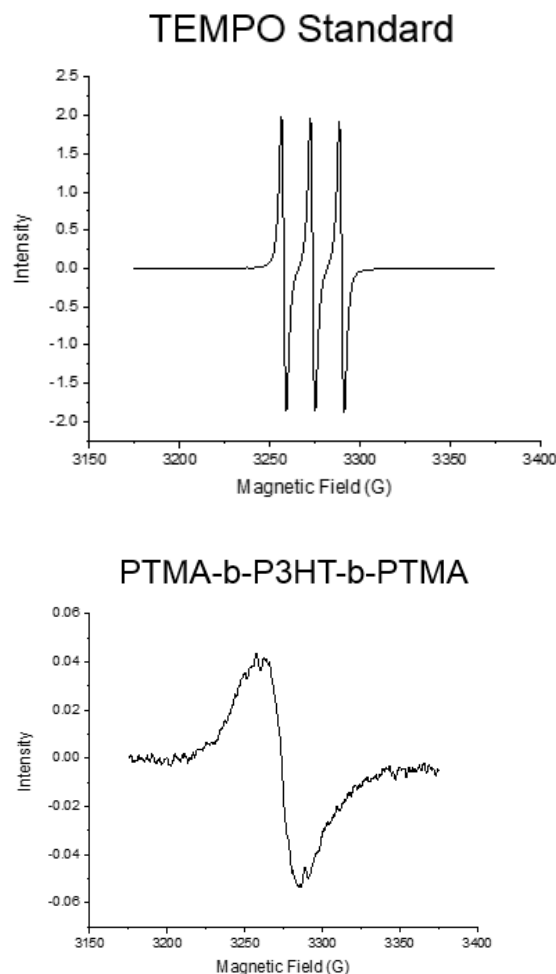


Figure 2: EPR spectra for a TEMPO standard (top) and PTMA-b-P3HT-b-PTMA

molecular weight from this spectra, and found that the polymer had a molecular weight of 160k g/mol. The PTMPM-b-P3HT-b-PTMPM was then oxidized with mCPBA in DCM, yielding a yellow powder. The resulting PTMA-b-P3HT-b-PTMA was then analyzed EPR to determine the conversion of the amine pendant groups on the PTMPM block to stable radical pendant groups. Figure 2 shows the EPR spectrum for a 0.0005M TEMPO standard, and a 0.0005M PTMA-b-P3HT-b-PTMA sample. The conversion of the amine to stable radical can be calculated by finding the area of the double integral of both of these graphs, and then taking the ratio of the two as the percent conversion per unit weight. After doing this calculation, we found that we achieved an amine to stable radical conversion of 13.6%. We believe that this number is as low as it is because mCPBA is a strong oxidant, and potentially over oxidized the stable radical groups. We are

investigating alternative reagents to use as oxidants to overcome this problem.

Azide-Alkyne “Click” Chemistry

For this synthetic route, rather than create a macroinitiator and grow the PTMPM block off of it, we would grow the two polymers separately, and then “click” them together. Alkyne azide “click” chemistry was chosen as the method by which the two polymers would be combined into a block copolymer, due to the high yields that the reaction is known for.

To grow the azide functionalized PTMPM, an initiator with an azide group was synthesized. Polymerization of the TPM monomer was initiated from this molecule to create the azide functionalized PTMPM polymer.

To synthesize the alkyne functionalized P3HT, a procedure very similar to the synthesis of P3HT with H/Br end groups was followed. Rather than quenching the reaction with dilute HCl, Ethynylmagnesium chloride was added to the reaction vessel, allowed to stir for three minutes, then precipitated into MeOH. The polymer was not purified using Soxhlet extraction as the heat has been shown to catalyze a coupling reaction between the azide end groups, but was rather rinsed with MeOH in a filter. It was also kept in a cool room for storage to prevent this coupling reaction from occurring⁵. We confirmed the presence of the alkyne end group using NMR, and calculated that the molecular weight of the polymer to be 7.9k g/mol.

We were interested to see the effect of oxidizing the PTMPM polymer to PTMA before clicking it with P3HT versus oxidizing after they had been clicked. Two click reactions were assembled, one using azide functionalized PTMPM, and the other using azide functionalized PTMA. These reactions have been precipitated, but have not yet been analyzed at the time of writing.

CONCLUSIONS

In the course of this project, we developed a procedure for the synthesis of PTMA-b-P3HT-b-PTMA, and P3HT-b-PTMA by ATRP from a P3HT macroinitiator. The radical tri block PTMA-b-P3HT-

b-PTMA was successfully synthesized, and characterization by EPR shows that it has a 13.6% conversion of amines to stable radicals. The polymer had a molecular weight by NMR of 160k. P3HT-b-PTMA was not successfully synthesized after ATRP failed to initiate from the macroinitiator. Additionally, we synthesized azide functionalized PTMPM and alkyne functionalized P3HT that could be used in a “click” reaction. The results of the PTMA-b-P3HT and PTMPM-b-P3HT click reactions are being investigated at the time of writing.

Future work on this project should focus on varying the ratio of the P3HT block and the PTMA block to study the effect that the block ratios have on the material properties. Additionally, a new method to achieve a higher conversion of amine groups to stable radical groups.

ACKNOWLEDGEMENTS

I would like to thank Yiren Zhang, as well as the Ober lab for their support with this project. I would also like to thank Dr. Christopher Ober for the opportunity to work in his laboratory, as well as the entirety of the Ober lab Group. Finally, I would like to thank the Cornell Center for Materials Research and NSF REU program (DMR-1460428 and DMR-1120296) for funding me through this REU program.

REFERENCES

- [1] Tomilson, E.; Hay, M.; Boudouris, B. *Macromolecules*, **2014**, 47 (18), 6145-6158
- [2] Miyakoshi, R.; Yokoyama, A.; Yokozawa, T. *Macromol. Rapid Commun.*, **2004**, 25, 1663-1666
- [3] Surin, M.; Coulembier, O.; Tran, K.; De Winter, J.; Leclere, P.; Gerbaux, P.; Lazzaroni, R.; Dubois, P. *Organic Electronics*, **2009**, 11, 767-774
- [4] Kumari, P.; Khawas, K.; Hazra, S.; Kumar Kuila, B. *J. Polymer Science, Part A*, **2016**, 54, 1785-1794
- [5] Lohwasser, R.; Thlakkat, Mukundan. *Macromolecules*, 2011, 44, 3388-3397

Integration of Fibers with Elastomers for Programmable Shape-Changing Surfaces

Ceron, Steven

Abstract— A novel type of twisting actuators have been fabricated by embedding specially patterned Kevlar fiber spirals into an Eco-flex substrate. These actuators have been inflated in order to produce controlled twisting and expanding motions. The studies presented demonstrate how various properties of the actuators change as a function of the curvature and number of fiber spirals. It is also shown that optical fibers can easily be incorporated into the actuators, and as a result, distinct relationships can be observed between the signal transmission and the extrinsic physical properties of the actuators.

Index Terms—Eco-flex, twist, actuator, fiber

I. INTRODUCTION

THE twisting actuators that are presented in current literature consist of fiber-reinforced, cylinder-like, soft actuators that perform a twisting motion across a large length. When miniaturized, these twisting actuators become very difficult to precisely fabricate in order to create reproducible twisting motions. As a result, it is not optimal to use this design for accurately programmed shape-changing surfaces. A fabrication method is presented for a soft twisting actuator that is able to perform its rotating mechanism across a smaller length scale and can be manufactured in a much smaller amount of time than the preceding designs.

The soft twisting actuators presented are also fiber-reinforced, but rather than starting off as cylinder-like structures, they begin as a flat substrate. When the substrate is inflated, the actuator rotates to a maximum angle that is entirely dependent on the curvature of the fibers' spiral pattern. In addition, the inflation of the actuator leads to a specified shape that can also be derived from the pattern of the fibers. This will be discussed in greater detail in the Discussion section.

There are a number of measurements that have been taken from the actuators, including torque, maximum angle of rotation, and surface area. Although each of these measurements gives us a clear understanding of how the actuators twist and expand with a given set of parameters, there is still a missing piece to the story. How can all of this information be extracted during the whole process of actuation from one lone measurement? A method for completing this objective is to embed an optical fiber into the substrate and monitoring the signal input and output through the fiber as the actuator rotates and expands. The basis for a relationship between the signal transmission data and the other

measurements is presented as a feature that would allow for the prediction of the actuator's current state at any point during its actuation.

II. PROCEDURE

Fabrication of Twisting Actuators

The following sections describe the methods by which the inflatable twisting actuators were fabricated.

A. Kevlar Fiber Sewing

A set of Matlab programs were written to process various parametric equations and create specific spiral patterns that could be interpreted by a computer-controlled sewing machine. The respective designs were loaded onto the sewing machine so that Kevlar thread could be sewn onto water-soluble plastic, using a secondary water-soluble thread as well.

B. Eco-flex Substrate

A plastic 3D-printed circular mold of 89 mm in diameter and 2 mm in depth was used for the first layer of 20 grams of Eco-flex 10. The water-soluble plastic with the Kevlar thread sewn on it were embedded on the viscous liquid and placed in the oven for approximately 30 minutes. Afterwards the water-soluble plastic and thread were washed off with water.

A laser-cut piece of acrylic was then placed on top of the plastic mold and a second layer of 20 grams of Eco-flex 10 were poured over the embedded Kevlar thread. The Ecoflex was placed in the oven for an additional 30 minutes.

C. Torque Data

The edge of a wooden stick of 0.42 grams (negligible weight when compared to the mass of the actuator) and a length of 0.14 cm was super-glued to the center of each actuator. Each actuator was rotated to a specific starting angle that was increased from 0 to the actuator's maximum angle of rotation, by increments of 10°. When the internal pressure was raised to 2psi, the actuator rotated and the force of the stick against a scale was measured. With each of these measurements, the torque was computed and reported.

D. Angle and Surface Area Data

The angle and surface area data was entirely computed with the use of image analysis programs. The angle of rotation as a function of time was computed with periodic images taken from the top of the twisting substrates. The surface area calculations were obtained from images taken from the side, and processed through Matlab scripts.

III. RESULTS

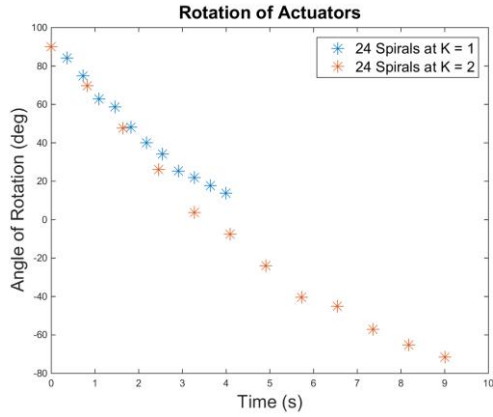


Fig. 1. Angle of rotation as a function of time, for two actuators with equal number of spirals and an increasing curvature value.

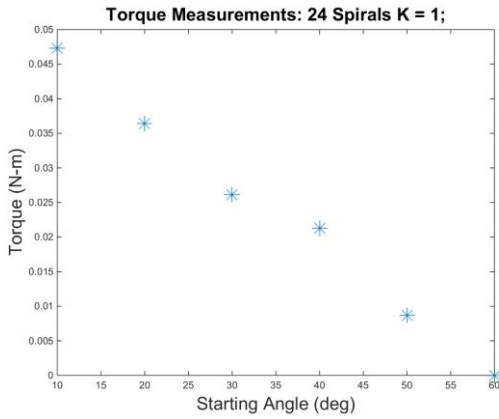


Fig. 2. Torque calculations for an actuator with 24 spirals and a curvature ‘k’ value of 1, inflated at 2psi.

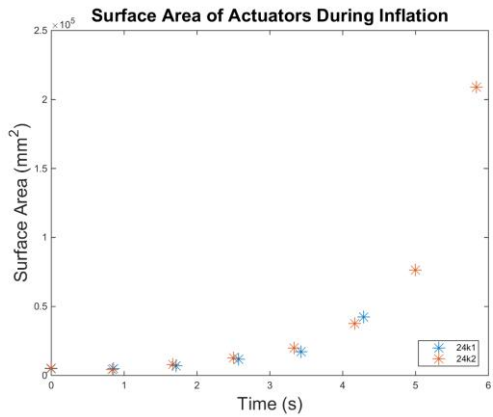


Fig. 3. Surface Area calculations for two actuators with 24 spirals and ‘k’ values of 1 and 2, inflated at 10 psi.



Fig. 4. Images of three twisting actuators with 24 spirals and a ‘k’ value of 1 on the left, 24 spirals and a ‘k’ value of 2 in the center, and 18 spirals and a ‘k’ value of 3 on the right. Each of these actuators was inflated at 10 psi.

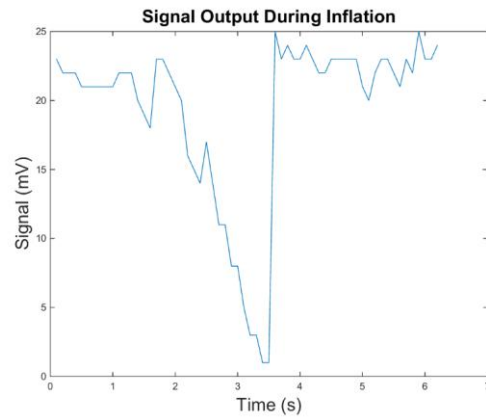


Fig. 5. Output signal from the photodiode as an actuator with 24 spirals and a curvature ‘k’ value of 1 was inflated at 10psi and then deflated.

IV. DISCUSSION

The design of each actuator presented in this study was first created with the use of the following parametric equations, which generated the coordinates that were then fed to the computer-controlled sewing machine.

$$x(t) = -15t \cos\left(kt + \frac{n}{4\pi m}\right)$$

$$y(t) = -15t \sin\left(kt + \frac{n}{4\pi m}\right)$$

The ‘x’ and ‘y’ coordinates for the stitches operated as functions of ‘t’, an incremented angle value between 0 radians and $7/8\pi$ radians. The parameter, ‘k’, which was chosen to have values of 1 and 2 for this study, determines the curvature of the spiral lines, and thus determines the maximum angle of rotation for each of the twisting actuators. The parameter ‘m’ is the number of spirals, and ‘n’ iterates from 0 to ‘m+1’. These two parameters are simply for the sake of sewing the intended number of spirals.

If the value of ‘k’ was reduced all the way down to zero, the spiral lines would instead be replaced by straight lines, and thus no rotation would occur. The rotation of the actuator can be attributed to the unwrapping of the inextensible fibers as the surrounding elastomer expands. If there was no maximum strain on the elastomer, then each twisting actuator would reach the point where the fibers fully unwrap to form straight lines.

In Figs. 1-3, there seems to be a clearly defined trend in each of the measurements as each of the actuators is inflated over time. Each of the measurements shown in the figures follows a trend that can easily be quantified, which as a result provides a great framework upon which to build relationships between the signal output in the optical fibers and each of the measurements presented in these figures. The clear identification of the relationships will lead to greater control in the twisting mechanisms.

In the images presented in Fig. 4, it is evident that a more defined conical structure arises as the value of ‘k’ increases. This is simply due to the fact that a higher curvature value for

the spirals will result in smaller spacing between the individual fibers. When there is less space between two fibers, the elastomer is able to expand less between them. By nature of the geometry of the spirals, there will always be less spacing between spirals, closer to the center, than closer to the edges. As a result, the larger expansion at the edges of the substrate and the smaller expansion at the center will result in the conical structure clearly defined in Fig. 4.

The signal transmission data from the optical fiber embedded in an actuator, shown in Fig. 5, displays how the output signal quickly decreases around the 1.5 second mark as the substrate is inflated, and then increases again when it is deflated. This data will be analyzed in the future in greater detail to form connections between the signal output and the previous measurements reported.

V. CONCLUSION

The twisting actuators presented demonstrate relationships between the number of spirals embedded in a substrate and the curvature value of each of those spiral designs. The use of these actuators could have applications in various subfields of soft robotics where a twisting mechanism must be controlled to a great extent. In addition to the twisting motion of the actuators, the spiral patterns prove to be very useful in creating reproducible shapes. Preliminary results on the signal transmission through the optical fiber were presented, and have set the basis for future work in defining a clear relationship between various properties of an actuator's twisting mechanism and the value of the output signal. The integration of the optical fibers will allow for quick implementation into control systems.

Bone Mechanobiology

Kyle Cripps ^a, Erin Cresswell ^{b,c}, Christopher Hernandez ^{b,c}

^a Department of Mathematical Sciences, El Camino College, Torrance, CA 90506

^b Department of Mechanical and Aerospace Engineering, Cornell University, Ithaca, NY 14853

^c Menig School of Biomedical Engineering, Cornell University, Ithaca, NY 14853

ABSTRACT

Bone is often a source of inspiration in the field of materials science because of its optimized structure and unique adaptive functionality. Bone is both lightweight and strong, allowing for mobility while minimizing fracture risk. Additionally, bone has the unique ability to change its structure in response to the mechanical stress and strain delivered by its environment. For example, physical exercise leads to increased bone density because stronger bone is required to withstand rigorous physical exertion. Conversely, lack of physical exercise will lead to resorption of bone that is not being used. While this behavior of bone has been observed and studied at the macroscopic level, little is known about how bone responds at the local, microscopic level. We can study this behavior by using a specialized device to apply cyclic mechanical loads to vertebral bone in live animals in order to stimulate bone formation. Using high resolution micro-computed tomography (micro-CT) imaging and finite element modeling (FEM) of the vertebrae, we are able to approximate the mechanical stress or strain that each region of bone experiences during bouts of mechanical loading. Using high resolution fluorescent imaging we are also able to identify locations of bone formation and thus are able to spatially associate bone formation and mechanical stress or strain at the microscopic level. Results showed a correlation between increased bone formation and higher SED at the periosteal surface of the vertebrae, but there appeared to be no correlation between bone formation and SED at the endosteal surface. Our results suggest that there may be biological factors that have a greater influence on bone formation responses than mechanical stimulation. Better understanding how bone behaves at the microscopic level may allow for the development of pharmaceuticals that can target specific bone forming pathways and facilitate bone growth in patients with osteoporosis.

INTRODUCTION

Bone is a unique material because it is mechano-responsive, meaning that it has the ability to change physically in response to mechanical stimuli. Within bones is a complex network of specialized cells that are responsible for the formation and removal of bone tissue. Osteoblasts are bone cells that produce new bone matrix, while osteoclasts remove bone where it is no longer needed. It is believed that osteocytes are instrumental in the regulation of bone formation because they are able to sense mechanical stimuli and respond by sending inhibitory or promotion signals to osteoblasts and osteoclasts. Osteocytes in regions of relatively low mechanical stress or strain will send signals that inhibit bone formation, while osteocytes in regions of high mechanical stresses and strains will send signals that promote bone formation.

Therefore, regions of bone that experience relatively high magnitudes of mechanical loading will form more new bone than regions of the same bone that experience relatively low magnitudes of mechanical loading.¹ Consequently, regions of bone under high stresses and strains will better be able to resist deformation and fractures.

Few *in vivo* studies have been done on healthy bone at the microscopic level. By conducting experiments on live animals, we can gain a deeper understanding of the processes that regulate bone growth in healthy bone. Once a deeper understanding of healthy bone is developed, it will be easier to conduct studies on osteoporotic bone and to identify differences in how osteoporotic and healthy bone behaves. With these differences identified, bone forming pathways could potentially be targeted by drugs that can allow for the facilitation of bone growth in patients with osteoporosis.

This study focuses specifically on the effects of mechanical loading on the caudal 8 (Cd8) vertebra in rats. Vertebrae are comprised of a dense exterior cortical shell (“compact bone”) filled with a porous cancellous interior (“spongy bone”) and bone marrow. On the interior surface of the cortical shell is a thin membrane called the endosteum, under which the endosteal surface of the cortical shell is found. Likewise, on the exterior surface of the cortical shell is the periosteum, under which the periosteal bone surface can be found (See figure 1). The endosteum and periosteum provide nutrients for the bone cells that reside at the endosteal and periosteal bone surfaces.

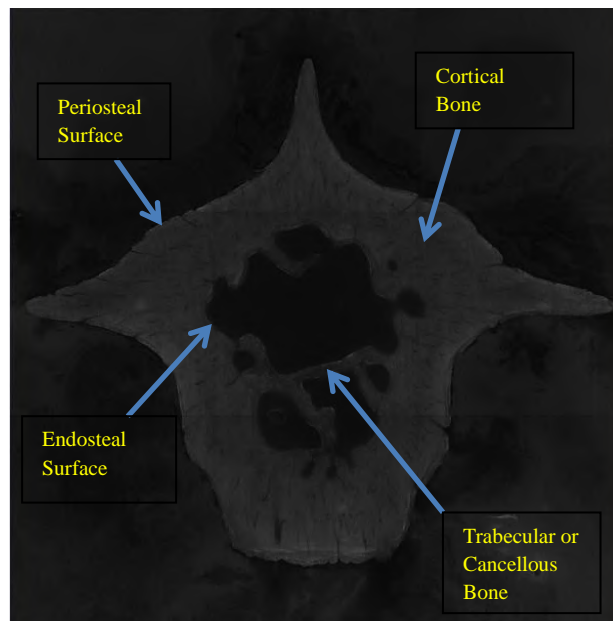


Figure 1: Transverse cross section of the caudal 8 vertebrae of a rat

In this study, we used images of bone formation and finite element modeling to analyze the mechano-responsiveness of bone at the endosteal and periosteal surfaces of the Cd8 vertebra in rats.

METHODS

In vivo mechanical loading and injection of fluorescent dyes

Prior to mechanical loading, a fluorescent marker (oxytetracycline) was injected into all (pre-loaded and control) rat specimens. Three days later, cyclic mechanical loading was applied to the eighth caudal (Cd8) vertebrae of non-control specimens for three consecutive days (days 0, 1, and 2). Another fluorescent marker, calcein, was injected into all (loaded and control) specimens on day 5, and again on day 10. On day 14, the rat specimens were euthanized and their Cd8 vertebrae were collected for imaging.² Wherever new bone is formed after the injections, the fluorescent markers will be trapped underneath new bone, while the fluorescent marker will be “cleaned away” by natural processes where no new bone is formed.

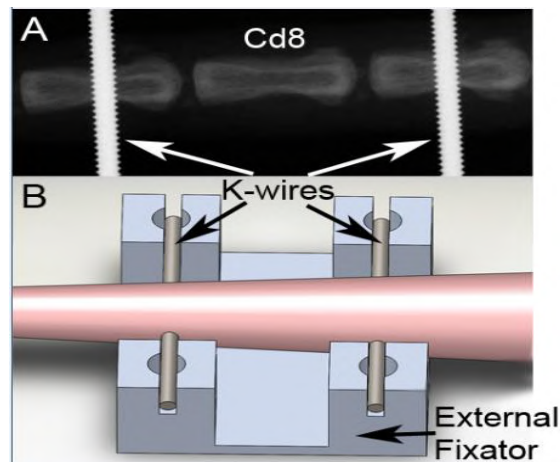


Figure 2: Device used to apply cyclic mechanical loading to Cd8 vertebrae in rats²

Micro-CT scans and high resolution serial milling

The Cd8 vertebrae of the specimens were cleaned and micro-CT images with a voxel resolution of 11x11x11 microns were taken. Serial milling was then used to obtain high resolution (0.7x0.7x5.0 microns) fluorescent images of the vertebrae.² The oxytetracycline and calcein bone markers injected into the rats are known to fluoresce at different wavelengths, so for each cross sectional slice of the vertebrae, a different colored light was used to obtain each set of calcein and each set of oxytetracycline images. Because two fluorescent markers were injected at different time points prior to and following mechanical loading, we are (in theory) able to differentiate between natural bone forming events that were already in progress before loading and new bone forming events that were stimulated by mechanical loading (we were not able to implement this in our analysis due to time constraints).

Finite Element Modeling

Finite element models were then generated from the micro-CT images of each specimen to determine the stresses and strains at each individual bone voxel.²

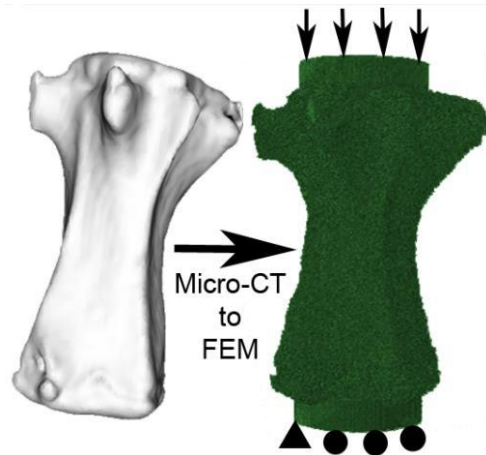


Figure 3: Finite element models were generated from micro-CT images²

Resampling and Image Registration

At this point, all necessary data had been acquired, but we could not conduct an analysis because our FEM, micro-CT, and bone formation (fluorescent) images were not on the same coordinate axis and did not have the same pixel size, so we could not do an analysis relating these different sets of images. This problem was easily resolved by resampling (or “resizing”) the images and image registration. Micro-CT and FEM image stacks were resampled to the same voxel size as the fluorescent images and affine registration was performed on the micro-CT and FEM image stacks to find the matrix of transformation for each specimen. Transformation matrices were then applied to the image stacks resulting in a one-to-one correspondence between each voxel in FEM, fluorescent, and micro-CT image stacks of each specimen.



Figure 4: Micro-CT images were resampled and transformed onto the same coordinate axis as fluorescent images

Image Processing

Following resampling and image registration, Matlab software was written to process images and extract data to be analyzed. Some Matlab code was adapted from a previous study involving only the cancellous bone of the rat vertebrae.²

- i. Prior to image processing, masks of the cancellous regions were traced so that cancellous bone could be studied separately from cortical bone.³ See figure A.
- ii. Cancellous masks and micro-CT bit masks were combined to remove cancellous bone and a majority of background noise from the fluorescent images. See figures B, C, D, and E.
- iii. Remaining artifacts were removed from the background of the image and small holes (caused by nutrient foramen) were removed from the interior of the cortical shell. See figure E.
- iv. A sobel edge detection algorithm was used on a bit mask of the resulting cortical shell to identify edges, resulting in two sets of edges.
- v. Additional algorithms were applied to separate the endosteal and periosteal edges so that they could be analyzed separately.
- vi. Bit masks of endosteal and periosteal edges were combined with bone formation and FEM images to gather data relating bone formation with strain energy density at the endosteal and periosteal surfaces of each specimen. See figures F and G.

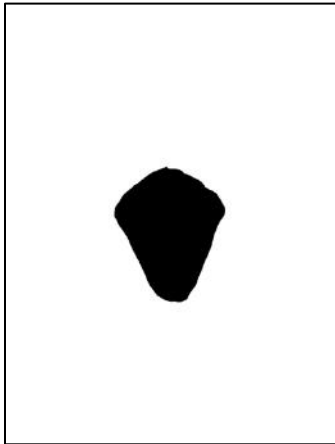


Figure A: traced cancellous mask

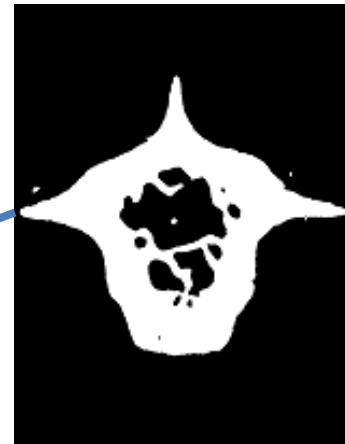


Figure B: micro-CT mask



Figure C: mask of cortical shell



Figure C

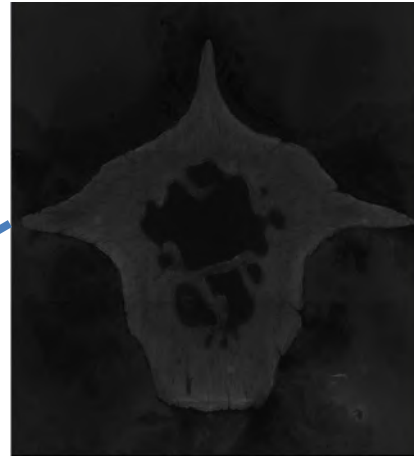


Figure D: original image



(+ additional filtering)

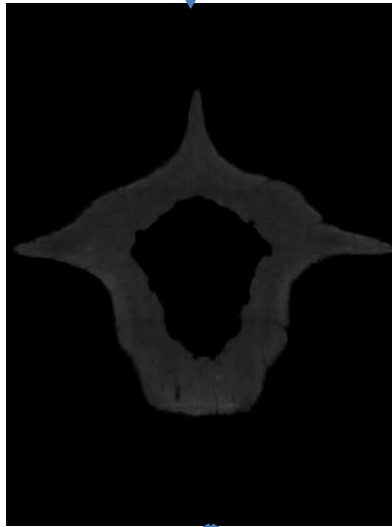


Figure E: final image of cortical shell



(+ edge detection and fluorescent images of bone formation markers)

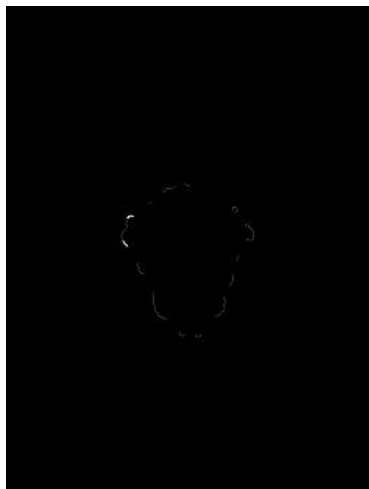


Figure F: Bone formation on endosteal surface

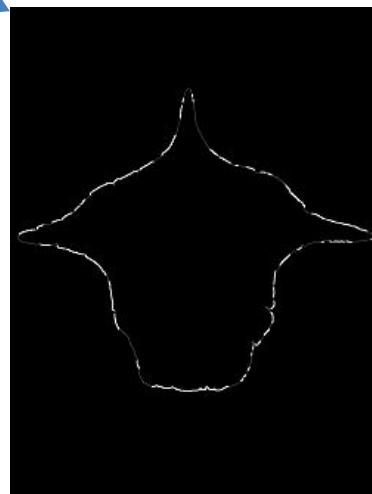


Figure G: Bone formation on periosteal surface

An important measurement that we collected from our data was the amount of mineralizing surface (where new bone was formed) per bone surface (total bone surface, including newly formed bone and old bone), which will be abbreviated as MS/BS. We expect the loaded specimens to have higher MS/BS values due to the adaptive response by cells in the bone. Another important measurement we collected from our data, specifically from the finite element models (FEM), was the strain energy density (or SED) of each bone voxel. A detailed understanding of SED is not necessary: For the purposes of this paper, it is sufficient to know that higher SED values correspond with regions of higher mechanical stresses and strains, while lower SED values correspond with regions of lower mechanical stresses and strains. We expect bone forming surfaces to be at a higher SED than surfaces which did not form new bone.

RESULTS

It was found that the average MS/BS of the endosteal surface in the loaded specimens was 3.34% while the average MS/BS of the endosteal surface in the control specimens was 3.20% (See figures 6 and 8). The average MS/BS of the periosteal surface in the loaded specimens was 53.01% while the average MS/BS of the periosteal surface in the control specimens was 48.60% (See figures 7 and 8).

Histograms were generated to gather the following data relating SED and bone forming and non-bone-forming surfaces of the cortical shell. Due to the nature of the histograms (having right-skewed distributions in most cases (see figure 4 below)), the geometric mean will be used to describe the data rather than arithmetic mean, which is not very representative of a skewed distribution.

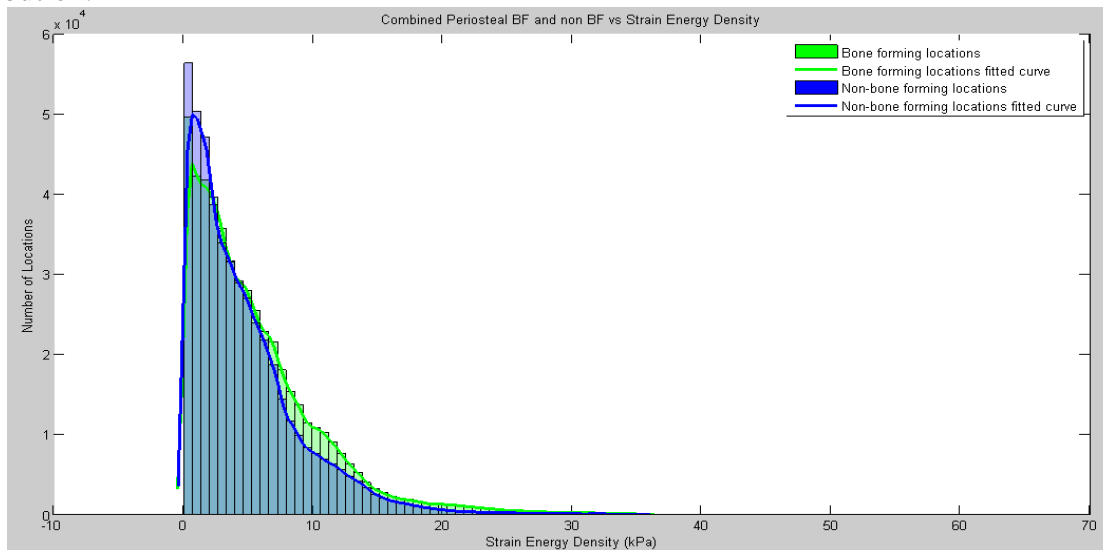


Figure 5: Right-skewed histogram of SED values at bone-forming and non-bone-forming locations on the periosteal surface

The geometric mean strain energy density (SED) at the periosteal surface was 3.34×10^3 Pascals (Pa) while the geometric mean SED at the endosteal surface was 3.64×10^3 Pa (See figure 9).

The geometric mean of the SED at bone forming locations on the periosteal surface was 3.29×10^3 Pa while the geometric mean SED at non-bone forming locations on the periosteal surface was 2.68×10^3 Pa (See figure 10).

The geometric mean of the SED at bone forming locations on the endosteal surface was 2.52×10^3 Pa while the geometric mean SED at non-bone forming locations on the endosteal surface was 3.12×10^3 Pa (See figure 11).

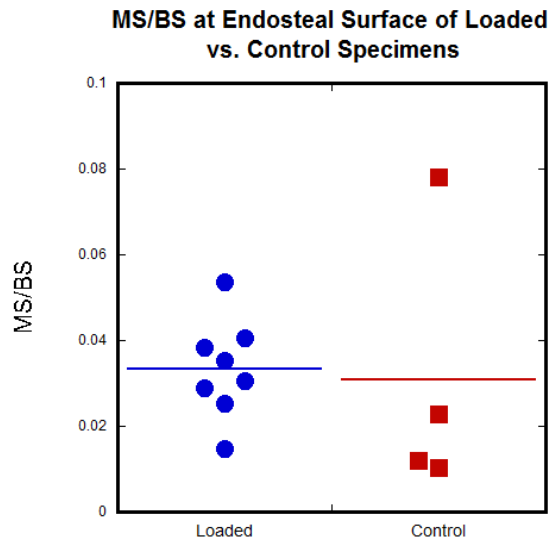


Figure 6

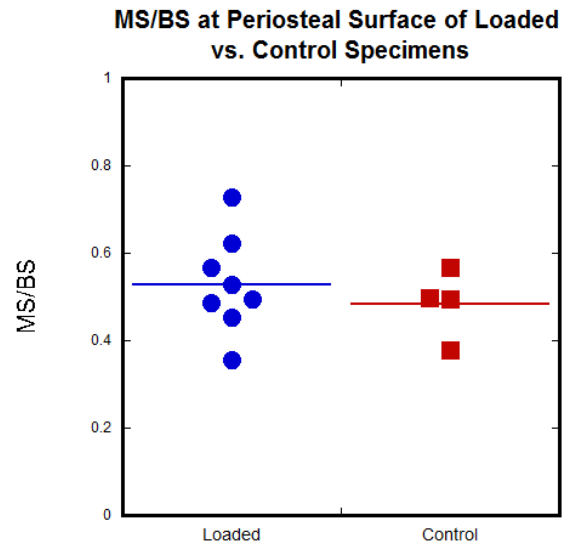


Figure 7

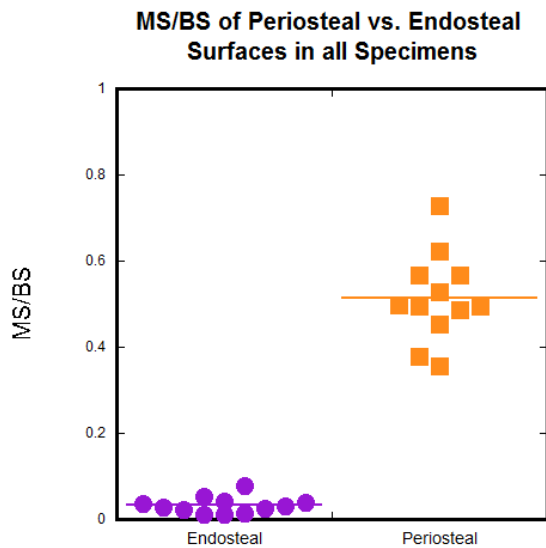


Figure 8

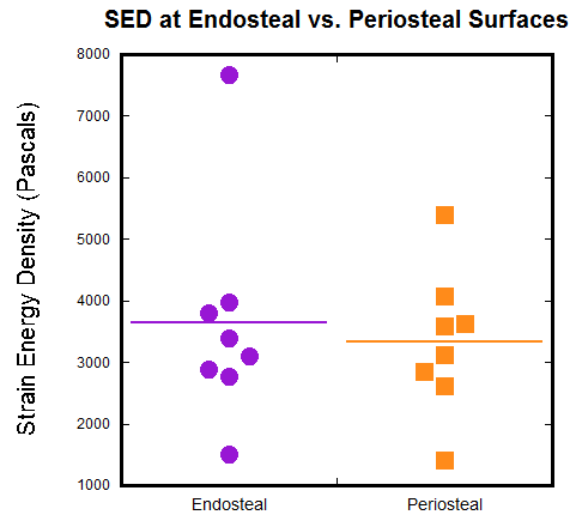


Figure 9

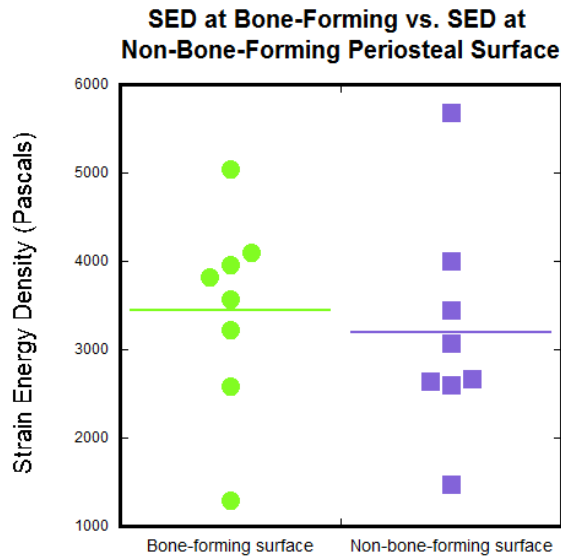


Figure 10

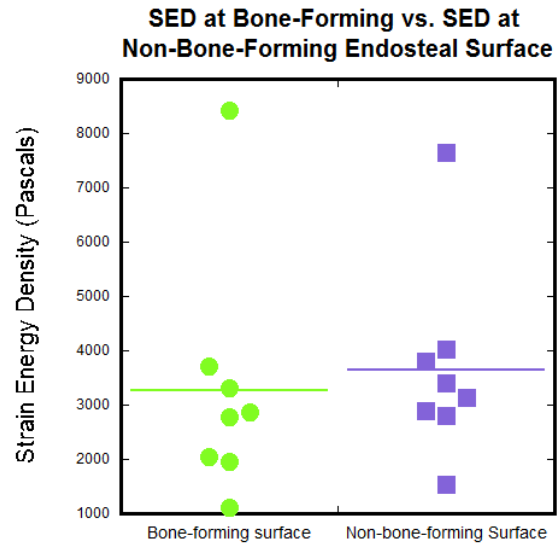


Figure 11

DISCUSSION, SIGNIFICANCE, AND FUTURE ANALYSIS

Although there was an overall slight increase in bone forming surface in the loaded specimens, it is questionable whether this increase is large enough to definitively say that mechanical loading directly influenced bone formation in the loaded specimens. This may be due to other biological factors that significantly influence bone formation at these surfaces. For example, osteocytes at the endosteal and periosteal surfaces may be more sensitive to fluid flow than to mechanical stimulation.

From a mechanics standpoint, one would expect the periosteal surface to be at an overall higher SED than the endosteal surface. Since the endosteal surface is closer to the central axis of the vertebrae, it should experience less stresses and strains because it will bend slightly less than the periosteal surface during mechanical loading. However, results show that the periosteal surface is at equal or slightly lower SED magnitudes than the endosteal surface. This suggests that the difference between SED at the periosteal and endosteal surfaces may be too small to be able to accurately observe with our data. However, from our data we know that more new bone was formed at the periosteal surfaces than at the endosteal surfaces. This could mean that mechanical stimulation does not play a very strong role in bone formation and that maybe more studies need to be done to identify important differences in the biological environments at the endosteal and periosteal surfaces.

At the periosteal surface, bone forming locations are, on average, at higher SED levels than non-bone forming locations. This is consistent with the idea that mechanical loading stimulates bone formation at the local level. However, data relating bone formation and SED at the endosteal surface show the opposite effect. Also, there was much more bone formed at the periosteal surfaces than at the endosteal surfaces in all specimens. These data suggest that the endosteal surface may be much less mechano-responsive than the periosteal surface, possibly due to the differences in the biological environments at each surface. At the endosteal surface, bone is

formed by osteoblasts that need to be recruited from deeper in the bone marrow by osteocytes. At the periosteal surface, osteoblasts reside in the periosteum, and are readily available to form new bone when they are needed. Therefore the endosteal surface may be less sensitive to mechanical stresses and strains than the periosteal surface, and may instead be more sensitive to fluid flow within the bone marrow, for example.

Using the images that have been acquired following the in vivo rat experiments, and using Matlab software that a colleague has been developing³, we will also be able to identify osteocyte lacunae (microscopic caves in bone in which osteocytes reside). Now that we have spatially associated stress and strain (SED) and bone formation at the endosteal and periosteal surfaces, the next step will be to determine how osteocyte lacunar density correlates with SED levels and bone formation locations. Incorporating osteocyte lacunar density into our overall analysis may provide some additional insights into the bone forming processes of the intricate network of cells in bone.

Acknowledgements

Live animal experimentation and image acquisition were done by graduate students in the Hernandez Lab prior to my work. I was mentored and advised by graduate student Erin Cresswell and faculty member Christopher J. Hernandez. This work was supported by the Cornell Center for Materials Research with funding from the NSF Research Experience for Undergraduates program (DMR-1460428 and DMR-1120296).

References

- (1) Bettine Willie; Georg N. Duda; Richard Weinkamer. *Bone Structural Adaptation and Wolff's Law*. 2013.
- (2) E.N. Cresswell; M.G. Goff; T.M. Nguyen; W.X. Lee; C.J. Hernandez. *Spatial Relationships between bone formation and mechanical stress within cancellous bone*. 2016.
- (3) Adrian Alepuz (Undergraduate from the Department of Mechanical and Aerospace Engineering at Cornell University)

Brushing Up on Polymers: Controlling Molecular Weight Distribution to Manipulate Polymer Structures

Hazel Davis¹, Dillon Gentekos², Brett Fors²

¹*Chemistry, Furman University, Greenville, SC*

²*Chemistry and Chemical Biology, Cornell University, Ithaca, NY*

Abstract

Polymer brushes are a class of polymer structures that offer a wide variety of interesting phase behavior and morphological properties, however, the synthesis of these structures is limited by the randomization of chain lengths along the polymer backbone. As structures with a wide range of molecular architectures offer a multitude of promising applications, the synthesis of these materials was investigated. Previously, the Fors group has shown that by temporally regulating the addition of initiator species, shifts in the MWD shape are observed in living controlled polymerizations. Synthetic routes for the creation of new dual functional monomer/initiators in living controlled tandem polymerization were developed in order to synthesize tapered brush polymer structures, where manipulation of the shape and breadth of the molecular weight distribution by temporal initiation provides access to novel polymer structures. Nitroxide-mediated polymerization (NMP) and cationic ring opening polymerization (CROP) were investigated for this purpose and a new monomer/initiator synthesized was intended to feature a polyoxazoline (POZ) backbone with tethered polystyrene (PS) branches. This NMP/CROP monomer/initiator was synthesized in three steps, however, after polymerization a bimodal distribution was observed in the gel permeation chromatography (GPC) results, and faster and more versatile ring opening polymerization processes were studied further. New monomer/initiator structures were synthesized, including the synthesis of a six membered aryl lactone treated with a NMP radical. These structures will be further characterized by GPC and nuclear magnetic resonance (NMR) spectroscopy before polymerization.

Introduction

In the past few decades, the field of polymer synthesis has made tremendous innovations in the preparation strategies of materials with a variety of physical properties and attributes. A key parameter of polymers, the dispersity (\mathcal{D}), or the normalized standard deviation of molecular weights in the sample⁹ has been linked to the control of viscosity, material processability, and nearly all block copolymer properties.¹³ Despite the theoretical

suggestions¹¹ that molecular weight distribution affects morphology, previous efforts center around the manipulation only of the dispersity, and not the exact shape of the molecular weight distribution. It is thus of vital importance to develop strategies that will allow for the careful tuning of dispersity and molecular weight distribution shape in polymer synthesis, in order to create exciting new materials with emerging properties.

A number of synthetic avenues have been explored in order to create polymers with well-defined molecular weight distributions. These techniques have revolutionized polymer synthesis and provided chemists with advanced control over molecular weight distribution, composition, topology, and chain-end functionalities.^{12,18} Additionally, with well-controlled polymerization techniques comes the ability to expand polymer architectures to stars, cycles, combs, and brushes.¹² One such type – polymer brushes, in which polymer chains are bound to the backbone of a linear polymer strand or other surface – have been shown to possess unique physical properties and phase behavior.¹⁶ These shapes offer a variety of functionalities in the modern world, from biomedical films that prevent bacterial adherence to nanotechnology applications in the enhancement of sensors,¹ making easy and efficient synthesis techniques of large research interest. Previous synthesis efforts however have been limited to random distributions of polymer branch chain lengths along the polymer backbone.^{3,5} (**Figure 1.1**)

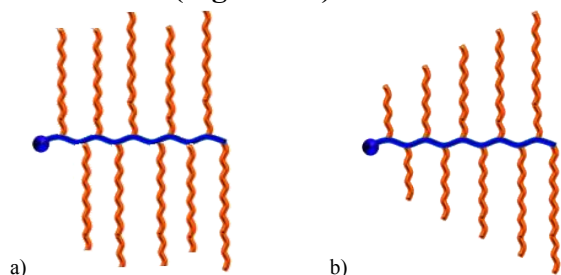


Figure 1.1: a) Current approach to brush polymers and b) intended goal of previously inaccessible tapered brush polymers.

Previously, the Fors group has shown that by using temporal regulation for the process of chain initiation, it was possible to achieve great control over the polymer chain sizes, polydispersities, and MWD shape.^{6,9} (**Figure 1.2**)

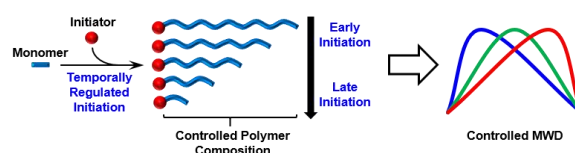


Figure 1.2: Previous research has shown that temporal regulation of initiator species can cause shifts in MWD shape^{6,9}

By manipulating the rate of addition for the initiator species, it is possible to control the growth of polymer chain lengths, and accordingly shift the molecular weight distribution shape. This method has been shown to be successful for both anionic and radical polymerization techniques, and in order to synthesize previously inaccessible polymer shapes, tandem polymerization processes will be used. By synthesizing dual functional structures where the initiator of one polymerization is tethered to the monomer of the other, and then metering in the addition of this monomer/initiator structure in the same fashion seen previously, we hope to engineer a method that will allow the synthesis of unique molecular weight shapes that in turn will possess a range of physical properties.

Experimental

General Analytical Methods

Polymer samples were analyzed using a Tosoh EcoSEC HLC 8320GPC system with two SuperHM-M columns in series at a flow rate of 0.350 mL/min with THF as the eluting solvent. Number average molecular weight (M_n), weight average molecular weight (M_w), and dispersity values were calculated from refractive index chromatograms against TSKgel polystyrene standards. Conversions were determined from NMR spectra recorded on either a Varian Mercury-300 or Varian Mercury-400 NMR spectrometer in $CDCl_3$.

ATRP Temporal Regulation Studies

All reactions were carried out under an inert atmosphere unless otherwise stated. Methyl methacrylate (MMA) and acrylic acid methyl ester (methyl acrylate) were purchased from Sigma Aldrich and TCI America, respectively, and filtered over a column of basic alumina to remove the inhibitor before use. Tris(2-dimethylaminoethyl)amine (Me₆TREN) was purchased from Alfa Aesar and filtered over a column of basic alumina prior to use. N,N,N',N'',N'''- Pentamethyldiethylenetriamine (PMDETA) and ethyl 2-bromoisobutyrate (EBiB) were purchased from Alfa Aesar and Sigma Aldrich, respectively, and then distilled from calcium hydride under nitrogen prior to use. Mn(salen)Cl was synthesized according to the literature.⁸ Copper(I) bromide and copper(II) bromide were purchased from Alfa Aesar and Strem Chemical, respectively, and used as received. Acetone was purchased from Macron and used as received, and dimethyl formamide (DMF) was used directly from a solvent system. Ag^o strips for catalysis were purchased from Alfa Aesar and were 0.2 mm in diameter, cut to 1 cm lengths.

Synthesis of Poly(methyl methacrylate). In a reaction vial (“A”) fitted with a screw cap and Teflon septa the following were added: stir bar, CuBr₂ (4.7 mg, 0.02 mmol), CuBr (2.7 mg, 0.02 mmol), 0.852 mL acetone, MMA (0.852 mL, 8 mmol), and PMDETA (16.7 μL, 0.08 mmol). In another reaction vial (“B”) fitted with screw cap and septa, measured EBiB (11.7 μL, 0.08 mmol) in 400 μL acetone. Both solutions were degassed by three freeze-pump-thaw cycles following backfill with inert gas. After purging needle three times with headspace from vial “B”, carefully transferred all of EBiB-acetone solution into vial “A”. Placed into 50 °C oil bath for 16 hours. A small aliquot was removed as needed from the reaction mixture for GPC and NMR analysis.

Synthesis of Polymethylacrylate – Control Experiments. First, a stock solution of CuBr₂, Me₆TREN, and DMF was prepared by mixing CuBr₂ (6.4 mg, 0.03 mmol), Me₆TREN (14.4 μL, 0.05 mmol), and 0.52 mL DMF. Solution was shaken, and prepared every 3-4 days. In a reaction vial fitted with screw cap and Teflon septa, pipetted filtered MA (0.63 mL, 7 mol) along with 0.92 mL DMF. To this vial, 28.4 μL of the CuBr₂ stock solution was added, along with a 1 cm length Ag^o strip and stir bar. In a separate reaction vial, “B”, approximately 1 mL of distilled EBiB was added. Both vials were degassed by three freeze-pump-thaw cycles following backfill with inert gas. After purging needle 3x with headspace from vial “B”, degassed EBiB (5.1 μL, 0.03 mmol) was carefully transferred into the reaction vial, and reaction placed in oil bath for 90 minutes at 50 °C. A small aliquot was removed as needed from the reaction mixture for GPC and NMR analysis. *For Initiator Addition Experiments.* Procedures identical to prior, however a solution of EBiB initiator was made in DMF (5.1 μL EBiB per 200 μL DMF) and this solution was degassed three times by freeze-pump-thaw cycles. 200 μL of the degassed initiator solution was drawn into a 1 mL syringe that had been purged with N₂. The syringe was mounted onto a New Era NE-4000 Double Syringe Pump and programmed to the appropriate addition rate profile (**Table 3.1**) The needle was quickly transferred from the stock solution of EBiB to the reaction vial containing the monomer. Immediately after introducing the needle tip to the reaction mixture, the vial was submerged into an oil bath at 50 °C for 90 minutes.

Synthesis of NMP – CROP Monomer/Initiator

The initiator, 2,2,5-Trimethyl-4-phenyl-3-azahexane-3-nitroxide (TIPNO) was purchased from Sigma Aldrich and used as received. Ethanolamine (141-43-5) was purchased from Aesar and distilled under vacuum before use. 4-cyanostyrene (3435-51-6) was purchased from

Acros and was used as received, as well as synthesized in method below. Methyltriphenylphosphonium bromide (98%) was purchased from Aldrich and used as received. Zirconium dichloride oxide ($\text{ZrOCl}_2 \cdot 8\text{H}_2\text{O}$) 99.9% (13520-92-8) and phenothiazine + 98% (PTZ) were purchased from Aesar and used as received. Anhydrous zinc acetate ($\text{Zn}(\text{OAc})_2$), n-butanol, potassium carbonate (K_2CO_3), tert-butyl peroxide, +90% 4-vinylbenzyl chloride, and sodium borohydride (NaBH_4) were purchased from Sigma Aldrich and used as received. ACS Grade toluene and 200 proof ethanol were purchased from VWR and Fluka Chemical Corporation, respectively, and used as received. Sodium bicarbonate and magnesium sulfate were purchased from Mallinckrodt and EMD Millipore, respectively, and used as received. 2 N HCl was purchased from Fisher Scientific and used as received. Dry ice was obtained from Airgas and used as received. Dichloromethane (DCM) was filtered through a column of alumina and passed through activated molecular sieves prior to use.

For synthetic steps, see Figure 3.4.

Synthesis of 4-cyanostyrene (2) Into a 25-mL schlenk bomb, 4-cyanobenzaldehyde (**1**) (0.5 g, 3.8 mmol) was added. Measured (1.6 g, 4.5 mmol) methyltriphenylphosphonium bromide as well as (0.8 g, 5.8 mmol) potassium carbonate into bomb as well. Added stir bars and then evacuated and backfilled with either nitrogen or argon. Quickly replaced the top cap of the schlenk bomb with septa and added 4 mL dry dioxane through the septa using a syringe. Resulting white paste was added to 110 °C oil bath, and let stir for 20 hours. Let cool to room temperature and then filtered through celite, washing through with 150 mL hexanes. Removed excess solvent under vacuum to isolate white crystals, then dissolved in DCM to obtain yellow oil which was run through flash chromatography (hexanes).

Synthesis of 2-(4-ethenylphenyl)-4,5-dihydro-oxazole (3) using $\text{ZrOCl}_2 \cdot 8\text{H}_2\text{O}$. Into reaction vial fitted with screw cap and Teflon septa, added $\text{ZrOCl}_2 \cdot 8\text{H}_2\text{O}$ (48 mg, 0.15 mmol) and 4-cyanostyrene (133 mg, 1.0 mmol). Evacuated and backfilled reaction vial with inert gas, being careful to only open up to vacuum briefly so as to not pull off 4-cyanostyrene. Sparged ethanolamine for approximately 20 minutes and then added 0.49 mL to reaction vial, black solution resulting. Placed in oil bath set at 100 °C for 6 hours. Allowed to cool to room temperature, and diluted with dichloromethane to transfer into round bottom flask. Removed excess solvent under vacuum, and then used solution of 10% ethyl acetate in hexanes to transfer to silica column. Ran flash chromatography with gradual gradient up to 40% ethyl acetate in hexanes. Yields <10%.

Synthesis of 2-(4-ethenylphenyl)-4,5-dihydro-oxazole (3) using $\text{Zn}(\text{OAc})_2$. Sparged ethanolamine under argon for approximately 20 minutes before use. In reaction vial fitted with screw cap and Teflon septa, added stir bar, $\text{Zn}(\text{OAc})_2$ (95.6 mg, 0.52 mmol), phenothiazine (300 mg, 1.5 mmol), 4-cyanostyrene (950 mg, 7.4 mmol) and 3.8 mL nBuOH to form gold yellow mixture. Sparged under argon for approximately 5 – 10 minutes. Added dropwise 0.47 mL ethanolamine, and upon completion added reaction vial to oil bath at 115 °C. Let stir for 7 hours before diluting by half in hexanes, storing in freezer overnight. Allowed to warm to room temperature, then diluted with 5 mL deionized H_2O to transfer into a separatory funnel. Extracted organic layer with 2x 10 mL washed of deionized H_2O , then extracted organic layer 5x with 5 mL dichloromethane. Ran flash chromatography (hexanes), slowly increasing polarity of column up to 15% ethyl acetate in hexanes. Removed excess solvent under vacuum, isolated 430 mg.

Synthesis of N-(tert-butyl)-O-(1-(4-(4,5-dihydrooxazol-2-yl)phenyl)ethyl)-N-(2-methyl-1-phenylpropyl)hydroxylamine (4). Prepared solution of 50/50 toluene/ethanol (EtOH). In 100 mL round bottom flask containing (3), added 20.4 mL 50/50 solution of toluene/ethanol, TIPNO (579 mg, 2.6 mmol), and a stir bar. Covered round bottom with rubber septa when not actively adding reagents. In plastic weighboat, measured Mn(salen)Cl (380 mg, 1.1 mmol), and NaBH₄ (307 mg, 8.1 mmol). Added contents of weightboat to round bottom flask, removing septa momentarily. Added slowly 0.71 mL di-tert-butyl-peroxide, removing septa to do so, and saw dark brown solution turn yellow. Replaced septa and added balloon to vent. After 3 hours, added additional portion of Mn(salen)Cl (193 mg, 0.54 mmol), NaBH₄ (152 mg, 4.0 mmol), and 0.35 mL di-tert-butyl-peroxide, exposing reaction to air momentarily. Let run an additional 18 hours overnight. Removed excess solvent under vacuum, and diluted black paste with DCM to transfer to separatory funnel. Extracted organic layer with 4x 10 mL deionized H₂O, and then 5x 20 mL DCM. Removed excess solvent under vacuum, and then dry loaded onto silica column in hexanes. Ran flash chromatography, gradually increasing the polarity to 14% ethyl acetate in hexanes. Yield: 490 mg.

Polymerization of (4).

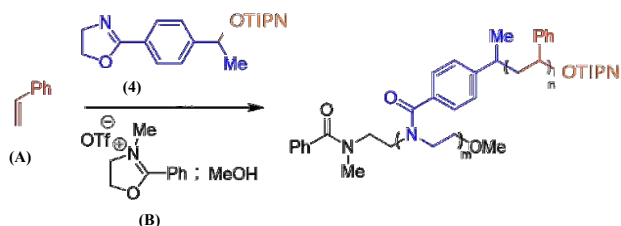


Figure 2.3: Polymerization pathway of (4)

For a general polymerization of the monomer/initiator synthesized above, the following method was used. In a scintillation vial, prepared stock solution of TIPNO (10.3 mg, 0.05 mmol) in 5 mL DCM. In another

scintillation vial fitted with septa, added stir bar, 0.47 mL of TIPNO stock solution (modify for desired equivalence), 1.9 mg B, and (4) (82.9 mg, 0.22 mmol). Removed excess DCM under vacuum, and then brought into glove box for the addition of 600 μ L styrene. Added sample to 120 °C oil bath, let stir for 150 minutes before allowing to cool to room temperature. To cooled solutions, diluted by half in DCM, and added 2-3 drops methanol to quench, can see white precipitate crashing out. A small aliquot was removed as needed from the reaction mixture for GPC analysis.

Synthesis of NMP-ROP Monomer/Initiator

For following synthetic steps, see Figure 3.5

Synthesis of 2(4-styryl)ethanoic acid (2): In a 250 mL three neck round bottom flask, added stir bar and connected to reflux condenser. Flame dried glassware under vacuum, placing septa on unused ports. Measured Mg^o turnings (4 g, 0.16 mol) and added to round bottom. Evacuate and backfill 3x with nitrogen. Under nitrogen, added 40 mL ethyl ether. Made a solution of 4-vinylbenzyl chloride (1) (20 mL, 0.14 mol) in 30 ml diethyl ether, and added first 10 mL of this solution dropwise into round bottom. Set up water lines to flow through reflux condenser, and warmed briefly with heat gun until solution dark green before submerging reaction in ice bath. Adding remaining 4-vinylbenzyl chloride solution dropwise over 30 minutes. Let reflux for 2 hours at room temperature, and then added approximately 100 g of solid dry ice by removing septa quickly and dropping in a piece at a time. Removed from ice bath while adding CO₂. Upon completion, removed septa and slowly added 25 mL of 10% HCl to quench. When stopped bubbling added an additional 25 mL, Extracted organic phase and neutralized with 300 mL saturated sodium bicarbonate solution, pH ~ 6 – 7. Extracted aqueous layer reacidified with dilute HCl (10%), can see white precipitate crash out. Filter

aqueous cuts under vacuum and isolated white powder. Dissolved in diethyl ether, and extracted organic layer. Dried over magnesium sulfate and then removed excess solvent under vacuum. Yield: 10.6 g.

Synthesis of 2-(4-vinylphenyl)hexanoic acid (3). In three-neck round bottom flask, placed stir bar and then evacuated under vacuum. Flamed dried until no more condensation could be seen, and then backfilled flask with nitrogen. Measured 2(4-styryl)ethanoic acid (5 g, 31 mmol), and added solid to flask, removing septa momentarily. Evacuated and backfilled with nitrogen 3 times before adding 100 mL dry THF. Stirred to form clear solution, and then submerged in dry ice/chloroform bath (-61 °C). Added dropwise solution of hexyllithium (22 mL, 0.17 mol) over period of 30 minutes. Replaced chloroform-dry ice bath with ice bath, and let solution stir for two hours. In a separate reaction vial fitted with Teflon septa and screw cap, degassed approximately 4 mL 1-bromo-3-chloropropane by three freeze-pump-thaw cycles, and then backfilled with nitrogen. Measured 2.7 mL of this clear solution and added dropwise to three neck flask containing brown-red solution. Upon completion removed ice bath and allowed to warm to room temperature, where pale yellow solution stirs for 18 hours. Quench reaction with 50 mL 1 N NaOH, and then transfer to separatory funnel. Extract aqueous phase and rewash organic with 25 mL 1 N NaOH. Combined aqueous cuts and reacidify with 2 N HCl. Extract organic phase with 2x 25 mL ethyl acetate, and then washed with deionized H₂O. Dry over magnesium sulfate, and then remove excess solvent under vacuum to isolate yellow oil (**3**).

Synthesis of 3-(4-vinylphenyl)tetrahydro-2H-pyran-2-one (4): To round bottom containing yellow oil (**3**), added stir bar and then evacuate and backfill round bottom with argon. Dissolved in 50 mL dry THF. In separate reaction vial, degas approximately 3 mL of DBU with three

freeze-pump-thaw cycles, before backfilling with argon. Added dropwise to round bottom containing (**3**) and placed in 60 °C oil bath for 18 hours. The resultant slurry is filtered through a glass frit and washed with 3 portions of 10 mL ethyl acetate. The filtrate's excess solvent is removed under vacuum to obtain a red-orange oil, which is diluted in a solution of ethyl acetate in hexanes before running flash chromatography (ethyl acetate: hexanes – 1:3).

Synthesis of 3-(4-(1-((tert-butyl(2-methyl-1-phenylpropyl)amino)oxy)ethyl)phenyl)tetrahydro-2H-pyran-2-one (5). The conditions for synthesizing the NMP-CROP monomer/initiator are repeated here.

Results and Discussion

ATRP Temporal Regulation Studies

The combination of ring-opening metathesis polymerization (ROMP) and atom-transfer radical polymerization (ATRP) are a well-studied tandem polymerization method.^M To assess the ability to temporally regulate the initiator species for new polymerization techniques, ATRP was first chosen for study. Poly(methyl methacrylate) was synthesized following the method above, however, the polymerization of poly(methyl methacrylate) is prone to termination events, and it was decided to move from this monomer in order to study the polymerization of methyl acrylate. A control synthesis was first designed by conducting the polymerization with lengthening reaction times, and as shown in **Figure 3.1**, it can be seen that after a reaction time of approximately 90 minutes, the conversion rates flatline around 80%, and no higher M_n were seen. This suggests that termination events are occurring as higher conversions cannot be reached, and therefore when the initiator addition experiments were conducted, the reactions were only allowed to go for 90 minutes.

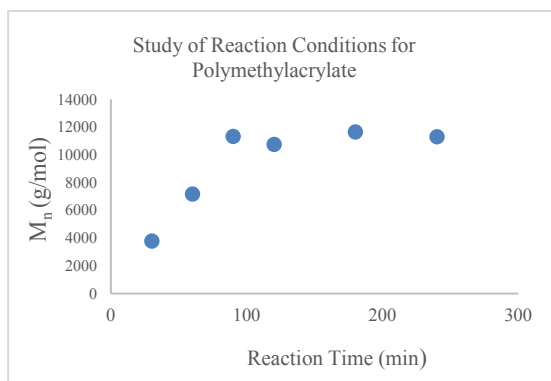
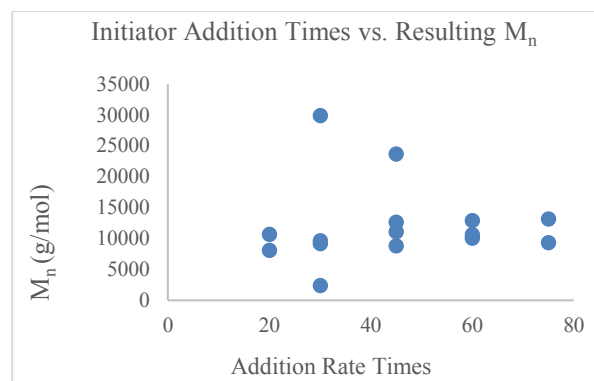


Figure 3.1: Study of Reaction Times for Synthesis of Polymethylacrylate

For the previous reactions the initiator species was added at the start of the reaction along with the other reagents. Once the length and conditions of the polymerization were chosen, the effect of adding initiator species over a period of time was studied. Keeping the total length of these reactions and the total volume of initiator added constant, the time over which the initiator was added was changed as shown in **Table 3.1**. A longer addition time will thus correspond to a slower rate, as the same volume of initiator is being added over a longer period of time. These samples were run on GPC to determine the dispersity and M_n of the samples, and NMR to determine conversion, as reported in the method above.

<u>Add't Rates (min)</u>	<u>M_n</u>	<u>\bar{D}</u>	<u>Conversion %</u>
20	10656	1.10	67
	8072	1.10	67
	9652	1.16	73
30	2374	1.29	19
	9186	1.17	71
	29905	1.15	43
45	12671	1.28	76
	23667	1.29	74
	11088	1.16	57
	8810	1.22	57
60	12896	1.54	72
	10631	1.23	56
	10056	1.48	71
75	9318	1.89	62
	13184	1.78	68

A).



B)

A) **Table 3.1:** Initiator addition times and the resulting M_n , dispersity, and Conversion % as given by GPC and NMR

B) **Figure 3.2:** Study of Decreasing Addition Rates and the Resulting M_n

From the data (**Figure 3.2**), no general trend can be seen, and this reaffirms the inconsistency of these reactions. It is believed that due to the sensitive nature for ATRP conditions, replicability of these reactions outside the glove box was difficult to master. Instead, the attention shifted to synthesizing tapered brush polymers using polymerization techniques that were shown to work with temporal regulation previously.

Synthesis of Monomer/Initiator for NMP – CROP Tandem Polymerization

First, a synthetic technique for dual functional monomer/initiators for use in tandem polymerizations must be found. Tandem polymerization techniques of nitroxide-mediated polymerization (NMP) and cationic ring opening polymerization (CROP) were chosen, as these have been previously reported, and a synthesis pathway was designed to create polyoxazoline chains serving as the polymer backbone and polystyrene chains serving as the polymer branches (**Figure 3.3**)

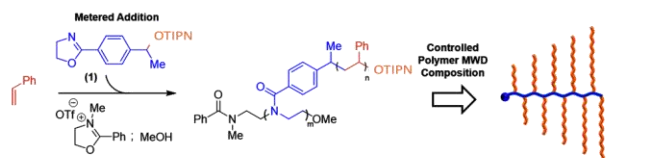


Figure 3.3: Reaction scheme of tandem polymerizations of NMP and CROP to synthesize previously inaccessible tapered brush polymers.

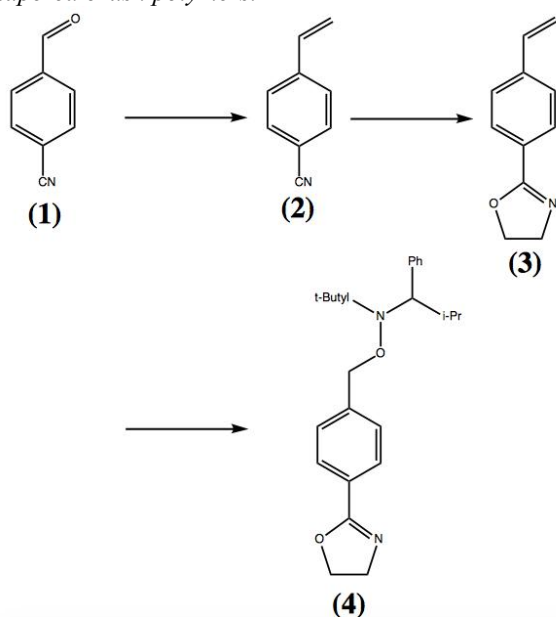


Figure 3.4: Synthesis pathway for NMP-CROP monomer/initiator

A monomer/initiator was synthesized as shown in **Figure 3.4**, beginning with the commercially available 4-cyanobenzaldehyde (**1**) and modifying a method by Zhang and Thong^o to synthesize 4-cyanostyrene (**2**). Using a similar method for the synthesis of 2-aryloxazolines^p, this product can then be treated with ethanolamine to synthesize 2-(4-ethenylphenyl)-4,5-dihydro-oxazole (**3**). This method however only resulted in <10% yields of (**3**), and thus a new synthesis involving Zn(OAc)₂ was conducted. Using this technique, 430 mg were synthesized, and it is this product that is then isolated and reacted with a TIPNO radical to create the NMP – CROP monomer/initiator (**4**). To test the polymerization of this product (**4**), a variety of reaction conditions were studied (**Table 3.2**), and for these experiments both the NMP monomer (styrene) and CROP monomer

(oxazole derivative) are added at the beginning of the reaction, although the goal is to eventually meter in the addition of the monomer/initiator species.

(1)	Radical (TIPNO)	PS. (NMP Mon.)
40	0.4 (10%)	600
40	0.8 (20%)	600
20	0.2 (10%)	300
20	0.4 (20%)	300

Table 3.2: Reaction conditions for NMP-CROP Polymerizations. Concentration of **B** (see methods), held constant at 1 eq.

Figure 3.4: GPC Chromatograms for NMP-CROP Polymerizations.

In every condition run, a bimodal distribution of peaks was seen. It is believed that this is due to one polymerization process occurring faster than the other. To test this, the reactions were let run for longer, and the second peak gave way to the first, suggesting that the extending polymer branches are growing faster than the polymer backbone monomers can click in, and the synthesized brush polymer has a random chain length along the backbone.

Synthesis of Monomer/Initiator for NMP-ROP Tandem Polymerization

As it was believed that one polymerization process was occurring faster than the other, or specifically, that the ring opening process to create the polymer backbone proceeds slower than the branching polymer process, a new tandem polymerization processes were investigated. One limit to CROP-polymerized oxazolines are that they can only be polymerized one way, and thus more flexible and speedier techniques are desired. Acid catalyzed ring opening of lactones has been

found to occur fairly quickly using coriaria valerolactones with $\text{Sc}(\text{OTf})_3$ as the catalyst.¹⁴ Additionally, the polymerization of these lactones offers the ability to use many different mechanisms for ring opening, and thus the synthesis of six-membered aryl lactones that can then be modified to serve as monomer/initiator species was studied.

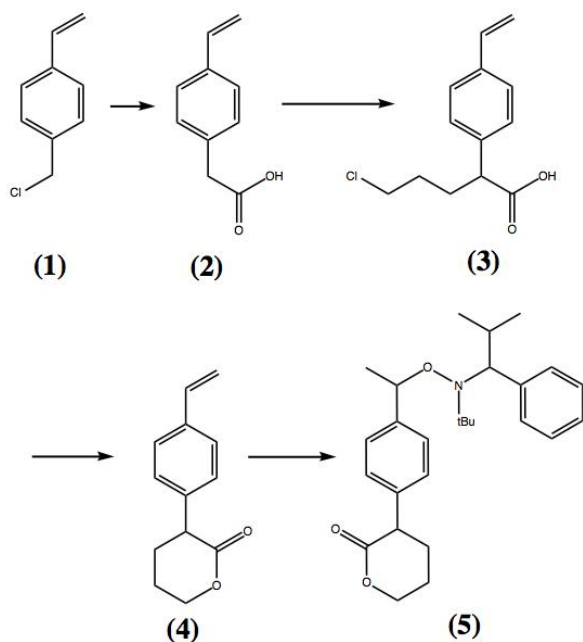


Figure 3.5: Reaction pathway for synthesis of NMP-ROP dual functional monomer/initiator

The synthesis pathway is shown in **Figure 3.5**. Modifying a technique by Rosen for the synthesis of 3-aryl- δ -lactones¹⁷, the synthesis begins with 2-(4-styryl)ethanoic acid (2), which was first synthesized from 4-vinylbenzyl chloride (1) through a Grignard reaction using a method by Padovani.¹⁵ Following the isolation of (2), the six-membered lactone (4) is synthesized in a two-step reaction pathway, where first (2) is treated with hexyllithium and 1-bromo-chloropropane, followed by treatment with DBU. The isolated lactone can then be treated with the NMP TIPNO radical to create the NMP-ROP monomer/initiator. Currently work is ongoing to polymerize this structure.

Conclusion and Future Work

The first look at ATRP temporal regulation deemed ATRP unsuitable for these reactions and no further modification of synthesis pathways was investigated. Instead, the synthesis of a new monomer/initiator for NMP-CROP polymerization was developed, and investigation began into various polymerization techniques using this structure. It was found that the synthesized structure utilized an oxazoline-derivative as the cationic ring opening for the backbone, and that this process was neither fast or versatile enough for the desired range of monomer synthesis. Thus, other monomers were investigated that might provide more possibilities for ring opening to create a faster backbone polymerization, and a six-membered lactone species was synthesized to create a possible NMP-ROP monomer/initiator. The synthesis of these dual-functional monomer/initiators will allow for the investigation of new polymer shape development. Future work will include the continued synthesis of these brush polymers with narrow distributions, and then the metered addition of these monomer/initiators to see how the molecular weight shapes can be manipulated to form tapered polymer compositions.

Acknowledgements

This study was supported by Cornell University and the Cornell Center for Materials Research with partial funding from the Research Experience for Undergraduates program (DMR-1460428) This study made use of the Cornell Center for Materials Research Shared Facilities, which are supported through the NSF MRSEC program (DMR-1120296).

References

1. Ayres, N. *Polymer Chemistry*, **2010**, *1*, 769 – 777.
2. Baltork, I.; Khosropour, A.; Hojati, S. *Cat. Comm.* **2007**, *8*, 200 – 204.
3. Bielawski, C. W.; Louie, J.; Grubbs, R. H. *J. Am. Chem. Soc.* **2000**, *122*, 12872.
4. Biewlawski, C.W.; Morita, T.; Grubbs, R. H. *Macromolecules*. **2000**, *33*, 678 – 680.
5. Cheng, C.; Khoshdel, E.; Wooley, K. L. *Nano Lett.* **2006**, *6*, 1741.
6. Gentekos, D. T.; Dupuis, L. N.; Fors, B. P. *J. Am. Chem. Soc.* **2016**, *138*, 1848 – 1851.
7. Hadziioannou, G.; Skoulios, A. *Macromolecules*, **1982**, *15*, 287 – 271.
8. Idage, B.B.; Idage, S.B., et al. *Elsevier: Materials Science and Eng. B.* **2010**, *168*, 193 – 198.
9. Kottisch, V.; Gentekos, D. T.; Fors, B.P. *ACS MacroLetters*. Submitted for publication.
10. Lynd, N. A.; Meuler, A. J.; Hillmyer, M. A. *Elsevier: Progress in Polymer Science.* **2008**, *33*, 875 – 893.
11. Lynd, N. A.; Hillmyer, M. A.; Matsen, M. W. *Macromolecules*. **2008**, *41*, 4531 – 4533.
12. Matyjaszewski, K. *Macromolecules*, **2012**, *45*, 4015 – 4039.
13. Nichetti, D.; Manas-Zioczower, I. *Polym. Eng. Sci.* **1999**, *39*, 887 – 895.
14. Nomura, N.; Taira, A.; Tomioka, T.; Okada, M. *Macromolecules*. **2000**, *33*, 1497 – 1499.
15. Padovani, M.; Hillker, I.; Duxbury, C.J.; Heise, A. *Macromolecules*, **2008**, *41*, 2439 – 2444.
16. Plate, N. A., Shibaev, V. P. *J. Poly. Sci.: Macromol. Rev.* **1974**, *8*, 117.
17. Rosen, J.; Nelson, T. D.; Huffman, M.A.; McNamara, J. M. *Tet. Let.* **2003**, *44*, 365 – 368.
18. Shipp, D. A. *Polymer Reviews*, **2011**, *51*, 99 – 103.
19. Zhang, J.; Tang, T. *Adv. Synth. Catal.* **2016**, *358*, 752 – 764.

Tumor cell shed microvesicles modulate endothelial monolayer permeability

Carlisle DeJulius¹, Francois Bordeleau¹, Marc Antonyak², Cynthia Reinhart-King¹

1. Nancy E. and Peter C. Meinig School of Biomedical Engineering, Cornell University, Ithaca, NY 14853, United States
2. Department of Biomedical Sciences, Cornell University, Ithaca, NY 14853, United States

Abstract

An important part of cancer progression is the diseased cells' ability to influence non-malignant cells. One method of communication is the shedding of microvesicles (MVs), membrane-bound vesicles whose cargo has been shown to modify cell behavior. Moreover, the vasculature present in the tumor is leakier than that found in healthy tissue. In addition, vascular permeability is known to be modulated by the increased stiffness of the tumor microenvironment. Here, we have treated endothelial cell monolayers seeded on substrate with stiffness ranging from 175 Pa to 10 kPa with MVs released by carcinoma cells. Our results show that tumor cell shed MVs increase endothelial cell monolayer permeability, notably by disrupting actin and cell-cell junction organization. Overall, our results suggest that MVs can contribute to tumor vasculature leakiness.

1. Introduction

Cancer remains a problem in the United States, with approximately 171 people per 100,000 dying from this disease annually (NCI). The vasculature plays an important role during cancer progression. The tumor vasculature is much leakier than in healthy tissues, which in turn affects drug delivery. In addition, vascular permeability has been shown to influence both tumor cell intra- and extravasation (Azzi, et al. 2013). Therefore, the mechanism controlling vasculature leakiness has important therapeutic consequences.

One mechanism by which cells communicate is the release of microvesicles (MVs). MVs are membrane-bound vesicles containing specific molecules including proteins, RNA transcripts, and DNA (Desrochers et al., 2016). The cargo can be taken up by neighboring or distant cells through endocytosis and influence the behavior of these cells. MVs shed by cancer cells have been shown to stimulate increased cell growth, survival, and migration (Desrochers et al., 2016). In this way, MVs allow tumor cells to influence their immediate environment as well as more remote cells. Tumor progression can

increase the stiffness of the extracellular matrix (ECM) (Levental et al. 2009). Interestingly, we have previously shown that increased ECM stiffness leads to increased endothelium permeability (Huynh et al., 2011). We have also shown that MV treatment increases the contractility of epithelial cells (Bordeleau et al., 2015). A similar response in endothelial cells could lead to increased vascular leakiness. The chemical cues provided by MVs and the physical cues provided by ECM stiffness may synergize to promote the leaky phenotype characteristic of tumor blood vessels.

In this work, we investigated the effect of MVs on the permeability of human umbilical vein endothelial cell (HUVEC) monolayers. HUVEC were cultured on either collagen gels of two stiffness values or polyacrylamide (PA) gels of two stiffness values. After MV treatment, the permeability of the monolayer was assessed. Additionally, cells were fixed and stained to observe cytoskeletal protein organization and cell-cell junction width. We hypothesized that permeability would increase with MV treatment and stiffness.

2. Methods

2.1 Cell culture and reagents

HUVEC were maintained in Endothelial Growth Medium (EGM) (Lonza, Allendale, NJ). MDA-MB-231 cells were maintained in RPMI-1640 medium (Sigma) supplemented with 5% fetal bovine serum

Commented [FB2]: MVs and increased cell contractility

Commented [D1]: Found this stat on National Cancer Institute website. Useable or no?

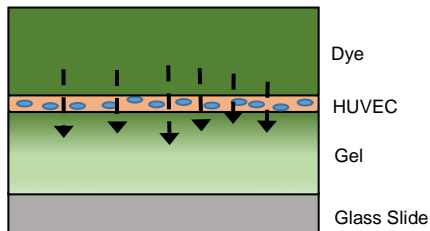
(FBS). All cells were cultured at 37°C and 5% CO₂. The primary antibody used was goat anti-VE-cadherin (#J1315; Santa Cruz Biotechnology, Santa Cruz, CA, USA). The secondary antibody used was Alexa-568 donkey anti-goat IgG (Invitrogen, Carlsbad, CA). Phalloidin-Alexa Fluor 488 and phosphate buffered saline (PBS) were purchased from Invitrogen; Triton X-100 was purchased from JT Baker (Philipsburg, NJ, USA). Acrylamide, bis-acrylamide, TEMED, and Ammonium Persulfate (APS) were purchased from Bio-Rad (Hercules, CA, USA). All other reagents were purchased from Sigma-Aldrich (St. Louis, MO, USA).

2.2 MV Collection and treatment of cells

MDA-MB-231 cells were cultured to ~80% confluency, rinsed twice with PBS, and incubated in serum-free RPMI medium for between 8 and 18 hours. The conditioned media was collected and spun twice at 400 rpm to collect debris. The solution was then filtered using a 0.22 µm Steriflip filter unit (Millipore) to collect MVs. The filter was rinsed with 10 mL of serum-free RPMI and filtered until 1 mL remained. The MV solution was collected from the filter for use. HUVEC monolayers on PA and collagen gels were treated with 500 and 30 µL of MVs, respectively, and incubated at 37°C and 5% CO₂ for 5.5 hours before assays were performed.

2.5.3 Confocal permeability time-lapse imaging on collagen gels

The supernatant media of the collagen gels was replaced with 100 µL of 10 µM FITC-dextran in EGM. Using a Zeiss LSM700 inverted laser scanning confocal microscope with a LD Plan-Neofluar 20x/0.4 Korr objective, the top of the gel was located. A 600 µm z-slice was taken to encompass the dye solution above the gel and that had diffused inside (see Figure 1). A 15-minute time-lapse was taken, with acquisitions made every 30 seconds.



2.3 Polyacrylamide gel synthesis

18x18 mm glass coverslips were activated with 0.1% glutaraldehyde. Gel solutions were prepared by combining 40% acrylamide, 2% bis-acrylamide, 0.25 M HEPES, TEMED, and MilliQ water. The stiffness of the gels was tuned by altering the ratio of acrylamide to bis-acrylamide. 1 kPa and 10 kPa gels were used. Polymerization was initiated with 10% ammonium persulfate, and the gel solution was sandwiched between the activated coverslip and a Rain-X treated 18mm diameter circular top coverslip. When polymerization was complete, the top coverslip was removed and the gels were coated in collagen. Before cell seeding, the gels were sterilized with UV light for 1 hour. HUVEC were seeded at 250,000 cells/gel and cultured for 5 days to confluency.

2.4 Collagen gel glycation and polymerization

Collagen stock solutions at 10mg ml⁻¹ were mixed with 500mM ribose to yield solutions with a final ribose concentration of 0 or 100mM in 0.1% sterile acetic acid. The solutions were incubated at 4°C for 5 days. After the glycation period, HEPES, EGM, and 1 M sodium hydroxide (neutralizing) were added. The 1.5 mg ml⁻¹ collagen solution was polymerized at 37°C for 1 hour, and the gels were washed with EGM

Figure 1: Cartoon of permeability assay. Dye is added to the supernatant media diffuses through the cell monolayer over time. The cells are seeded on either a PA or collagen gel, which absorbs the dye after it passes through the monolayer.

2.5.4 Staining and Fluorescence Imaging

HUVEC monolayers were fixed with 3.7% (v/v) formaldehyde in PBS on PA gels. The cells were permeabilized with 1% (v/v) Triton in PBS and the sample was blocked for non-specific binding with 5% fetal bovine serum (FBS) in PBS. Cells were incubated with goat anti-VE-cadherin primary antibody in PBS, then incubated with Alexa-568 donkey anti-goat secondary antibody and Alexa Fluor 488 phalloidin in PBS to stain for VE-cadherin and actin, respectively. The cells were also washed with DAPI in PBS to stain DNA. A Zeiss LSM700 inverted laser scanning confocal microscope with a EC Plan-Neofluar 20x/0.5 Pol objective was used to visualize the stained samples.

to remove traces of ribose. HUVEC were seeded at 25,000 cells/gel and cultured for 2 days to confluency.

2.5 Imaging

2.5.1 Confocal reflectance collagen imaging

A Zeiss LSM700 inverted laser scanning confocal microscope (Carl Zeiss, Oberkochen, Germany) was used to visualize the internal architecture of collagen gels. Optical slices were collected with a long working distance water-immersion CApochromat 40x/1.1 NA objective (Carl Zeiss).

2.5.2 Confocal permeability imaging on PA gels

The PA gels were transferred to 50 mm glass-bottomed Mattek dishes filled with a 10 µM FITC-dextran solution in EGM. Using a Zeiss LSM700 inverted laser scanning confocal microscope with a long working distance water-immersion CApochromat 40x/1.1 NA objective, the top of the gel was located. A 300 µm z-slice was taken to encompass the dye solution above the gel, the dye that had diffused inside, and the glass slide. Figure 1 is a cartoon of this system. After 5 minutes of diffusion, 6-8 images were taken at different positions on the gel.

2.6 Image Analysis

2.6.1 PA gel permeability

ImageJ software was used to evaluate the permeability of the PA gel samples. The mean gray value (MGV) of the dye that had diffused inside the gel was normalized to the MGV of the dye above. The normalized intensity value was averaged for the 6-8 images taken to yield one value per sample.

2.6.2 Collagen gel permeability

Using the Registration feature in ImageJ, the time-lapse stacks were normalized to each other to correct for drift in the system. The initial MGV of the dye above the gel was measured, and the MGV of each time point was normalized to it. The values were plotted against the square root of time to yield a linear curve. The slope of this curve was used to represent diffusion.

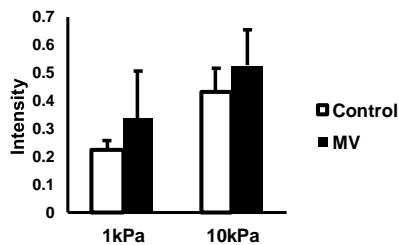


Figure 2. MVs and stiffness cause increasing permeability trend in endothelial cell monolayers on PA gels. Data presented as mean \pm SEM.

3. Results

3.1 MVs modulate endothelial cell permeability as a function of ECM stiffness

We have previously shown that PA gels of increasing stiffness can increase endothelial permeability (Huynh et al., 2011). Therefore, we investigated whether this phenomenon would be further enhanced with MV treatment. After treatment, the permeability of HUVEC monolayers was measured as described above. Figure 2 shows a slight

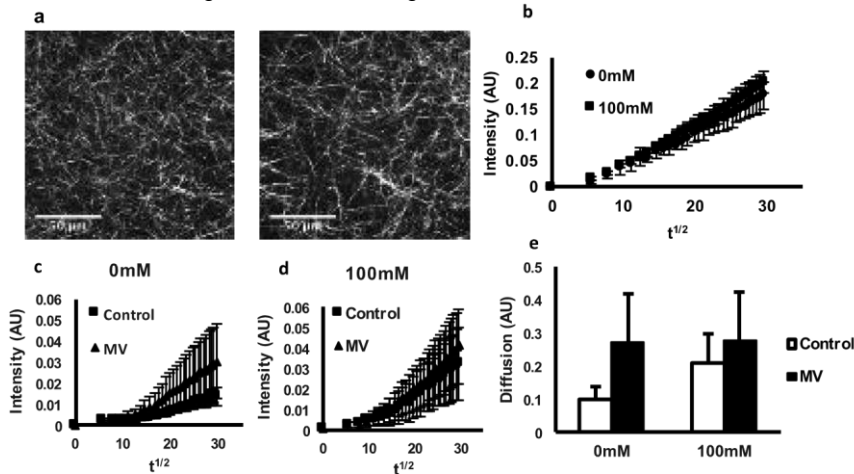


Figure 3. MV treatment increases endothelial cell permeability. (a) Collagen gel internal structure as determined by confocal reflectance microscopy. (b) Permeability of cell-free collagen gels that were incubated with either 0mM or 100mM ribose. (c) Permeability of endothelial monolayers cultured on collagen gels incubated with 0mM ribose, with or without MVs. (d) Permeability of endothelial monolayers cultured on collagen gels incubated with 100mM ribose, with or without MVs. (e) Mean slope of the diffusion curve for HUVEC monolayers cultured on either 0mM or 100mM ribose collagen gels, with or without MVs. Data presented as mean \pm SEM.

increase in permeability with MV treatment on both soft and stiff gels. Increasing stiffness also increased permeability, agreeing with previous results.

In order to measure vascular permeability at lower stiffness levels, we extended our study to the permeability of endothelial monolayers on collagen gels. Previous work has shown these gels to have compressive moduli between 100-800 Pa, respectively (Mason et al., 2012). This value is much closer to the stiffness found in healthy tissue, so we were interested to see if MVs had the same effect that was shown on stiffer PA gels. Figure 3a

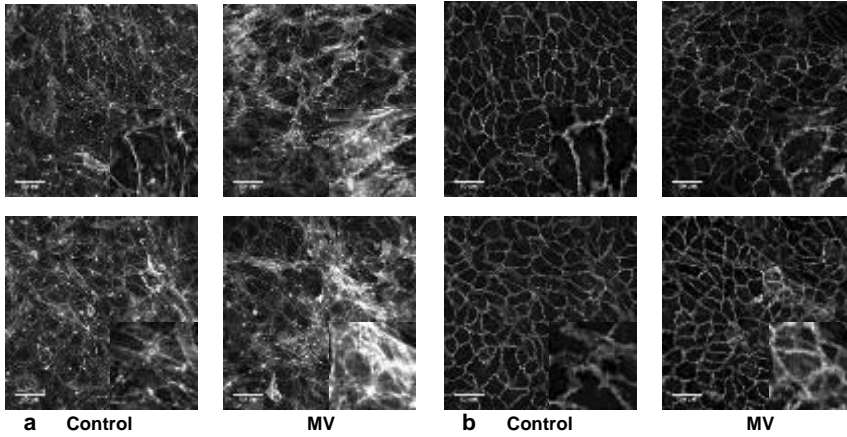
shows the architecture of an unglycated sample and a sample treated with 100mM ribose solution. There is no significant difference in the internal architecture of the two gels (Mason, et al. 2012). The permeability of unglycated and glycated acellular collagen gels is not significantly different, reflecting the structural similarities (Figure 3b). Figure 3c and d show the diffusion curves for endothelial monolayers

on the gels. Figure 3e displays the slopes of these graphs, representing permeability. Again, there appears to be an increase in permeability with MV treatment. Of note, the increase is most robust on the 0mM collagen gels. Together, our results show that MV treatment increases permeability, and that MVs have a greater effect on endothelial cells seeded on ECM with stiffness values similar to those of healthy tissue.

3.3 MVs influence actin and ve-cadherin organization

In order to understand the physiological mechanisms behind the increased permeability seen in both systems,

we decided to investigate actin organization and cell-cell junction width. Figure 4a shows that on the 1kPa and 10 kPa PA gels, the



1kPa

10kPa

Figure 4. MVs affects endothelial cells actin and cadherin organization. (a) Confocal images showing actin fiber organization of endothelial cell monolayers seeded on either 1 kPa and 10kPa PA gels and treated with or without MV. (b) Confocal images showing cell-cell phenomenon is seen on 10kPa gels. The cell-cell junctions appear more disrupted and wider with MV treatment when compared to the control on both stiffnesses (Figure 4b).

endothelial cells displayed an increase in the density of actin fibers, with patches that were much more compact than others. In contrast, the control group exhibited a more even distribution of actin. The same

4. Discussion

The tumor vasculature is characterized by increased leakiness (Azzi et al. 2013), which in turn influence drug delivery and tumor cell intravasation (Harney et al. 2015). Here, we show that MVs

can increase vascular permeability. We show that the increased permeability trend might be stronger on more compliant ECM with stiffness more characteristic of normal tissue. Moreover, we show that the MV treatment alters the actin cytoskeleton and disrupts the cell-cell junctions. Overall, our results indicate that MVs may play a role in increasing vascular leakiness.

Vascular permeability is known to be directly proportional to the contractility of the endothelial cells lining the blood vessel l junctions present in endothelial monolayers on 1

generation in epithelial cells (Bordeleau et al., 2015). Our finding indicating a MV-mediated disruption of the ve-cadherin junction and increased actin fiber content, which are both characteristic of increased cell contractility. Therefore, a MVmediated contractility response in endothelial cells, similar to the one seen in epithelial cells, could explain our results. Higher contractility could lead to higher stress across cell-cell junctions, which in turn could allow more molecules to diffuse between the cells. MVs could be important in enhancing this effect in tumor blood vessels, as well as instigating it in distant tissues.

(Huynh et al. 2011). Interestingly, it has been shown that MVs can cause increased traction force important role in of cancer progression Understanding the complex interactions between ECM stiffness and MV cargo will be important in combatting tumor progression, especially for drug delivery and preventing intravasation.

Acknowledgements

This work was supported by the Cornell Center for Materials Research (CCMR) Research Experience for Undergraduates (REU) program through the NSF (DMR-1460428 and DMR-1120296). We would also like to acknowledge the contributions of Richard Cerione.

Reference

- Azzi, S. et al. Vascular permeability and drug delivery in cancers. *Frontiers in Oncology* (2013).
- Bordeleau, F., et al., Microvesicles released from tumor cells disrupt epithelial cell morphology and contractility. *Journal of Biomechanics* (2015).

Desrochers, L., et al. Extracellular Vesicles: Satellites of Information Transfer in Cancer and Stem Cell Biology. *Developmental Cell* (2016).

Harney, A., et al. Real-Time Imaging Reveals Local, Transient Vascular Permeability, and Tumor Cell Intravasation Stimulated by TIE2^{hi} Macrophage-Derived VEGFA. *Cancer Discovery* (2015).

Huynh, et al. Age-Related Intimal Stiffening Enhances Endothelial Permeability and Leukocyte Transmigration. *Cell Biomechanics* (2011).

Levental, K., et al. Matrix Crosslinking Forces Tumor Progression by Enhancing

(Desrochers et al., 2016). The mechanisms of their action, however, are still poorly understood. Here, we investigated the possible effects of MVs on endothelial cell permeability, and found increased permeability with treatment. In the future, we hope to further investigate the underlying mechanism by which MVs disrupt endothelial actin and VE-cadherin organization.

Commented [FB3]: Leakiness or permeability

Commented [FB4]: Link stiffness, mvs and potential physiological importance

It is accepted that MVs play an important role in of cancer progression
Integrin Signaling. *Cell* (2009).

Mason, et al. Tuning three-dimensional collagen matrix stiffness independently of collagen concentration modulates endothelial cell behavior. *Acta Biomaterialia* (2013).

National Cancer Institute (NCI).
<http://www.cancer.gov/aboutcancer/understanding/statistics>

Exploring actin filaments and the effect of ROCK in gemcitabine resistant pancreatic cancer cells

Ricem Díaz¹, Ian Cardle², Fredrik Thege³, Kyle Wellmerling⁴, Brian Kirby⁴, Ankur Singh⁴

¹ CCMR ² Bioengineering Department ³ Biomedical Engineering Department ⁴ Engineering Department

Abstract

Pancreatic cancer is the fourth leading cause of cancer-related deaths in US¹, with an overall 5-year survival rate of less than 5%.^{1,2,3} Due to the lack of effective screening and biomarkers, the mechanisms of pancreatic cancer remain unclear. Actin is the major component of the cytoskeleton, which is involved in morphology, motility and division of the cell. ROCK, a Rho-associated coiled-coil containing protein kinase, plays a role in actin filaments in different ways. In this study, the role of actin filaments and the effect of ROCK inhibitor in resistant pancreatic cancer cells were explored. A difference in actin filaments was observed with fluorescence microscope as the resistance to the drug increased. The MTT Assay concluded that the ROCK inhibitor makes the pancreatic cancer cells more resistant to the drug. These outcomes provide the possibility that actin filaments are involved in drug resistance of pancreatic cancer.

Introduction

Pancreatic cancer is the 4th leading cause of cancer-related deaths in US¹, with an overall 5-years survival rate of less than 5%.^{1,2,3} Most pancreatic cancer has already reached an advanced stage when the first symptoms appear. Due to lack of effective screening and biomarkers, the mechanism of pancreatic cancer remains unclear. The standard treatment for patients with advanced pancreatic cancer is chemotherapy.⁴ Gemcitabine has been the standard of treatment during the last decade, but the median survival of patients treated with gemcitabine is only 5-6 months.⁴ Therefore, an understanding of the mechanism of pancreatic cancer may advance the treatment for pancreatic cancer.

One of the key challenges in cancer research is to develop predictive models of human tumors for identification of therapeutic targets and drug testing.⁵ Simple culture formats, such as spheroids, cancer cells in scaffolds and small cancer organoids are being complemented by bioengineered tumors providing cancer cells with tissue context incorporating the extracellular matrix, stromal cells and physical signals.^{6,7,8} Biomimetic models of human tumors, generated using methods of tissue engineering, provide a tremendous progress in understanding the native milieu of human tumors.⁵ Studying the biological complexity of tumor is necessary to build bioengineered tumor models that predict the cancer pathways and biomarkers.

Rho GTPases are small proteins that act as molecular switches in a wide range of signaling pathways.⁵ Three main classes of Rho GTPases; Rho, Rac and Cdc42, are known to regulate actin cytoskeletal dynamics.¹⁰ Rho-associated coiled-coil containing protein kinase (Rho-

kinase/ROCK) was initially characterized for its role in mediating the formation of RhoA, which induces stress fibers and focal adhesion through its effects on the phosphorylation of the myosin light chain.¹¹ ROCK also phosphorylate LIM kinase 1 and 2 (LIMKs), which phosphorylate cofilin.¹⁰ The phosphorylation of cofilin by LIMKs inactivates its actin depolymerization activity (Figure 1).¹² Therefore, the phosphorylation of LIMKs by ROCK inhibits cofilin-mediated actin-filaments disassembly and leads to an increase in the number of actin filaments.¹⁰ It has been reported that the Rho-ROCK pathway plays an important role in various cellular functions such as vascular smooth muscle cell contraction, cell migration and cell proliferation.¹³

Cell migration involves multiple processes that are regulated by various signaling molecules.¹⁴ The actin cytoskeleton and its regulatory proteins are crucial for cell migration in most cells.¹⁵ During cell migration, the actin cytoskeleton is dynamically remodeled, and its reorganization produces the force necessary for cell migration.¹⁶ Dynamics rearrangements in the actin cytoskeleton during progression of the disease are common to all forms of cancer.¹ It has been reported that actin remodeled in resistant and sensitive cells of ovarian and breast cancer cells.^{17,18} Because inhibition of these processes decreases cell motility, elucidation of the molecular mechanism of actin reorganization is important for cancer therapeutics.¹⁵ In Kirby's lab, subclones of gemcitabine resistant cell lines are generated. This subclones with more resistance aid to find the connection between proteins involves in cell motility and how this affect drug resistant. In the present study, we investigated the role of actin and effect of ROCK in resistant pancreatic cancer cells.

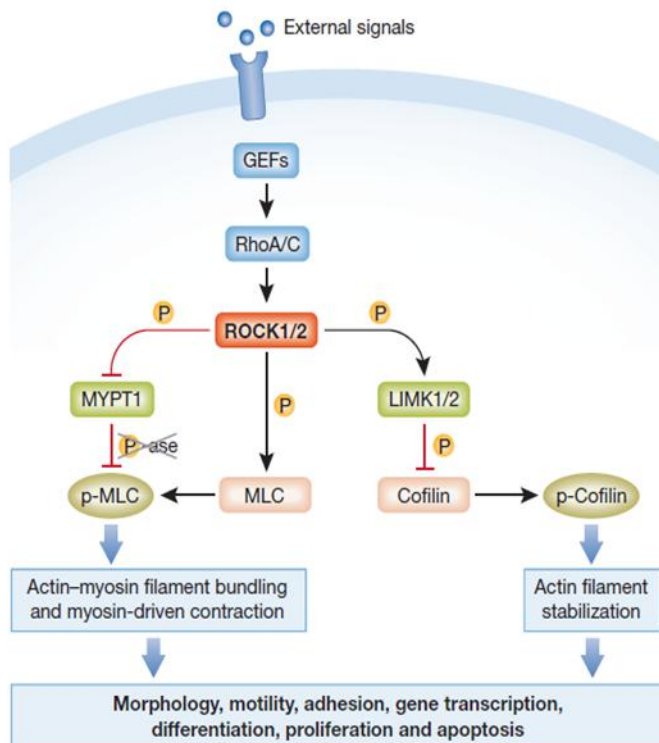


Fig 1: Rho/ROCK signaling promotes actomyosin contractility.⁴ RhoA/C are activated by guanine exchange factors (GEFs) that translate external signals from activated membrane receptors into cellular responses.⁴ Activated Rho proteins bind to and activate ROCK1 and ROCK2, which phosphorylate target proteins such as MYPT1, MLC and LIMK1/2. ROCK-mediated phosphorylation of MLC and LIMK-mediated phosphorylation of cofilin promotes increased actin fibre bundling and actomyosin contraction, which directly or indirectly influence various cellular behaviours.⁴ LIMK1/2, LIN-11, Is11 and MEC-3 domain kinase 1/2; MLC, myosin light chain; MYPT1, myosin binding subunit of the MLC phosphatase; ROCK1/2, Rho-associated coiled-coil protein kinase 1/2.⁴

Methods

Cell Culture

PANC-1, BxPC3, BxGR80C, BxGR360C, PAGR Col1 and Col10 pancreatic cancer cells were grown and generated in Kirby's Lab. The medium was supplemented with RPM1, 10%FBS and 1x P/S in humidified 5% CO₂ incubator at 37 °C.

Immunofluorescence microscopy studies

The cells were grown in 96-well plates, aspirated off all media and wash once with 200µL of PBS. It was added 200 µL of fixative (2% PFA in PHEM buffer) to each well and incubated for 15 minutes at RT. It was removed solution and washed three times with 200 µL PBS. Then it was added 200 µL of blocking buffer (10% NDS in PBS) per well and incubated for 45 minutes at RT. During this time, it was prepared primary antibody dilution: antibodies were spined down at 2000 RCF for 30 seconds and diluted together in blocking buffer. The blocking buffer was removed and preceded without washing. It was added 200 µL of permeabilizing buffer (0.1% saponin in PBS) and incubated for 5 minutes at RT. The solution removed and washed three times with PBS. Then it was added 100 µL of primary antibody and incubated for 1 hour. The secondary antibodies were prepared together in the same manner as primaries, except with the dilution listed next. The solution was removed and washed three times with PBS. It was added 100 µL of secondary antibody to each well, covered and incubated for 1 hour at RT. The solution was removed and washed three times with PBS. It was added 100 uL of DAPI solution per well and incubated covered for 15m at RT. And solution was removed and washed three times with PBS. Last wash stay in wells. The samples were performed fluorescence microscopy using the appropriate filters and following exposure times: DAPI: 10ms; Gain: 1 and TRITC: 500ms; Gain: 2.

Image Analysis

Based on the intensity of phalloidin signal on the fluorescence microscopy images, actin was quantitatively compared in the cell lines by CellProfiler. Using Student t test, the results were compared statistically to look for significantly difference within the cell lines.

MTT Cytotoxic Assay

The cells were plated in T25 flasks/60mm petri dish at 500,000 cells/flask. Then, the cells were plated on flat-bottom 96-well plates at 5,000 cells/well with 200 μ l complete media. To avoid evaporation, the edges were filled with media. After 24 hours, the cells were treated with gemcitabine and ROCK Inhibitor, Y27632. It was added 150ul media containing a range of gemcitabine concentrations. This involved an 8-point serial dilution starting at 100uM with a dilution factor of 1:4. Include two untreated controls, one without Gemcitabine and other without Gemcitabine and Rock, and two blanks (just media) to normalize each of these values. It was added 30uM of Y27632 Rock Inhibitor 10mM suspended in 50uL of PBS to each well. The cells were incubated with gemcitabine and Rock Inhibitor for 5 days. Make a 5 mg/mL (10x) solution of MTT in PBS. Vortex and place on rocker or 37C water bath until crystals (almost) completely dissolve (~30mins). Solution will be yellow. The solution was filtered with a 0.2um syringe filter. Then this solution was added to the cell supernatant with a multi-pipet, and pipetted up and down to mix. This was repeated for every row. It was incubated for 4 hrs in the 37C incubator. After 4 hours, the plates were centrifuged for 5 minutes at 1000xg. The MTT/media solution was removed carefully from the cells, leaving just formazan crystals. It was added 200 uL of acidified IPA (50mM HCl, 0.1% Triton X in Isopropyl Alcohol) to each well. Then, it was incubated on orbital shaker at 37°C for at least 15 minutes. Finally, the absorbance was read in the plate reader at 560 nm and a reference at 690 nm. The IC50 value was determined by finding where the viability curve crosses 50% of control well viability.

Results and Discussion

Effects of actin in resistant pancreatic cancer cells

In order to examine whether or not actin was involved in pancreatic cancer cells proliferation, we first evaluated the fluorescence microscopy images. The cells were stained with phalloidin, which bind to actin. The brightness was lower in the cell lines with more resistance (View Appendix). To verify these results, we also quantify the intensity of the phalloidin signal by CellProfiler. The intensity was increased in cell lines with more resistance. (View Appendix) Taken together, these results indicate that actin plays a role in the resistance of pancreatic cancer proliferation.

Effects of ROCK in resistant pancreatic cancer cells

We next examined the effect of ROCK inhibitor on the apoptosis of PANC-1, PAGR Col1 and Col10 pancreatic cancer cells. The cells were treated with gemcitabine within the range from 0-100 μ M and constant Y27632 30 μ M for 5 days. After treatment, the resistant pancreatic cancer cells were more resistant to the drug. The IC50 was higher in resistant cells with Y27632 than without this inhibition (View Appendix). Gathering these results, it can indicate that ROCK doesn't help to recover sensitive in resistant pancreatic cancer cells.

Our findings reveal that pancreatic cancer cells differing in drug sensitivity to gemcitabine show varied in the fluorescence intensity of actin cytoskeleton. We show an up-regulation of actin cytoskeleton in pancreatic cancer cells with more resistance. We also show that ROCK doesn't

change sensitive in pancreatic cancer cells. These outcomes could be due to remodeling of actin cytoskeleton by a signaling pathway that doesn't required ROCK activity.

Conclusions

The intensity of actin expression in resistant pancreatic cancer cell lines has change. On the other hand, ROCK inhibition doesn't change sensitive in these cells. For future works, it will be important to measure the stiffness in hydrogels with resistant pancreatic cancer cells to study the mechanical properties at different level of actin.

Acknowledgments

This work was supported by the Cornell Center for Materials Research with funding from the NSF MRSEC program (DMR-1120296).

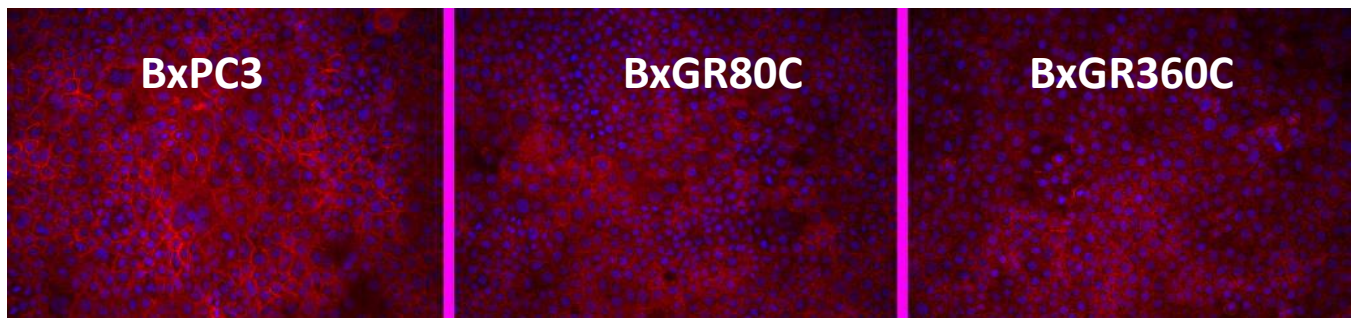
References

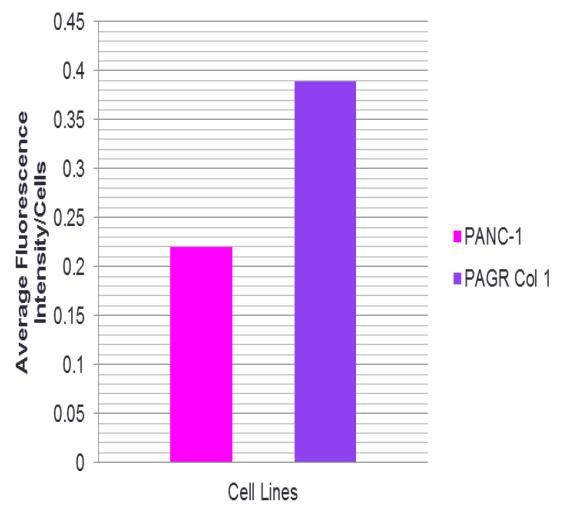
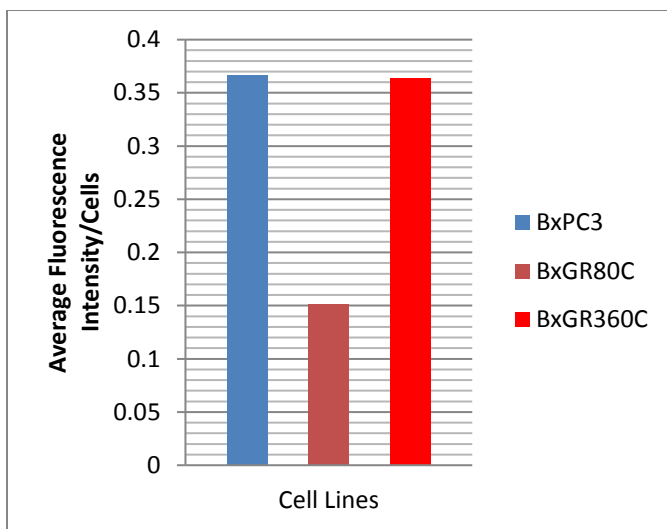
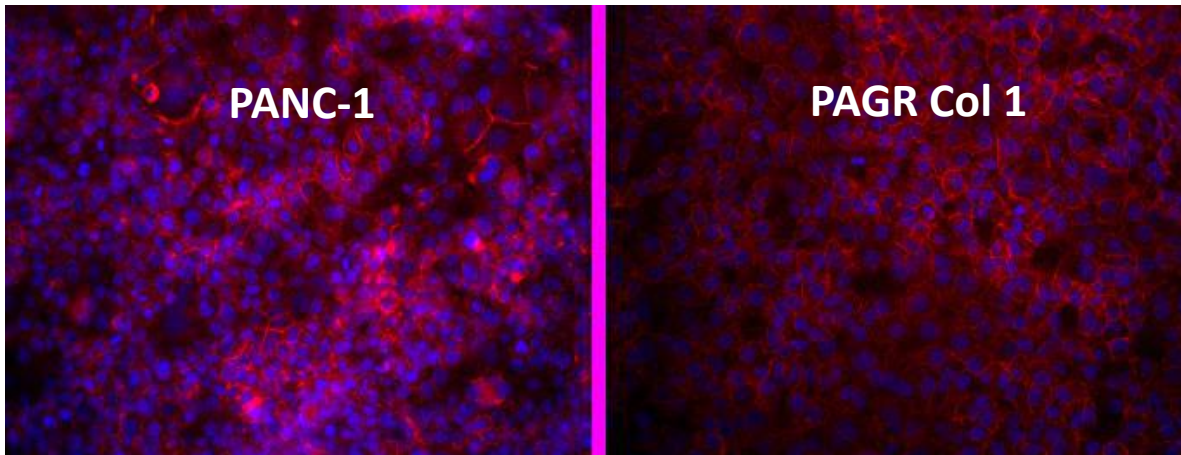
- ¹ Suresh, S. (2007) Biomechanics and biophysics of cancer cells. *Acta Materialia*, 55, 3989-4014.
- ² Bursac, P., et al. (2005) Cytoskeletal remodelling and slow dynamics in the living cell. *Nat Mater*, 4, 557–61.
- ³ Cokelet, G.R., et al. (1968) Rheological comparison of hemoglobin solutions and erythrocyte suspensions. *Science*, 7, 162-275.
- ⁴ Nakashima, M. (2011) Inhibition of Rho-associated coiled-coil containing protein kinase enhances the activation of epidermal growth factor receptor in pancreatic cancer cells. *Molecular Cancer*, 10(79). doi: 10.1186/1476-4598-10-79
- ⁵ Villasante, A. (2015) Tissue-engineered models of human tumors for cancer research. *Expert Opin Drug Discov*, 10(3), 257-68.
- ⁶ Kimlin, C., et al. (2013) In vitro three-dimensional (3D) models in cancer research: an update. *Mol Carcinog*, 52(3),167–82.
- ⁷ Yamada, K.M., Cukierman, E. (2007) Modeling tissue morphogenesis and cancer in 3D. *Cell*, 130(4), 601–10.
- ⁸ Nyga, A., et al. (2011) 3D tumour models: novel in vitro approaches to cancer studies. *J Cell Commun Signal*, 5(3), 239–48.
- ⁹ Ellenbroek, S. I., Collard, J. G. (2007) Rho GTPases: functions and association with cancer. *Clin Exp Metastasis*, 24, 657-72.

- ¹⁰ Riento, K., Ridley, A. J. (2003) Rocks: multifunctional kinases in cell behavior. *Nat Rev Mol Cell Biol*, 4, 446-56.
- ¹¹ Amano, M., et al. (1996) Phosphorylation and activation of myosin by Rho-associated kinase (Rho-kinase). *J Biol Chem*, 271, 20246-49.
- ¹² Arber, S., et al. (1998) Regulation of actin dynamics through phosphorylation of cofilin by LIM-kinase. *Nature*, 393, 805-9.
- ¹³ Sahai, E., Marshall, C. J. (2002) RHO-GTPases and cancer. *Nat Rev Cancer*, 2, 133-42.
- ¹⁴ Ridley, A. J., et al. (2003) Cell migration integrating signals from front to back. *Science*, 302, 1704-9.
- ¹⁵ Yamazaki, D., et al. (2005) Regulation of cancer cell motility through actin reorganization. *Cancer Sci*, 96(7), 379-86.
- ¹⁶ Pollard, T. D., Borisy, G. G. (2003) Cellular motility driven by assembly and disassembly from front to back. *Science*, 112, 453-65.
- ¹⁷ Sharma, S., et al. (2012) Correlative nanomechanical profiling with super-resolution F-actin imaging reveals novel insights into mechanisms of cisplatin resistance in ovarian cancer cells. *Nanomedicine*, 8, 757-66.
- ¹⁸ Guck, J. et al. (2005) Optical deformability as an inherent cell marker for testing malignant transformation and metastatic competence. *Bio-Phys Journal*, 88, 3689-98

Appendix

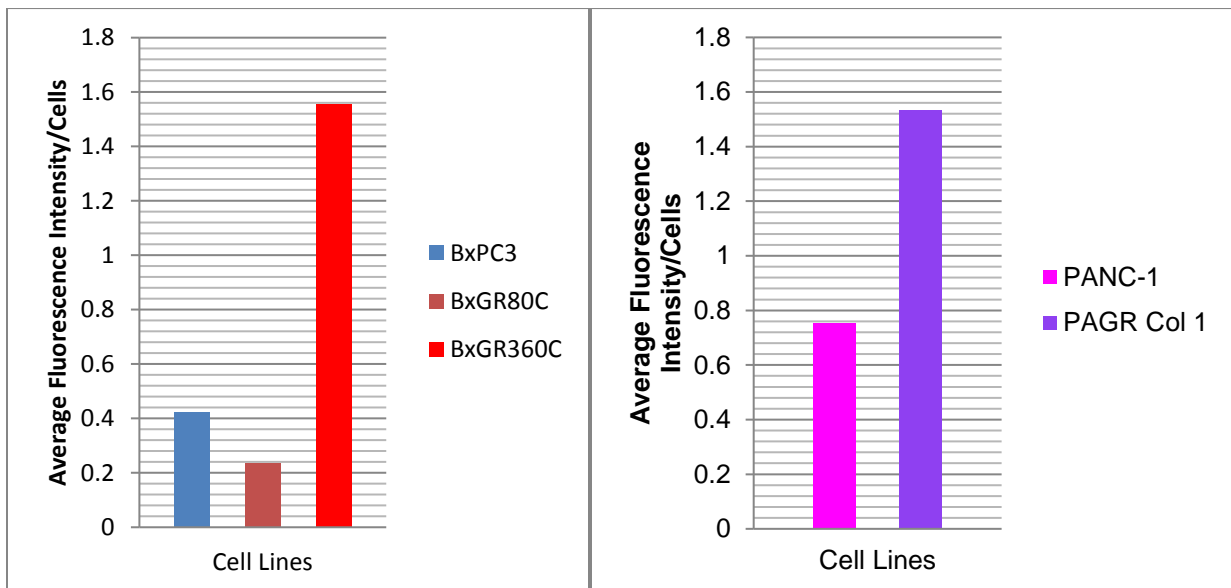
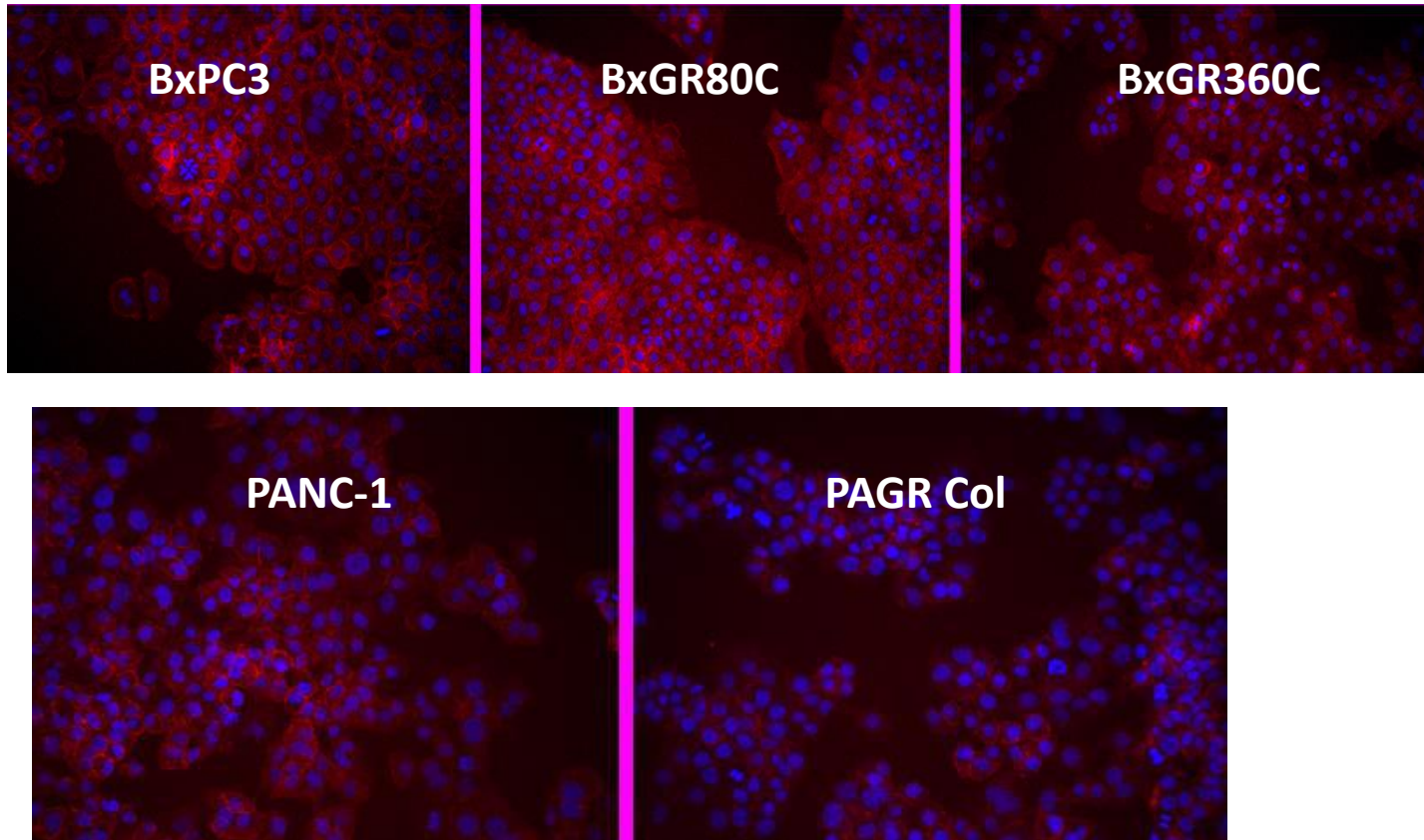
Center of Colonies:





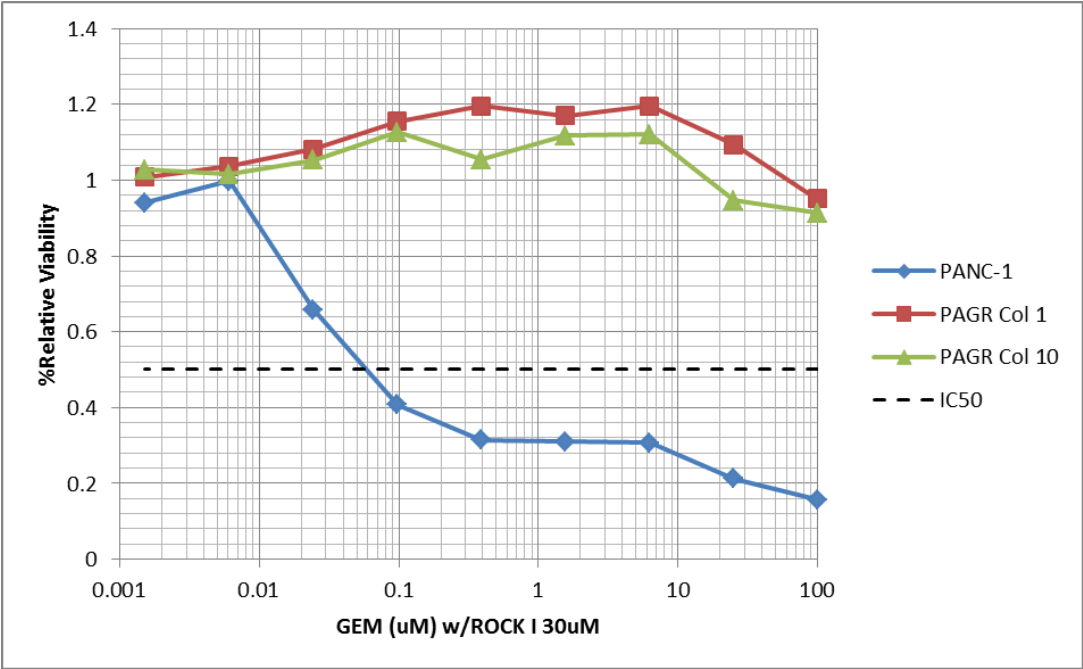
Cell Lines	tcal	tcrit (p=0.05)	Significantly Difference
BxPC3-BxGR360C	0.102420998	2.228	NO
BxPC3-BxGR80C	23.03137308	2.228	YES
BxGR80C-BxGR360C	9.572862541	2.228	YES
PANC1-PAGR Col1	18.42972913	2.228	YES

Edges of Colonies:



Cell Lines	tcal	tcrit (p=0.05)	Significantly Difference
BxPC3-BxGR360C	42.94987	2.228	YES
BxPC3-BxGR80C	10.59748	2.228	YES
BxGR80C-BxGR360C	62.4159	2.228	YES
PANC1-PAGR Col1	85.64683	2.228	YES

MTT Assay:



Cell Line	IC50 (nM) w/ROCK	IC50 (nM)
PANC-1	60	20
PAGR Col1	>100,000,000	>1,000,000

Design and Synthesis of a Facility for New Artificial Quantum Materials

Peter Frey¹, Haofei Wei², Kyle Shen²

¹Department of Physics, Hobart and William Smith Colleges, Geneva, NY 14456

²Department of Physics, Cornell University, Ithaca, NY 14850

I. Abstract

The material Sr_2IrO_4 , when electron doped, has physical and energetic properties that suggest it may be an unconventional superconductor of the cuprate family. If this is the case, it would be the first member of this group that is not comprised of cuprates. This could provide new information as to the mechanism behind superconductivity in the cuprate family. To definitively determine whether or not strontium iridate is a superconductor, direct resistivity tests must be made on it *in-situ*. Described here is the design of a new piece of equipment to take these measurements, as well as the results of the testing of this equipment.

II. Introduction

The search for a room temperature superconductor is an issue at the forefront of material physics because of its potential applications in areas such as power transmission lines, quantum computing, and high-power superconducting magnets. However, our lack of understanding of the phenomenon that drives superconductivity in non-BCS superconductors presents a significant obstacle in the fabrication of such a material. For this reason, most research surrounding superconductors is concerned with trying to learn more about what factors lead to a superconducting material, especially a superconducting material with a high critical temperature. One family of unconventional superconductors with a relatively high critical temperature is the cuprates, which typically consist of alternating planes of some metallic element and an octahedral oxygen structure surrounding a copper atom. The material Sr_2IrO_4 has a comparable physical structure, with strontium serving as the metallic layer and iridium replacing copper at the center of the oxygen octahedra. When surface-doped with potassium as an electron donor strontium iridate's electron structure also closely resembles that of a cuprate. Measurements taken on this material with angle-resolved photoemission spectroscopy have shown that it exhibits a d-wave gap analogous to what is observed in the cuprates, which could indicate superconductivity[1]. If this material does prove to be a superconductor it would be a significant discovery because

it would constitute the first material correctly predicted to be a superconductor similar to the cuprates. Therefore, determining whether or not strontium iridate is a superconductor could provide valuable insight as to the driving mechanism behind the cuprate family's superconductivity. To determine whether this material is in fact a superconductor, direct *in-situ* resistivity measurements must be performed on single crystal samples of the material. New equipment must be fabricated to make these measurements possible. This paper will serve to describe the design of this equipment.

III. Methods

iiia. Materials

- 4x gold pogo pins [2]
- 1x copper sample puck (fig. 1)
- Vespel frame (fig. 2)
- 4x gold filament wire
- 4x copper wire (.01 inch diameter)
- 4x small set screw
- 1x 3/8th inch screw
- 1x 6mm 4-bore ceramic tubing (.03 inch hole spacing) [3]
- Torr seal epoxy [4]
- Silver epoxy [5]
- Polyimide tape (.002 inch thickness)

iiib. Design

During measurements the sample will be mounted to a copper puck which is inserted into the slot on the top vespel piece. In order to eliminate contact resistance from the measurement, four pins should be used to contact the sample in a Van der Pauw configuration[6]. Pogo pins were used so that any extra force applied would be less likely to break the sample. The pins are held in a length of 4-bore ceramic tubing with torr seal epoxy to ensure they stay in the correct configuration, such that some length of pin extends from both ends of the ceramic. On one end of the pin (the end not contacting the sample) the pin is attached to a piece of copper wire. This is done by binding the two together with thin gold wire, then applying silver epoxy to all three materials to create a conductive bond. This method provides a robust bond that is not easily broken by mechanical force or thermal flexing. Once the epoxy has dried the connections should be wrapped in polyimide tape to prevent them from shorting to other pin-wire connections. The ceramic tube is mounted to the top of the center vespel piece with torr seal epoxy such that it is directly under the sample. The copper wire can be attached to the middle vespel piece with set screws, both to decrease the risk of some

force on the wire damaging the pin setup and to provide an opportunity to switch to a potentially more robust, higher gauge wire. The large screw is mounted to the bottom vespel piece and threaded through the center piece, such that when it is turned the center piece moves up or down on the threads. When in vacuum a transfer arm can be used to turn this screw. It is by this mechanism that the pin bundle is moved upwards to contact the sample.

IV. Results

Ex-situ measurements were performed on the sample to ensure that all contacts were capable of contacting the sample and taking data without malfunction. Figure 3 shows the voltage measured at various applied currents. The resulting linear relationship is what would be expected based on Ohm's Law, suggesting that the equipment is in fact successfully taking data for the sample.

V. Conclusions & Future Work

Strontium Iridate has the potential to be a new type of superconductor within the cuprate family. If this is the case, it could be the key to a deeper understanding about what makes these types of materials superconductors. The described equipment provides a method to test this material for superconductivity. Information gained from these tests could hopefully serve to further our theoretical understanding of unconventional superconductors, and help us more accurately predict which new materials could act as superconductors.

VI. Acknowledgements

I would like to thank Haofei Wei, Brendan Faeth, Kyle Shen, and the Shen group for their guidance and contributions to this project. This research was supported by the Cornell Center for Materials Research with funding from the NSF Research Experience for Undergraduates program (DMR-1460428 and DMR-1120296).

VII. References

- [1] Kim, Y. K., N. H. Sung, J. D. Denlinger, and B. J. Kim. "Observation of a D-wave Gap in Electron-doped Sr₂IrO₄." *Nat Phys Nature Physics* 12, no. 1 (2015): 37-41. doi:10.1038/nphys3503.

- [2] "Ultra-Mini Pogo Pin." Emulation Technology, Inc. Accessed August 09, 2016. [https://www.emulation.com/catalog/pogo/model 9.70-1](https://www.emulation.com/catalog/pogo/model%209.70-1)

[3] "Ceramic Membranes for Optimal Separation." AdValue Technology. Accessed August 09, 2016. <http://www.advaluetech.com/products/ceramic-membrane/ceramic-membranes>.

[4] "Torr Seal Low Vapor Pressure Epoxy." Kurt J. Lesker Company. Accessed August 09, 2016. https://www.lesker.com/newweb/fluids/sealants_epoxy.cfm?pgid=torrseal.

[5] "EPO-TEK H20E." Epoxy Technology. Accessed August 9, 2016. http://www.epotek.com/site/administrator/components/com_products/assets/files/Style_Uploads/H20E.pdf.

[6] Pauw, L. J. Van Der. "A Method Of Measuring Specific Resistivity And Hall Effect Of Discs Of Arbitrary Shape." *Semiconductor Devices: Pioneering Papers*, 1991, 174-82. doi:10.1142/9789814503464_0017.

II X. Figures

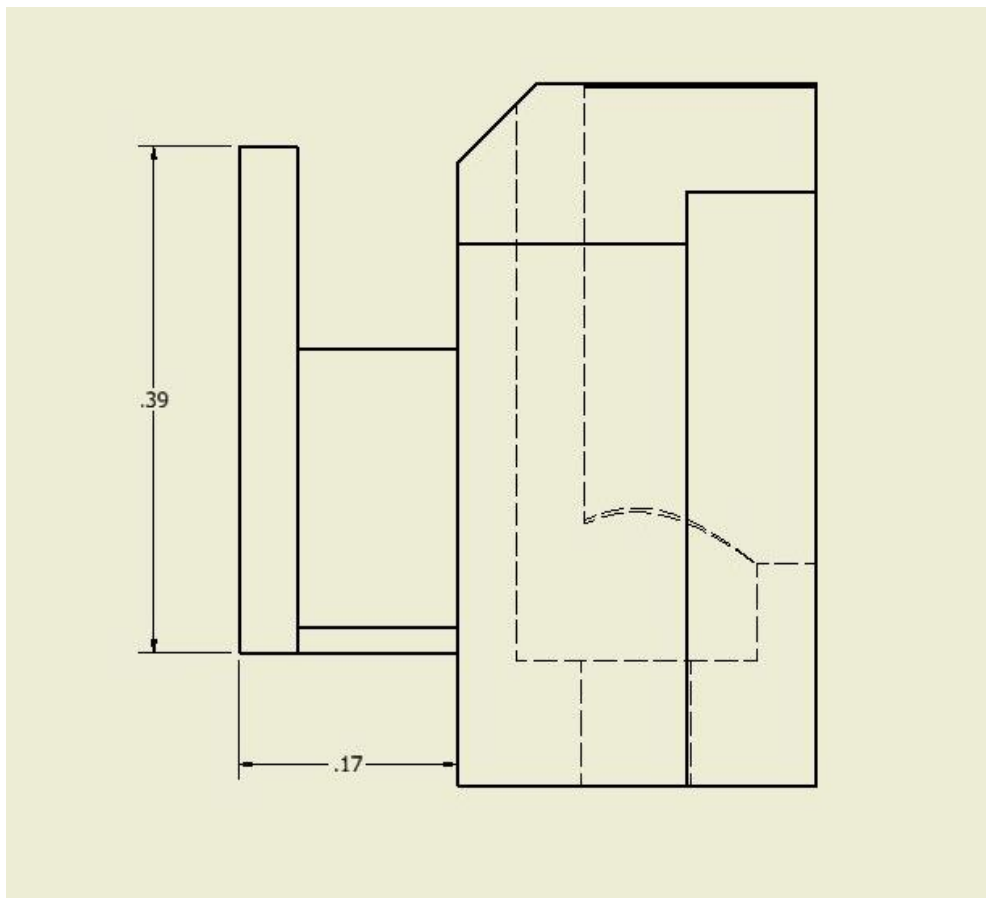


Fig. 1a) Technical drawing of copper puck used for sample mounting (side view)

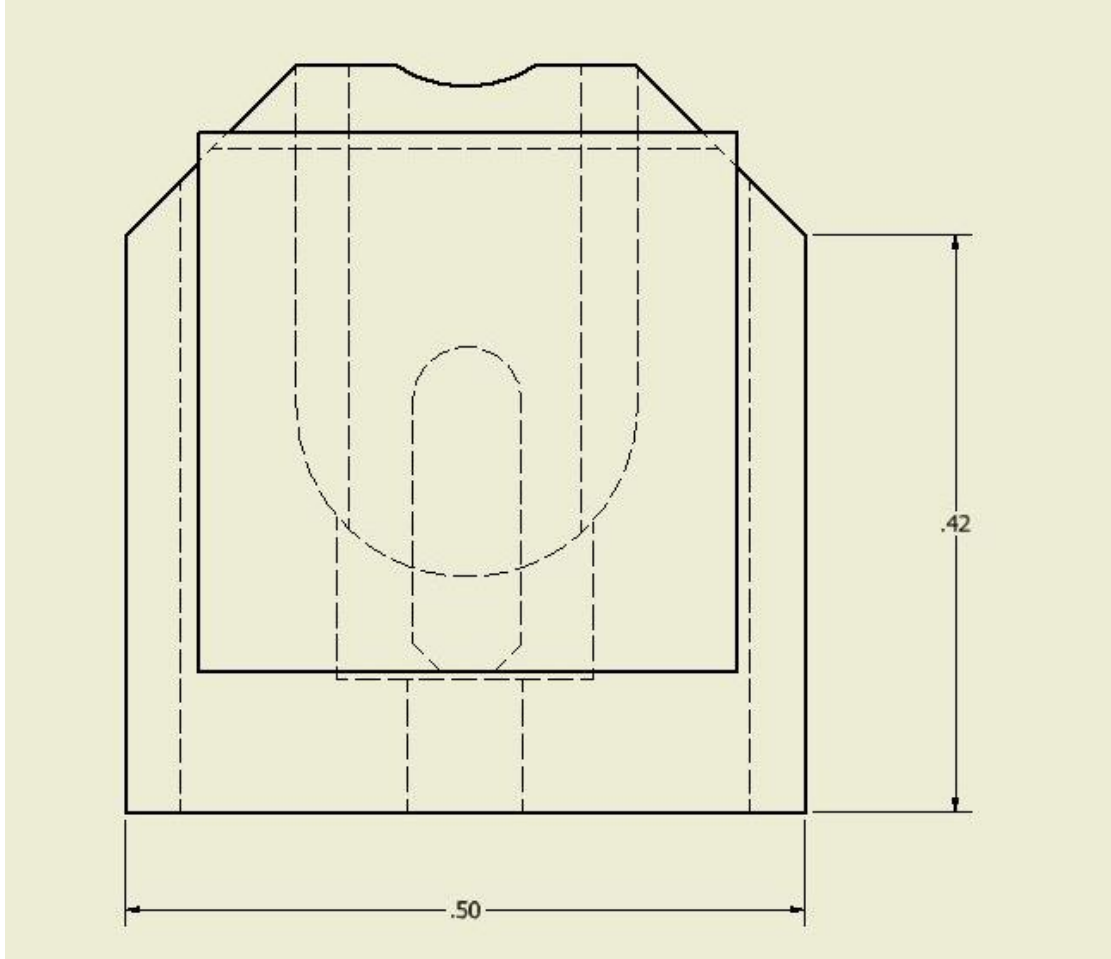


Fig. 1b) Technical drawing of copper puck used for sample mounting (top view)

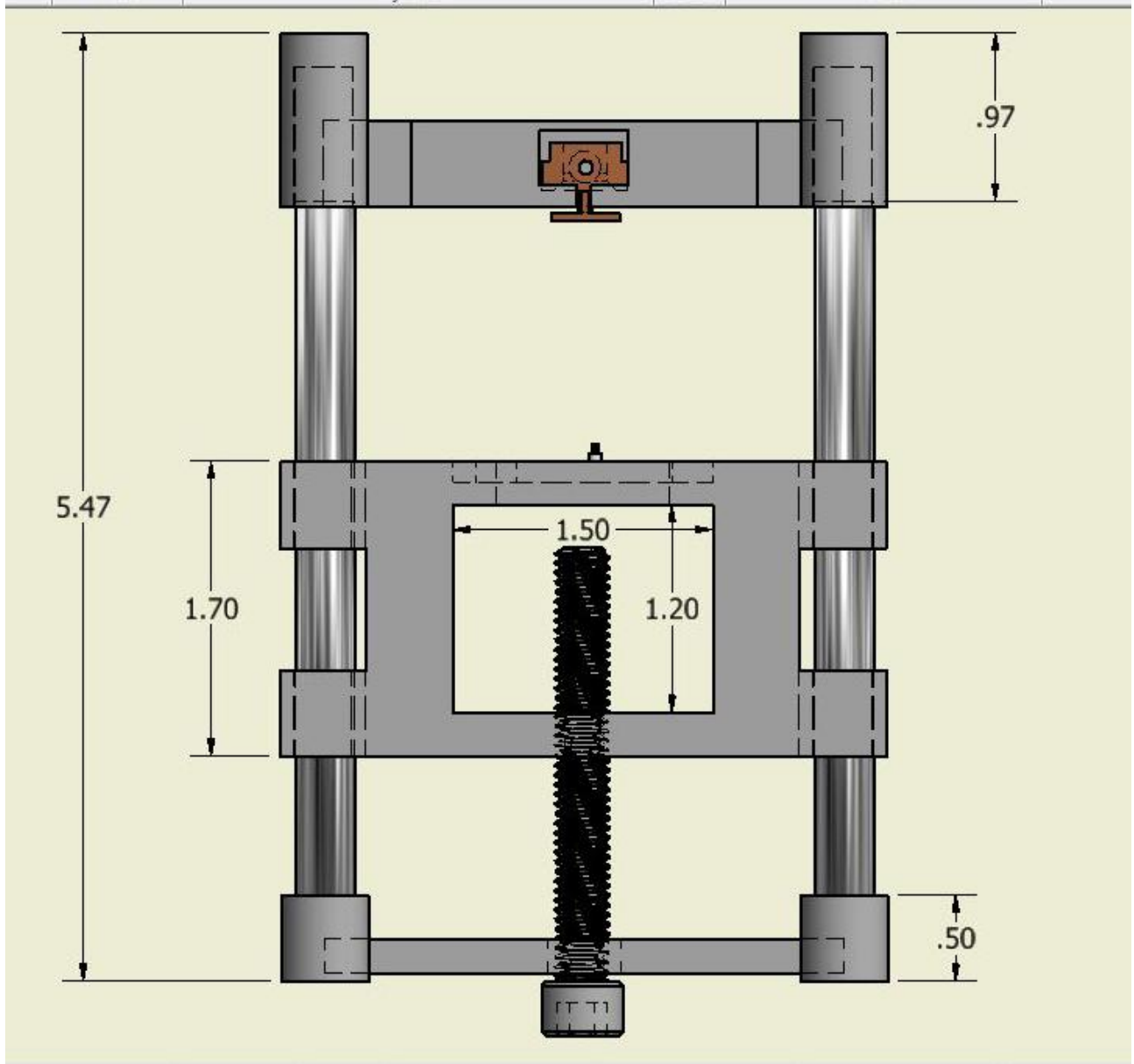


Fig. 2a) Technical drawing of vespel parts in completed apparatus, front view

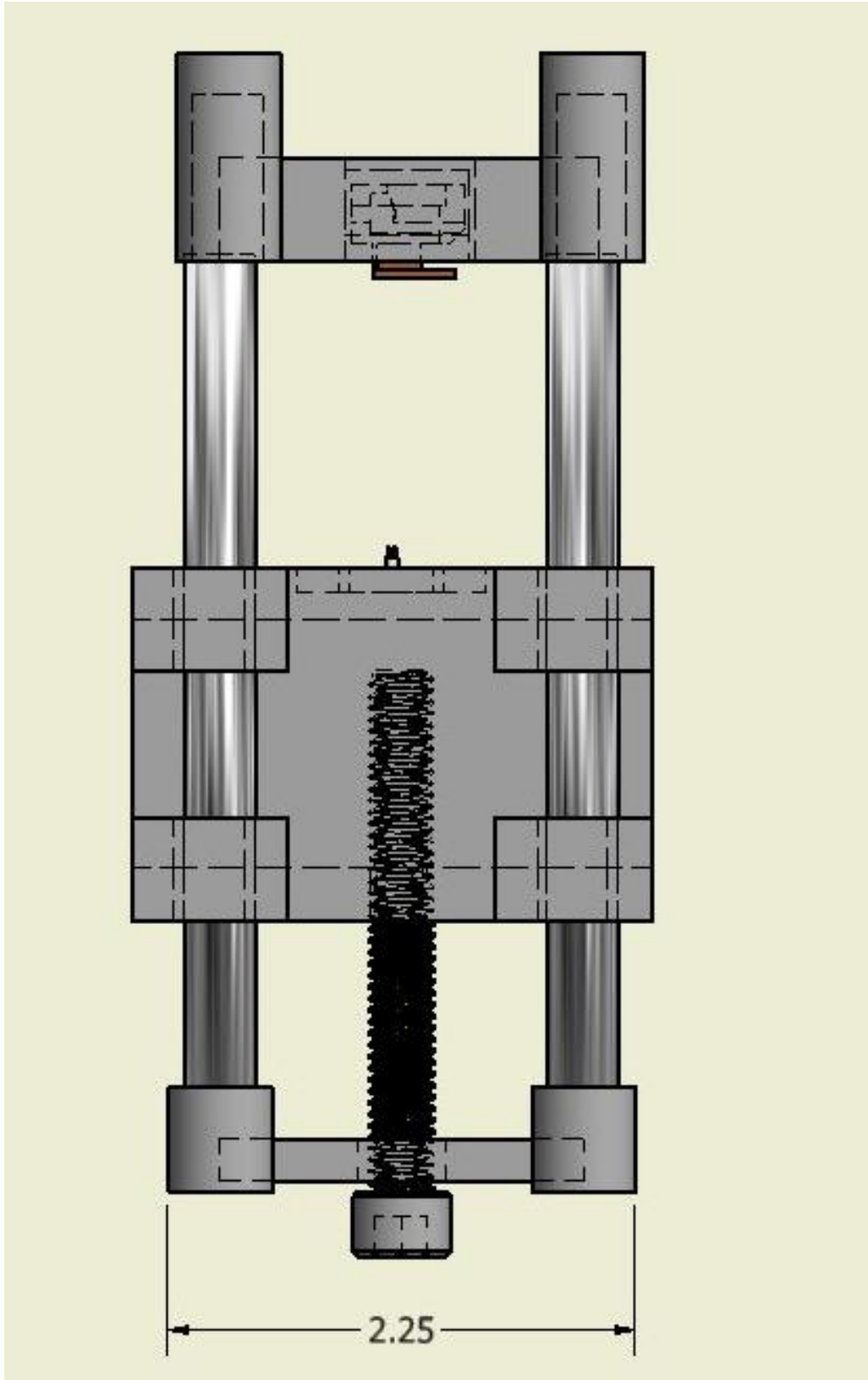


Fig. 2b) Technical drawing of vespel parts in completed apparatus (side view)

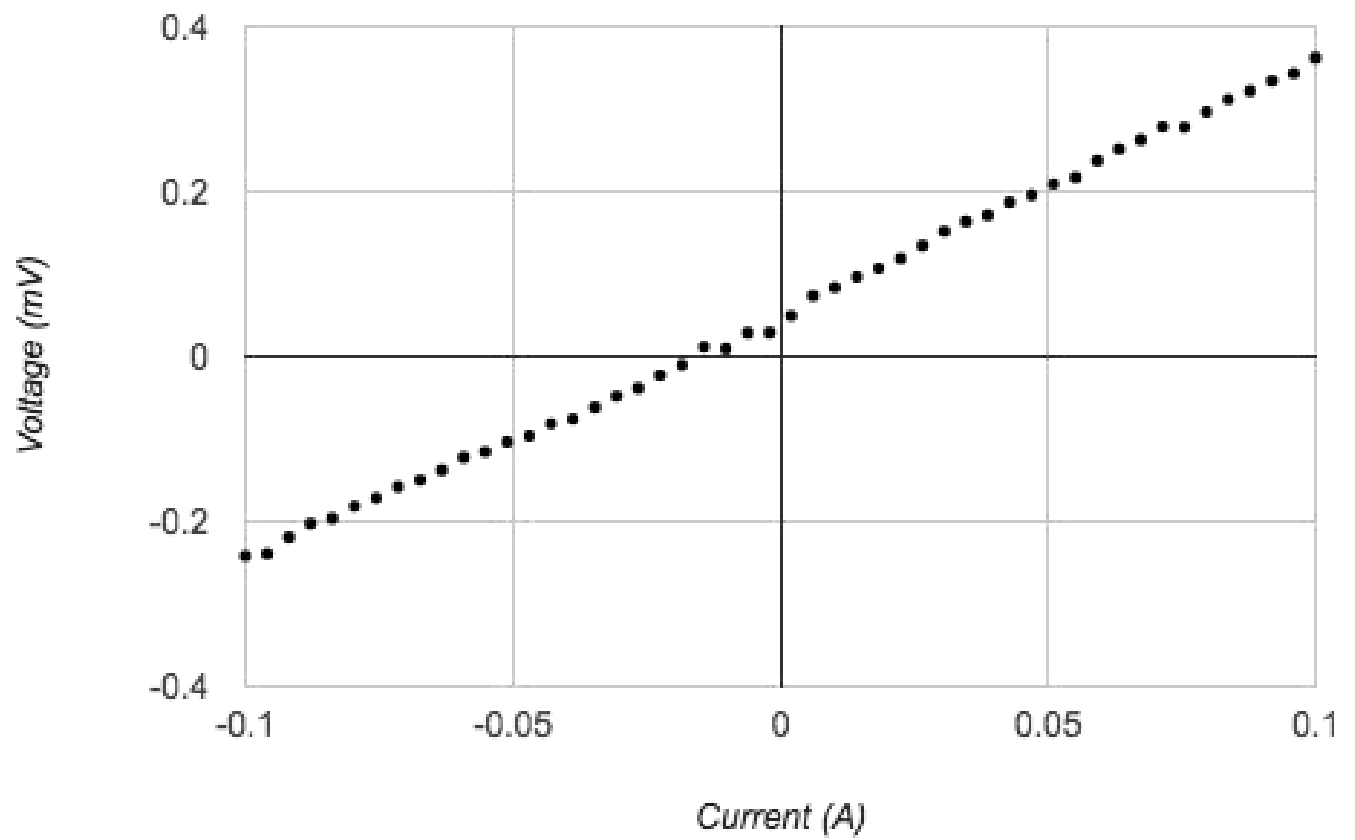


Fig. 3) Voltage vs. current data from equipment test run

Implementing Digital Feedback Control for Scanning SQUID Microscopy

Ashley Hardy, *Department of Physics, Astronomy, and Geosciences, Valdosta State University*

B. T. Schaefer and K. C. Nowack, *Laboratory of Atomic and Solid-State Physics, Cornell University*

Scanning SQUID microscopy is a magnetic imaging technique used to study magnetic properties of materials. Here, we built a breakout box to enable easy IV testing of our scanning SQUIDs using the four-point resistance measurement. Once we have selected a SQUID with good IV characteristics, we select a bias current that keeps the SQUID in the state where it is most sensitive to magnetic flux. Using a digital PID feedback controller, we monitor the voltage of the SQUID and keep it at its most sensitive point. The PID controller was tested by changing the flux using a permanent magnet and solenoid, which revealed that the PID controller can maintain the SQUID at its most sensitive point.

I. Introduction

Superconducting quantum interference devices (SQUIDs) are devices that allow us to detect magnetic fields at micron length scales in a low temperature environment. Our SQUIDs, specially designed for magnetic microscopy, can measure magnetic fields as small as 100 nT (10^{-7} Tesla). As a comparison, the Earth's magnetic field is about 45 μ T (4.5×10^{-5} Tesla). Being able to measure magnetic fields on this scale allows us to view magnetic features, including magnetic fields produced by currents, vortices in superconductors, and local magnetism on a variety of materials. This includes a variety of quantum materials such as van der Waals materials, unconventional superconductors, and topological insulators. To remain sensitive to small changes in magnetic fields, we implement a digital PID feedback controller that manipulates the flux of the SQUID to remain in its most sensitive operating regime.

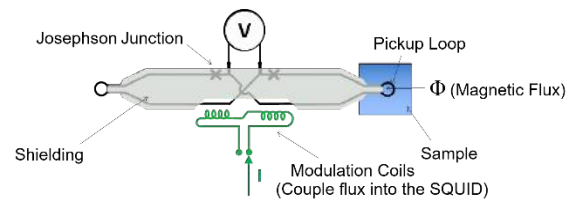


Figure 1: Diagram of a SQUID. We input current through the modulation coil and measure the change in the voltage from the terminals. The pickup loop scans above the sample [mention that signal depends on amount of flux through pickup loop].

II. Background: SQUID Design

Figure 1 shows a schematic diagram of a SQUID. We scan over the sample using the pickup loop on the left end of the SQUID. We bias the SQUID at a specific current and as the flux through the pickup loop changes, it changes the voltage of the SQUID. The pickup loop has a twist in the loop with an opposite pickup loop symmetric to it to cancel the effects of uniform background fields. The shielding layer protects the SQUID from unwanted flux coupling into it. We can pass a current to the modulation coil to change the amount of net flux through the SQUID, which in turn changes the voltage over the SQUID.

Our SQUIDs are made completely out of Nb, except for two Nb/AlO_x/Nb Josephson junctions. The junctions determine the critical current of the SQUID. At low values of current less than the critical current, the SQUID is superconducting. For values greater than the critical current, the Josephson junctions prevent the SQUID from superconducting. Instead, it behaves resistively.

III. Testing SQUIDs: IV Characteristics

We use a four-point resistance measurement to obtain the IV characteristics of SQUIDs. The advantage of using a four-point measurement technique is that it eliminates changes in the voltage due to the resistance in the wires. We use this measurement method to test for superconductivity below the critical current and how the critical current changes as we apply different amounts of magnetic flux, both of which are basic properties of SQUIDs.

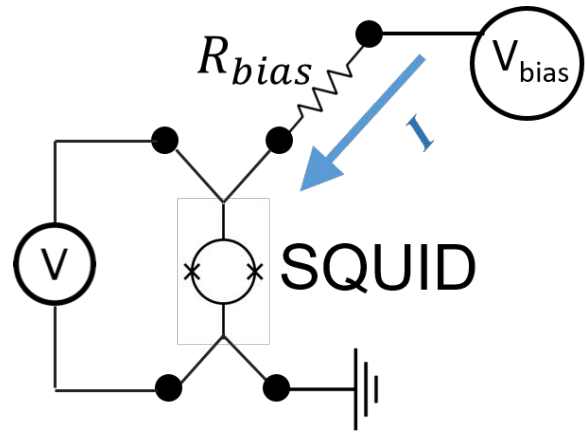


Figure 2: Four-point measurement of a SQUID. We apply a voltage to a resistor to current-bias the SQUID and measure the voltage across the SQUID.

Figure 2 illustrates our four-point measurement, where we apply a voltage V_{bias} to a resistor R_{bias} and measure the SQUID voltage, V . In doing the four-point measurement, we choose a bias resistance value that is much greater than the resistance of a SQUID so that the current passing through the circuit is nearly:

$$I_{bias} = \frac{V_{bias}}{R_{bias}}$$

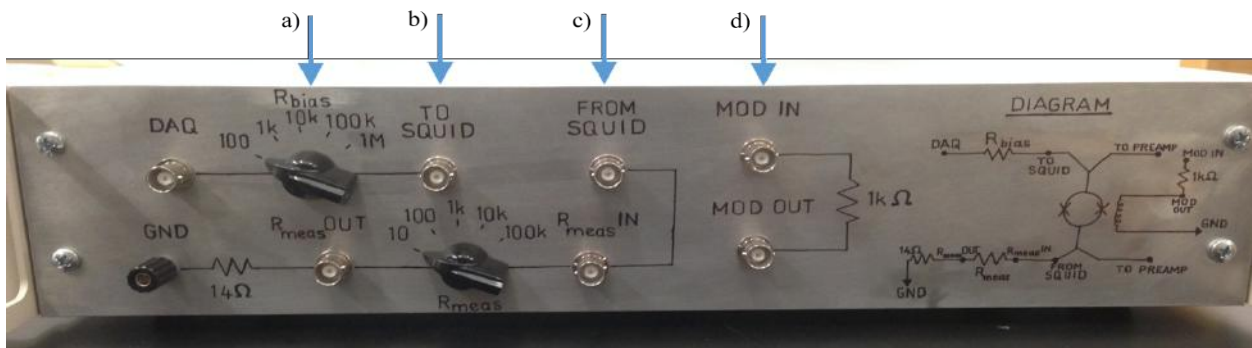


Figure 3: The breakout box that we use to characterize the SQUID: a) switch that allows selection of a bias resistor b) and c) BNC ports connect the breakout box to the SQUID; d) Terminals to send a current through a 1 kΩ resistor to the modulation coil.

Figure 3 is a breakout box we designed and built that would enable easy testing of a SQUID. The “DAQ” BNC is where we input a bias voltage. The bias resistor “ R_{bias} ” determines the approximate current flowing into the SQUID. Because this resistance switch allows us to choose from a few different resistors inside the box, it gives us a range of bias currents to test over. The “SQUID” terminals allow us to easily connect a SQUID to the breakout box. The “MOD” terminals allow us to send a current through a $1\text{k}\Omega$ resistor and into the modulation coil.

The IV characteristics of a SQUID at two different values of flux are shown in Figure 4. We can see that at low bias current, the SQUID is superconducting where the slope is zero. Once the current passing through the SQUID reaches the critical current, marked with arrows in Figure 4, the SQUID then becomes resistive. When we change the total flux through the SQUID by passing current

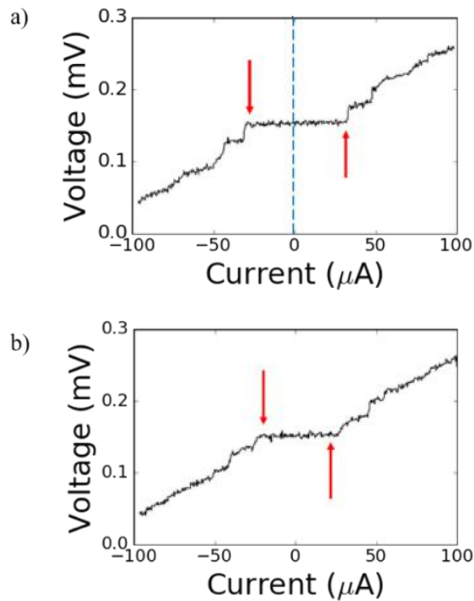


Figure 3: IV characteristics of a SQUID with modulation coil current of (a) $0\ \mu\text{A}$, (b) $200\ \mu\text{A}$. The critical currents are depicted by red arrows. The critical currents of the SQUID change with the modulation coil coupling flux into the

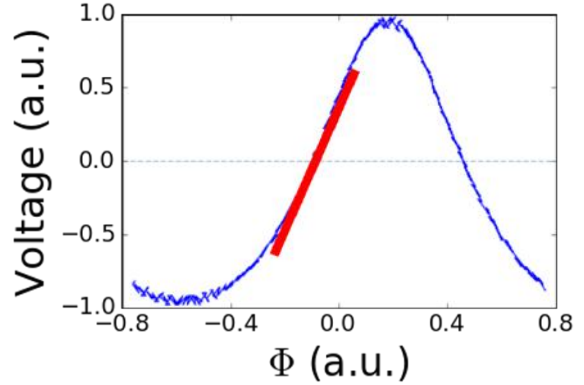


Figure 2: Response of the SQUID voltage to an applied flux at a fixed bias current. The tangent red line represents the maximum slope. The area of the graph we would like to focus our measurements is $V = 0$.

into the modulation coil, there is a change in the critical currents of the SQUID.

Figure 5 shows that the squid voltage responds sinusoidally to applied magnetic flux at a set value of current. The slope of the graph is steepest where the voltage is zero, meaning that there is a maximum change in voltage for a small change in flux. This part of the graph depicts the most sensitive part of the SQUID. We want to manipulate the flux of the SQUID to keep the voltage at zero to take advantage of the sensitivity of this region.

IV. Controlling Flux Sensitivity Using Digital Feedback

When trying to detect very small magnetic fields, it is important to keep the flux of the SQUID constant so that we get the greatest change in voltage for a small change in flux (see Figure 5). Typically, this is done using an analog feedback circuit, but these circuits typically include nonlinearities and may introduce additional noise into the measurement. We chose to implement a digital Proportional-Integral-Derivative (PID) controller to avoid using an analog

circuit. The goal of the PID controller is to keep its input at a fixed setpoint. The feedback controller calculates the difference between its input and the setpoint, giving us the error $e(t)$. Using the equation below, the controller calculates an output $u(t)$, which in turn will affect the next input into the controller. The calculation equation is:

$$u(t) = K_p e(t) + K_i \int_0^t e(\tau) d\tau + K_d \frac{de(t)}{dt}$$

where K_p , K_i , and K_d are the coefficients of the proportional, integral, and derivative terms [3]. Each term accounts for some part of the error; the proportional term takes into account the current values of the error, the integral term the past values of the error, and the derivative term the possible future values of the error. We tune the feedback controller by adjusting the coefficients of the equation.

For our system, the measured voltage of the SQUID is the input to the PID and the modulation coil current is the output. The controller measures the SQUID voltage, calculates the deviation from zero, and outputs a modulation current to keep the voltage close to zero, the most sensitive region of the SQUID.

V. Testing the Digital Feedback Controller

To test the PID controller, we place a neodymium magnet above a SQUID to introduce an external flux to the system.

After about seven seconds, we abruptly remove the magnet from the SQUID. After the same amount of time passes again, we quickly replace the magnet, but this time upside down introducing a magnetic field in the opposite direction.

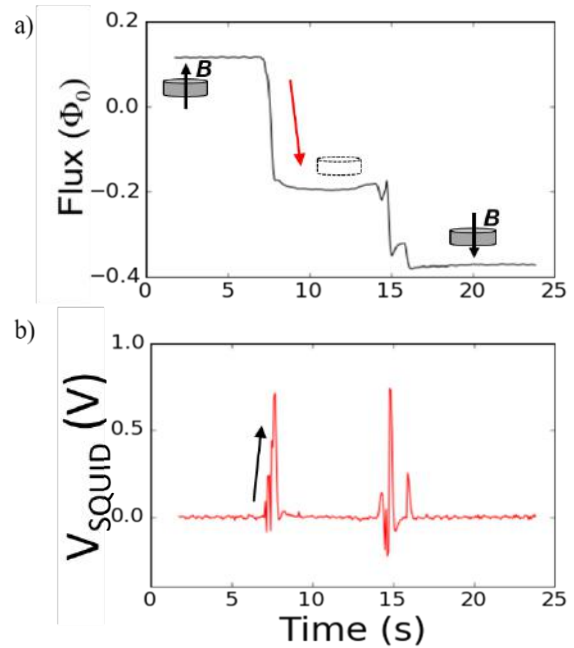


Figure 4: a) Output of the PID controller. This is the flux coupled in through the modulation coils required to exactly cancel the flux entering the pickup loop. b) SQUID Voltage. This is the input to the PID controller. When the magnet is lifted from the chamber, SQUID voltage begins to rise indicated by the black arrow. The PID controller then calculates how much flux it needs to couple in to the SQUID to bring the voltage back to zero and reduces the amount of flux, indicated by the red arrow.

Figure 6 shows the results of testing the PID controller using this method. This test shows that the feedback controller indeed keeps the voltage at zero. While the magnet is sitting above the SQUID motionless, the SQUID voltage remains at zero; therefore, the feedback controller does not change the amount of flux coupling into the SQUID. When we remove the magnet, the measured voltage quickly increases. As it increases, the PID controller corrects for this by passing a current into the modulation coil, coupling flux into the SQUID to bring the voltage back to zero. The same response occurs when we replace the magnet upside-down near the SQUID.

Though this testing method proves that the digital feedback controller is working, these dramatic changes in flux are not a typical simulation of the changes in flux we aim to measure. As a more controlled test, we lift the magnet slowly away from the SQUID using a scissor lift. While we lift the magnet, the flux of the SQUID is slowly decreasing, and the digital feedback controller properly adjusts the modulation current to keep the SQUID voltage at zero (Figure 7b). The results of this test prove that the feedback controller works with less drastic changes in flux. Though this tests the feedback controller well, we observe stair-step variations in Figure 7a that are a result from manually raising the scissor lift. by hand where the speed of the turns in uneven.

As a more controlled way of testing the SQUID, we placed a solenoid above the SQUID and passed a sinusoidal current through it, creating a slowly varying magnetic field coupling into the SQUID. Figure 8b shows that the output of the PID controller looks roughly sinusoidal; however, the PID controller does not keep

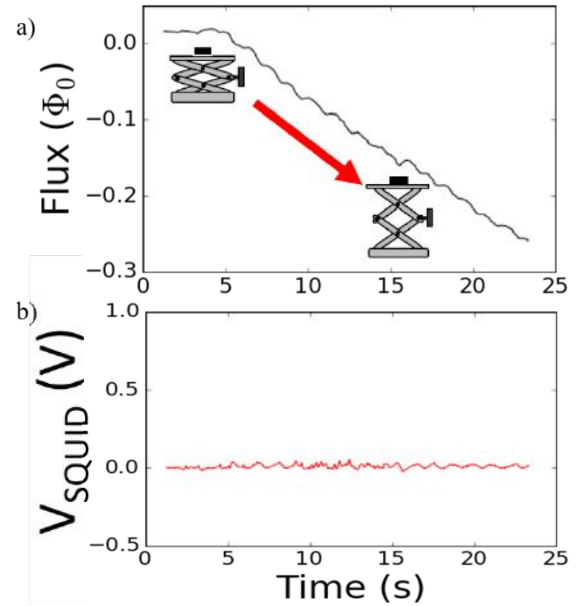


Figure 7: a) The graph of the flux response proves that the PID controller responds well to a less drastic change in flux. As the magnet is slowly being lifted, the graph of the flux is decreasing, showing that the PID is responding well to the slow change in the flux of the SQUID. b) The voltage we are measuring from the SQUID stayed around zero.

the voltage closely enough to zero. The systematic fluctuations of the voltage indicate that the feedback controller is not properly tuned to correct the modulation current quickly enough. From this test, we conclude that we need to correct the tuning of the PID feedback controller. In order to do that, we need to figure out how long it is actually taking for the feedback controller to correct the change in the flux of the SQUID. We can use a square wave to change the flux instantaneously. The results of Figure 8d show us that the feedback controller overshoots the desired value, and then corrects itself, taking a few seconds to do so. Our ideal PID controller will be able to calculate the correction value as quickly as possible. We still have work to do, but we can now use this information to correct and better tune the digital feedback controller so

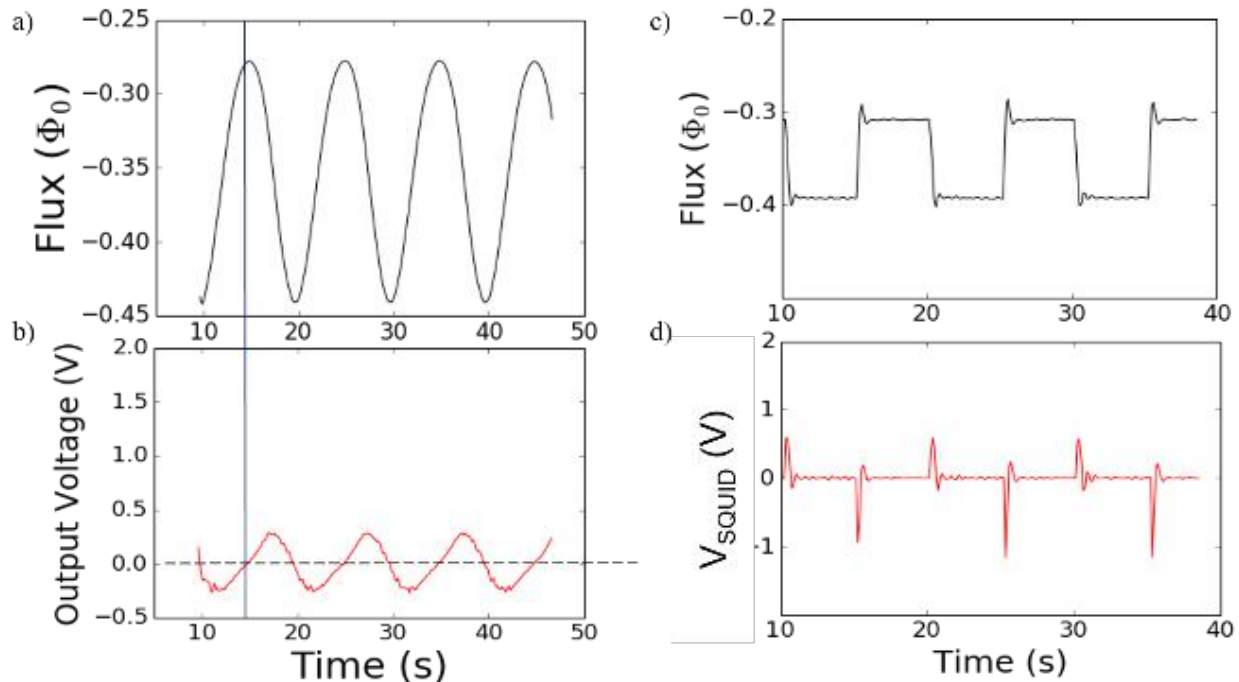


Figure 8: a) The PID feedback controller's response to the sinusoidal current input to the solenoid. b) The voltage changes due to the change in flux from the solenoid and the feedback controller's efforts to keep the values at zero. c) The response time of the PID controller is more evident in the response graph. d) The voltage response of the square wave test. The peaks in this graph align with the oscillations of the PID feedback.

that we can use it when actually scanning samples with the SQUIDs.

VI. Conclusion

Knowing we can control the voltage of the SQUID using a digital feedback control method gives us new possibilities of measuring samples with less noise in the system from the analog feedback. By using a digital feedback controller, we will be able to do everything from the computer and digitize all of our results. This will centralize the operations within the computer and we can eliminate the analog-to-digital converter hardware which, in turn, should eliminate some of the noise of the system [2]. When we eliminate the analog-to-digital converter, we also eliminate the possibility of the converter interpolating the data or creating discontinuities in the data [4]. By doing this, we can measure samples with small

variations in magnetic flux, such as topological insulators.

VII. Acknowledgements

We would like to thank the CCMR Research Experience for Undergraduates Site program (DMR-1460428) and the NSF MRSEC program (DMR-1120296) for funding the REU program, and we would like to thank Cornell University for the use of their facilities.

VIII. References

- [1] M. E. Huber. *Rev. Sci. Instrum.* **79**, 053704. (2008)
- [2] J. Clarke and A. I. Braginski, editors. *The SQUID Handbook*. Wiley-VCH. (2004)

[3] G. P. Starr. Introduction to Applied Digital Control. Univ. New Mexico (2006)

[4] B. Widrow and I. Kollár. Quantization Noise. 1st ed. Cambridge: Cambridge University Press. (2008)

Understanding the Solute and Solvent Effects on Processing of Hybrid Organic-Inorganic Perovskites using Density Functional Theory

Angela F. Harper¹, Blaire A. Sorenson² and Paulette Clancy²

Abstract—Hybrid organic-inorganic perovskite solar cells (HOIPs) are rapidly gaining popularity as affordable, flexible, alternatives to silicon and gallium arsenide based solar cells. Experiments have shown that processing conditions greatly affect the final perovskite product, but little is known about the mechanisms by which HOIP crystalline thin films form. HOIP perovskite thin film formation, through a one-step solution coating, is now a common method for depositing perovskite layers within solar cells. In this work, I present a computational analysis of Hybrid Organic Inorganic Perovskite (HOIP) coordination in solution, using Density Functional Theory (DFT) as the main computational technique employed, for a wide range of solvents and solutes capable of forming HOIP perovskites. By understanding the lowest energy orientations of these materials in solution, as well as which solvents are predicted to be effective in solvating these materials, this project serves to provide much-needed insight into the solution processing of HOIPs.

I. INTRODUCTION

Solar energy is at the forefront of renewable energy resources in the 21st century, and recent advancements in solar cell technology have made it possible for these cells to be available for commercial use. However, the problem still remains that the most efficient cells, based on silicon or gallium arsenide, are still too expensive to be used as a viable alternative to fossil fuels [1]. Thus, it is increasingly desirable to investigate low-cost, efficient photovoltaic (PV) materials. To this end, hybrid organic-inorganic perovskite based solar cells (HOIPs) have emerged as exciting potential candidates to address the problem of solar cell efficiency versus cost.

After the first implementation of HOIPs as solar cell transport materials in 2009, research into these materials has flourished [2]. The first cells only displayed a power conversion efficiency (PCE) of around 3-4%, but, since that time, the PCE of the cells produced today has

increased to 20-22% in the lab. This is the fastest growing efficiency of any solar cell material so far [3], [4]. HOIPs can be made from earth-abundant materials and possess highly desirable production properties such as low energy solution synthesis and roll-to-roll processing. [5]. However, the mechanism by which these perovskites form in solution remains poorly understood and is hindering the scale-up from laboratory to fabrication. Research has created HOIP solar cells with a commercially viable PCE, but without the ability to make them in large quantities and with reasonable stability. It is clear that what is needed is a full investigation of the fundamentals of perovskite growth.

A typical HOIP unit cell takes the form ABX_3 , where A is an organic cation (such as methylammonium (MA), formamidinium (FA), or Cs), B is the inorganic cation (generally Pb or Sn), and X is a halide anion (where X is Cl, Br, or I). In processing perovskite solar cells, a variety of experimentally used solvents have been tried, with the best choices being made with little to no fundamental justification and, further, no understanding of the solvent's effect on the synthesis procedure. Among the most cited solvent choices are dimethyl sulfoxide (DMSO), γ -butyrolactone (GBL), N-Methyl-2-pyrrolidone (NMP), Dimethylformamide (DMF), and Acetone (ACE). [6], [7].

Previous work in the Clancy group has determined an effective metric to gauge the performance of these solvents, namely the Mayer Bond Order (MBO) [8]. In my work, we screened other potential, as-yet untested, solvents that contain a sulfoxide bond. We hypothesized that this chemical motif could lead to the production of a more desirable MBO, perhaps comparable to the best performing solvents used to date. In doing so, we were able to provide a fundamental explanation for the use of an additive, tetrahydrothiophene 1-oxide (THTO), investigated by an experimental group working on HOIPs at the University of Virginia. This work was the first of its kind to better understand the processing-structure-property triad of solution processed HOIPs. However, the mechanism by which these perovskite

*Support for this work is provided through the NSF MRSEC REU program (DMR-1120296) and the REU Site program (DMR-1460428).

¹Department of Physics, Wake Forest University, 1834 Wake Forest Rd., Winston-Salem, NC 27109

²R.F. Smith School of Chemical and Biomolecular Engineering, Cornell University, Ithaca, NY 14853, USA

precursors form in solution is still unexplained. There is no confirmed “best” combination of halide, cations and solvent; the processing “recipe” to achieve a high PCE is still very much a trial-and-error process. A comprehensive exploration of the large number of combinations of solvent, halide, and cations will only be possible using computational methods.

In this work, I will investigate the nucleation and early-stage growth of perovskite thin films in precursor solutions. I will study the impact of various solvent, halide, and cation combinations, and the mechanism by which these precursors form in solution. Here, I present a computational method using density functional theory (DFT) to investigate the complexation of the building blocks that comprise a HOIP unit cell. This will be modeled after the experimental one-step perovskite formation method in which a lead salt and organic halide are combined in solution, spin-coated onto a substrate, and then thermally annealed to form a HOIP thin film [9]. I propose a potential mechanism by which these sub-units come together, by understanding the paths of minimum energy in solution.

II. METHODS

A. Classifying the Sub-units of the HOIP Unit Cell

In order to formulate a perovskite-like structure in solution, the chemical components are typically a lead salt (PbX_2) and an organic halide, which, in this work, will be MAX, where MA is a positively charged methylammonium ion and X is either Cl-, Br-, or I-. These two components come together in solution to form a neutral “monomer,” PbX_3MA , shown in Fig. 1A. Two monomers in solution that have complexed together we will then refer to as a “dimer,” as shown in Fig. 1B.

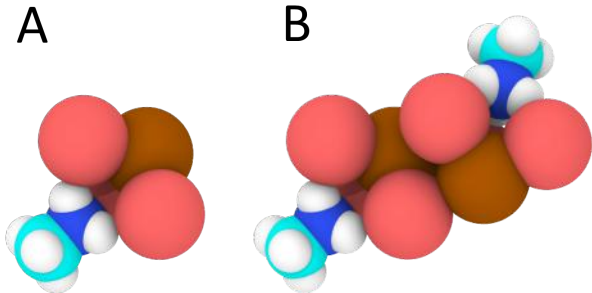


Fig. 1. A) Monomer containing lead (brown), three Br halide ions (magenta) and a methylammonium organic cation, containing C (cyan), N (blue) and H (white). B) Dimer consisting of two monomers.

By breaking the final HOIP crystal down into smaller sub-units, we are able to use accurate DFT methods

which are accessible only to small numbers of atoms. Using an open-source electronic structure code, Orca [10], we can obtain electronic properties of the dimers, and use this information to better understand their chemical properties. In this work, we will mainly discuss the nature of the possible dimers in solution.

B. Determining Lowest Energy Conformations of HOIP Perovskite Dimers

HOIP monomers could dimerize in many different orientations. In order to determine which of these has the lowest energy state, we employed a nudged elastic band (NEB) method [11], [12]. Traditionally, NEB is employed to find the path of minimum energy between two points using iterative optimization steps. For HOIP dimers, these points are different angles that define the relative orientation between the two monomers. To generate an approximate path, I first optimized the dimers with the methylammonium (MA) cations positioned at 0° , 90° and 180° orientations, as shown in Fig. 2. A linear interpolation found the path of rotation between these three states. To obtain the most energetically favorable path, I employed a BFGS optimization algorithm, combined with a B97-D3 functional, and def2-SVP basis set for the DFT energy calculations [13], [14]. This lower level of theory serves as a starting point for more accurate subsequent double-hybrid calculations in explicit solvent. This allows the more expensive calculations to start at an already partially optimized state, thus lowering the computational expense.

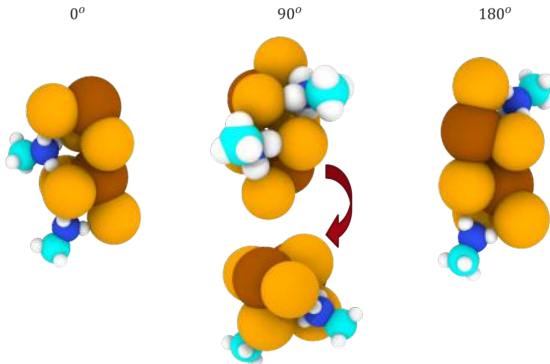


Fig. 2. Three optimized dimer configurations, denoted by the approximate angles of rotation between the methylammonium cations connected to the lead cations. The arrow on the 90° orientation gives perspective of the angle between the methylammonium ions. Color scheme as in Fig. 1, but now including Cl (orange).

For each of the three halides, the optimal configuration was determined with NEB in both vacuum and implicit solvent for all six solvents mentioned above.

The implicit solvent was introduced using the continuum solvation (COSMO) keyword in Orca, and specifying the dielectric constant of the solvent being simulated [10]. This method eliminates the cost of including explicit solvent molecules, but estimates the properties of placing the material in a polarizable medium that represents a given solvent.

C. Sampling Solvents Using DFT Analysis

The five most commonly used solvents for HOIP formation are DMSO, GBL, NMP, DMF, and ACE (defined above). Of these, DMSO has been recognized as the solvent that most readily forms HOIP crystals in solution. Unlike the other solvents, DMSO contains a sulfoxide bond, which bonds to a lead ion in solution. Previous work in the Clancy lab showed that, by measuring the Mayer Bond Unsaturation (MBU) of this bond, which coordinates with the lead ion, we can predict how well the solvent will solvate the lead salt [15]. The Mayer Bond Order (MBO) can be calculated directly from DFT, and the MBU can be calculated using (1). The formal bond order is 2.0 for oxygen, for example.

$$\text{MBU} = \text{Formal Bond Order} - \text{MBO} \quad (1)$$

A higher MBU indicates that the atoms are more readily available to form further dative bonds, which, in turn, suggests that the molecule will be a better solvent for the lead salt.

D. Computational Techniques Employed

All of the DFT calculations in this work were performed using the quantum chemistry package, Orca, for both geometry optimizations and energy measurements [10]. The initial geometry optimizations for all of the molecules containing a lead salt were made using a B97-D3 functional and def2-SVP basis set [14], [16]. To obtain the Mayer Bond Order (MBO) and optimized energy states of solvent molecules, we used three levels of theory in order to speed up the optimization process: the molecules were initialized with B97-D3/def2-SVP, then the output of those optimizations was run on a B97-D3/def2-TZVP and, finally, a single point calculation was made using a double hybrid DFT functional PWPB95 with a quadruple zeta basis set def2-QZVPP(-g,-f) [14]. For the double hybrid DFT simulation, I applied the Coulomb-fitting approximation for Coulomb integrals and the RIJCOSX approximation for the Hartree-Fock exchange integrals, from Weigend [16]. Continuum solvation was introduced using the COSMO keyword which adds a solvent using Solvation Model Density theory (SMD) [17].

The nudged elastic band calculations used the Broyden-Fletcher-Goldfarb-Shanno (BFGS) algorithm to determine the minimum energy path between two states [13]. These optimizations were performed at the B97-D3/def2-SVP level of theory. The nudged elastic band algorithm was adapted by Henry Herbol in the Clancy group [11], [12]. All of these calculations were done on servers operated by the Institute for Computational Science and Engineering (ICSE).

III. RESULTS

A. Dimer Orientation Dependence on Solvent

In order to simulate the effects of placing a dimer in solution, one method would be to place solvent molecules around the dimer, simulating a realistic situation in which the solvent molecules are interacting with each other and the dimer. However, there is an infinite configurational space by which these solvents could potentially form complexes and, thus, we must use an approximation to represent the effects of the solvent on these molecules. For this, we used the SMD continuum solvation model, employed by Orca, which places our solute in an “ether” with a chosen dielectric constant [10]. This way, we model the effects of the solvent without the computational expense and human bias of placing these molecules in an explicit solvent.

For each combination of solvent and solute shown in Table 1, NEB was used to obtain an energy profile and to identify the angle of rotation between monomers that is associated with the lowest energy, following optimization. The angle of rotation was calculated by finding a pseudo-dihedral angle between the lead and carbon atoms in the dimer. It is clear from Table 1 that, although the final energy of each conformation is within 1 kcal/mol for a given halide-solvent combination, the corresponding angle of rotation varies from solvent to solvent, for the same halide. With no solvent added, the dimers tend to have the lowest energy when the two monomers are displaced by around $10 - 20^\circ$ relative to each other; but this is not the case when they are placed in implicit solvent. Thus, it is necessary to take into account the effects of placing them in solution.

The COSMO continuum model approximates each pseudo-solvent as a point charge around our solute. Each solvent has a different dielectric constant, which -in turn- influences the overall polarization on the lead dimer. Going forward, a better representation of solvent effects would be achieved if these lowest energy configurations were used as the starting points for placing the dimers in an explicit solvent.

This computational experiment served to approximate the behavior of these solutes in solution without the

Halide	Solvent	Energy (kcal/mol)	Angle of Rotation ($^{\circ}$)
Cl	ACE	(-1992,-1991)	35
	DMF		178
	DMSO		97
	GBL		178
	NMP		91
	THTO		94
	None		18
Br	ACE	(-9557,-1996)	7
	DMF		169
	DMSO		14
	GBL		177
	NMP		6
	THTO		7
	None		12
I	ACE	(-1412,-1411)	151
	DMF		13
	DMSO		13
	GBL		14
	NMP		25
	THTO		170
	None		16

TABLE I

Final energy, and angle of rotation of the dimer conformation with the lowest energy for combinations of halide and solvent with a methylammonium cation.

computational expense of considering an explicit solvent. In future simulations, we plan to hold the dimer conformation fixed while an explicit solvent is allowed to interact with it in a Molecular Dynamics (MD) simulation. The output from this MD simulation will then be re-relaxed using a double hybrid DFT calculation. It is possible that all of the dimers will relax to the same configuration regardless of solvent, but this result would be in contrast to the results we have given above for an implicit solvent.

B. Prediction of Efficacy and Screening of Experimentally Untested Solvents

In addition to simulating the effects of commonly used solvents, we have explored the effectiveness of solvents not (yet) used in HOIP thin film formation. Previous computational work indicates that the Mayer Bond Order (MBO) is a good indicator of the relative enthalpy of solvation of the lead salt [8]. A lower enthalpy of solvation indicates that a solvent more easily forms coordination bonds with the lead. However, this

enthalpy calculation is expensive, and requires multiple simulations at different levels of theory in DFT. Thus, here, we screen the efficacy of candidate solvents quickly using the MBO. In order to compare solvents with different chemical compositions, the MBO can then be normalized using the formal bond orders of the bonded elements using Eq. 1, to find the Mayer Bond Unsaturation (MBU). For example, in a sulfoxide bond, the oxygen in the sulfoxide bond will more readily bind to the lead salt and, given that the sulfoxide functional group has a formal bond order of 2, we will subtract all of the MBOs for sulfoxides from 2. Thus, a higher MBU indicates a solvent that is more likely able to solvate the lead salt.

The first group of solvents that we chose to investigate were based on experimental results that showed that DMSO was the best solvent for lead HOIPs and our results that DMSO had the lowest MBU of any commonly used HOIP solvent. The one feature that separates DMSO from the other solvents mentioned above, is its sulfoxide bond. Sulfur is a hypervalent element, which is able to form additional bonds, and we hypothesized that other sulfoxide-based solvents would potentially provide the same stabilization as DMSO. Further evidence came from experiments using THTO, which also contains a sulfoxide bond, that showed that this additive works well in solution-processing of HOIPs.

A search for common solvents containing sulfoxide bonds led to the eight solvents shown in Fig. 3 [18]. By determining the MBU for each of the sulfoxides, I observed that the bond unsaturations followed a similar general trend based on the chemical nature of the sulfoxide group on the molecule, as discussed below. The molecules are shown in Fig. 3, and their respective MBU is given in Table 2. For reference, I have also included the MBU of both DMSO and THTO, two solvents that are known to work well for HOIP formation.

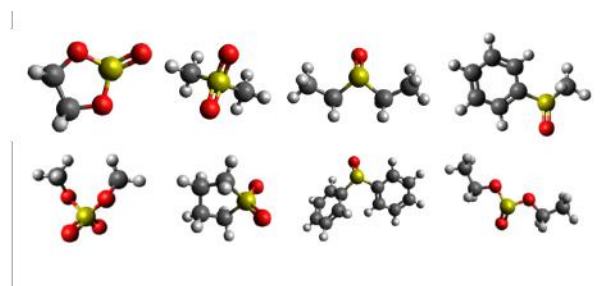


Fig. 3. Sulfoxide solvents used in the analysis. From upper left to bottom right they are ethylene sulfite, methylsulfonylmethane, diethyl sulfoxide, methyl phenyl sulfoxide, dimethyl sulfate, tetramethylene sulfane, diphenyl sulfoxide, diethyl sulfite. Color scheme as in Fig. 1.

Solvent	B97-D3	PWPB95
diethyl sulfoxide	0.41	0.53
THTO	0.39	0.52
DMSO	0.39	0.48
methyl phenyl sulfoxide	0.37	0.48
diphenyl sulfoxide	0.33	0.44
diethyl sulfite	0.03	0.29
tetramethylene sulfane	0.17	0.28
methylsulfonylmethane	0.18	0.25
ethylene sulfite	0.15	0.24
dimethyl sulfate	0.07	0.17

TABLE II

Mayer Bond Unsaturation (MBU) at the B97-D3 level of theory with a def2-TZVP basis set, and at the PWPB97 level with a def2-QZVPP(-g,-f) basis set. All MBU values are calculated using a formal bond order of 2 for the S=O bond.

For any solvent in which sulfur is bonded to 2 or more oxygens, the MBU is lower than that for a molecule which only has one sulfoxide bond. This is reasonable since it is unlikely that sulfur with a full valence shell or bonded to highly electronegative atoms will be capable of forming more bonds. The usefulness of sulfur's hypervalency appears to be degraded by the presence of extra oxygen bonds on the sulfur. Diethyl sulfoxide has the highest MBU of this group, 0.53, which is higher than either THTO or DMSO. This suggests that diethyl sulfoxide may be more effective than either of these known high performers, but it has yet to be tested for HOIP systems, probably due to the fact that it is not readily available.

One of the major problems with solvents such as DMSO that work particularly well at solvating lead salts, is that they are relatively toxic. If perovskite solar cells are to become widely used commercially, there is a clear incentive to use environmentally benign solvents. Thus, I have investigated the effectiveness of several non-hazardous solvents shown in Fig. 4 [19]. These solvents were all tested in the same fashion as the sulfoxides, and I have presented the resulting MBU for each of them in Table 3. In this case, the MBU is calculated from the most electronegative bond on each molecule such as the benzene ring, alcohol group, or any oxygen or nitrogen atom in the molecule. The corresponding formal bond orders are 2.0 for a double bond, 1.0 for a single bond, and 1.5 for resonance bonds in benzene.

From the results in Table II and III, the sulfoxide with the highest bond unsaturation is diethyl sulfoxide, with a MBU of 0.53, and the best non-hazardous solvent

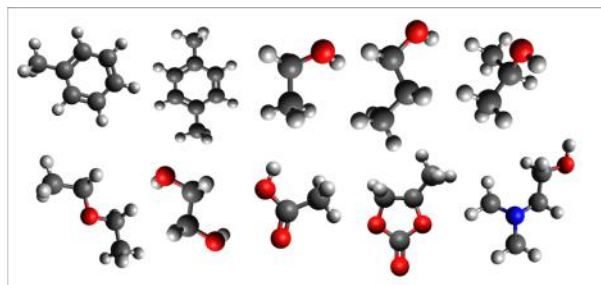


Fig. 4. Structures for the non-hazardous solvents used in the DFT calculations. From top left to bottom right: toluene, xylene, ethanol, propanol, isopropyl alcohol, diethyl ether, ethylene glycol, acetic acid, propylene carbonate, and dimethylethanolamine.

Solvent	B97-D3	PWPB95
xylene	0.09	0.11
toluene	0.15	0.10
ethanol	0.0	0.07
ethylene glycol	0.0	0.07
diethyl ether	0.0	0.07
propanol	-0.01	0.06
IPA	-0.01	0.05
DMEA : O bond	-0.07	0.04
DMEA : N bond	0.02	0.03
acetic acid	-0.10	0.01
propylene carbonate	-0.11	-0.03

TABLE III

Bond unsaturations for non-hazardous solvents using the B97-D3 functional with def2-TZVP basis set, and PWPB95 functional with def2-QZVPP(-g,-f) basis set. All bond orders are taken from the most electronegative portion of the atom (N, O, or benzene ring, depending on the atom studied).

is xylene with a weak bond unsaturation of 0.11. It is clear that solvents that do not contain a sulfoxide bond have significantly lower bond unsaturations suggesting that they are less likely to be a solvent of choice for HOIP synthesis. In fact, most of these solvents are commonly used in mixture "cocktails" to improve their effectiveness, rather than using DMSO which can be a harmful solvent.[19]. It would be informative to calculate the MBU of solvent mixtures in the presence of a lead ion. This could provide a better understanding of how these solvents help or hinder the solvation process. In this way, we may be able to identify which binary or ternary solvent mixtures lower the enthalpy of solvation.

For both classes of solvents, the level of theory and basis set used has an effect on the resulting MBU calculated. In all but one case (toluene), we see an upward

trend in the MBU from the B97-D3 level of theory to the PWPB95 level. This gives a good indication that these MBU can be compared directly, within the same level of theory.

IV. CONCLUSIONS

After studying the effects of several implicit solvents commonly used in HOIP thin film formation, we determined that the choice of solvent has a great effect on the lowest energy conformation of precursor dimers and hence how these dimers form in solution. The next step will involve further studies of these dimers in an explicit solvent to better understand their formation in solution beyond just a determination of the angle of rotation leading to the lowest energy conformation.

By computing the Mayer Bond Unsaturation (MBU) for several solvents, sulfoxides and non-hazardous solvents, we determined that diethyl sulfoxide may be a potential candidate for further investigation. Although none of the non-hazardous solvents had an MBU value close to that of DMSO and THTO, it is possible that mixtures of these solvents could be more effective in solvating a lead salt.

This work serves as a study into the complexation of HOIP precursor monomers in solution, and is one of the first computational efforts to better understand how these constituents lead ultimately to the formation of a crystalline structure. Using the lowest energy dimer conformations, and predicted effective solvents, we are able to identify how these materials might form in solution, and which solvents provide the most effective lead salt solvation.

ACKNOWLEDGMENTS

Special thanks to Principal Investigator Professor Paulette Clancy, M.S. student Blaire Sorenson, and all of the members of the Clancy Group in the Chemical Engineering department at Cornell University. This work was supported by the Cornell Center for Materials Research with funding from the NSF MRSEC program (DMR-1120296) and the Research Experience for Undergraduates program (DMR-1460428).

REFERENCES

- [1] A low-cost, high-efficiency solar cell based on dye sensitized colloidal TiO_2 films. *Nature*, 353(6346):737740, 1991.
- [2] Akihiro Kojima, Kenjiro Teshima, Yasuo Shirai, and Tsutomu Miyasaka. Organometal halide perovskites as visible-light sensitizers for photovoltaic cells. *Journal of the American Chemical Society*, 131(17):6050–6051, 2009. PMID: 19366264.
- [3] Nam-Gyu Park. Perovskite solar cells: an emerging photovoltaic technology. *Materials Today*, 18(2):65 – 72, 2015.
- [4] www.nrel.gov/ncpv/images/efficiency_chart.jpg. NREL Efficiency Chart. Accessed 2 August 2016.

- [5] Kyeongil Hwang, Yen-Sook Jung, Youn-Jung Heo, Fiona H. Scholes, Scott E. Watkins, Jegadesan Subbiah, David J. Jones, Dong-Yu Kim, and Doojin Vak. Toward large scale roll-to-roll production of fully printed perovskite solar cells. *Advanced Materials*, 27(7):1241–1247, 2015.
- [6] Giles E. Eperon, Victor M. Burlakov, Pablo Docampo, Alain Goriely, and Henry J. Snaith. Morphological control for high performance, solution-processed planar heterojunction perovskite solar cells. *Advanced Functional Materials*, 24(1):151–157, 2014.
- [7] Keyou Yan, Mingzhu Long, Tiankai Zhang, Zhanhua Wei, Haining Chen, Shihe Yang, and Jianbin Xu. Hybrid halide perovskite solar cell precursors: Colloidal chemistry and coordination engineering behind device processing for high efficiency. *Journal of the American Chemical Society*, 137(13):4460–4468, 2015.
- [8] J. Stevenson, B. Sorenson, V. Subramaniam, J. Raiford, P. Khy-labich, Y.-L. Loo, and P. Clancy. Mayer bond order as a metric of complexation in lead halide perovskite precursor solutions. Submitted August (2016).
- [9] Jin Cui, Huailiang Yuan, Junpeng Li, Xiaobao Xu, Yan Shen, Hong Lin, and Mingkui Wang. Recent progress in efficient hybrid lead halide perovskite solar cells. *Science and Technology of Advanced Materials*, 16(3):036004, 2015.
- [10] Frank Neese. The orca program system. *Wiley Interdisciplinary Reviews: Computational Molecular Science*, 2(1):73–78, 2012.
- [11] Graeme Henkelman, Blas P. Uberuaga, and Hannes Jansson. A climbing image nudged elastic band method for finding saddle points and minimum energy paths. *The Journal of Chemical Physics*, 113(22):9901–9904, 2000.
- [12] Graeme Henkelman and Hannes Jansson. Improved tangent estimate in the nudged elastic band method for finding minimum energy paths and saddle points. *The Journal of Chemical Physics*, 113(22):9978–9985, 2000.
- [13] J. Nocedal. "updating quasi-newton matrices with limited storage". *Mathematics of Computation*, 35 (151): 773782, 1980.
- [14] Lars Goerigk and Stefan Grimme. A thorough benchmark of density functional methods for general main group thermochemistry, kinetics, and noncovalent interactions. *Phys. Chem. Chem. Phys.*, 13:6670–6688, 2011.
- [15] Istvan mayer. *International Journal of Quantum Chemistry*, 109(11):2331–2339, 2009.
- [16] Florian Weigend. Accurate coulomb-fitting basis sets for h to rn. *Phys. Chem. Chem. Phys.*, 8:1057–1065, 2006.
- [17] Aleksandr V. Marenich, Christopher J. Cramer, and Donald G. Truhlar. Universal solvation model based on solute electron density and on a continuum model of the solvent defined by the bulk dielectric constant and atomic surface tensions. *The Journal of Physical Chemistry B*, 113(18):6378–6396, 2009. PMID: 19366259.
- [18] O. Wohlfahrt, C. Madelung. Static dielectric constants of pure liquids and binary liquid mixtures. pages 5–228, 1991.
- [19] Kira L. Gardner, Jeffrey G. Tait, Tamara Merckx, Weiming Qiu, Ulrich W. Paetzold, Lucinda Kootstra, Manoj Jaysankar, Robert Gehlhaar, David Cheyns, Paul Heremans, and Jef Poortmans. Nonhazardous solvent systems for processing perovskite photovoltaics. *Advanced Energy Materials*, pages n/a–n/a, 2016. 1600386.